NTNU
Norwegian University of
Science and Technology

Submerged floating tunnels exposed to internal blast loading

Nikolai Korvald Skaare

Master of Science in Mechanical Engineering
Submission date: June 2018
Supervisor: Tore Børvik, KT
Co-supervisor: Martin Kristoffersen, KT
Magnus Langseth, KT

Norwegian University of Science and Technology
Department of Structural Engineering

Department of Structural Engineering
Faculty of Engineering
NTNU- Norwegian University of Science and Technology

ACCESSIBILITY

OPEN

MASTER THESIS 2018

SUBJECT AREA:	DATE:	NO. OF PAGES:
Computational Mechanics	11. June 2018	18+131+32

TITLE:

Submerged floating tunnels exposed to internal blast loading

Neddykket rørbru utsatt for intern eksplosjonslast

BY:

Nikolai Korvald Skaare

SUMMARY:

In June 2017, the Norwegian parliament approved the plan of developing the E39 as an improved and continuous Coastal Highway Route between Kristiansand and Trondheim. The goal is to eliminate all ferry connections along the route and cut the current travel time by half. This includes long crossings over deep fjords, and unconventional methods are necessary to achieve this. One of the suggested alternatives is to use a Submerged Floating Tunnel (SFT). If the SFT were to be subjected to an internal explosion, either by accident or an intentional terrorist attack, it could have devastating consequences. Concrete is likely to be the main building material, owing to its low cost and versatility. It is therefore of interest to perform a small scale experimental study and numerical simulations to assess the potential and limitations of finite element programs in simulating concrete structures subjected to internal blast loading.

The main part of the experimental study in this thesis involved performing explosion tests on three different kind of concrete pipes; a total of 18 pipes were tested, 6 of each kind. The different pipes were the *BASAL Mufferør ig*, unreinforced, and the *BASAL Falsrør ig*, both reinforced and unreinforced. Dimensions of the pipes were 1500 mm in length, 200 mm inner diameter; and 2250 mm in length, 400 mm inner diameter, respectively. They were exposed to blast loading from centrically placed spherical C4 charges of varying size. For the smaller pipes a charge of 14 g was able to breach the pipe wall. The larger plain concrete pipes got through-thickness cracks at a charge size of 65 g and was split in two. In the case of the larger reinforced pipes, it was necessary with a charge of 300 g to create through-thickness cracks. At 500 g, the pipe wall was breached and large fragments were blown off.

For the numerical study of the pipes, the finite element analysis (FEA) software ABAQUS/Explicit was utilized. To model the concrete the implemented Concrete Damaged Plasticity (CDP) model was used. Initially, to model the pressure loading from the blast, the CONWEP model in ABAQUS was employed. A parametric sensitivity study on the larger plain concrete and reinforced pipes was performed. In general, the plain concrete pipes saw excessive erosion in the center part of the pipe, while the behavior of the reinforced pipes was well reproduced. Additionally, it was also seen that the CONWEP model was not able to take into consideration the reflections of shock waves due to confinement. This gave an underestimation of the pressure applied to the pipe, especially farther out from the center. Lastly, Eulerian analyses in Europlexus was conducted, to investigate potential improvements in describing the pressure loading. More complex effects were captured by this method, but the pressure was still underestimated.

RESPONSIBLE TEACHER: Professor Tore Børvik

SUPERVISOR(S): Professor Tore Børvik and Postdoc Martin Kristoffersen

CARRIED OUT AT: SIMLab, The Department of Structural Engineering, NTNU

Institutt for konstruksjonsteknikk
Fakultet for ingeniørvitenskap
NTNU- Norges teknisk- naturvitenskapelige universitet

TILGJENGELIGHET

ÅPEN

MASTEROPPGAVE 2018

FAGOMRÅDE: Beregningsmekanikk	DATO: 11. juni 2018	ANTALL SIDER: 18+131+32

TITTEL:

Neddykket rørbru utsatt for intern eksplosjonslast

Submerged floating tunnels exposed to internal blast loading

UTFØRT AV:

Nikolai Korvald Skaare

SAMMENDRAG:

I juni 2017 godkjente Stortinget planen om å utvikle E39 som en forbedret og kontinuerlig vei. Det langsiktige målet er å erstatte alle nåværende ferjeforbindelser med andre løsninger, noe som vil halvere reisetiden. Dette medfører lange krysninger av dype fjorder, og ukonvensjonelle metoder må tas i bruk. Et av de foreslåtte alternativene er å benytte seg av en nedsenket rørbru. Hvis denne rørbruen skulle bli utsatt for en intern eksplosjon, enten ved et uhell eller et forsettlig terrorangrep, kan det få katastrofale konsekvenser. Betong vil sannsynligvis bli brukt som byggemateriale, grunnet dens lave pris og allsidige egenskaper. Det er derfor av interesse å gjøre småskala eksperimentelle forsøk og utføre numeriske simuleringer for å undersøke potensialet og begrensningene til elementmetode-programmer i simulering av betong utsatt for intern eksplosjonslast.

Hoveddelen av forsøkene i denne oppgaven gikk ut på å utføre eksplosjonstester på tre forskjellige typer betongrør; totalt 18 rør ble testet, 6 av hver type. De forskjellige rørene var *BASAL Mufferør ig*, ikke armert, og *BASAL Falsrør ig*, armert og ikke armert. Rørdimensjonene var henholdsvis 1500 mm lange, 200 mm indre diameter; og 2250 mm lange, 400 mm indre diameter. De ble utsatt for sentralt plasserte, sfæriske C4-lladninger av varierende størrelse. For de mindre rørene var en ladning på 14 g i stand til å destruere røret. De større vanlige betongrørene var det nødvendig med en ladning på 65 g for å skape gjennomgående sprekker, hvilket delte røret i to. For de større armerte rørene trengtes det 300 g C4 for å skape gjennomgående sprekker. Ved 500 g C4 ble store fragmenter blåst av og det var store hull i rørveggen.

For den numeriske studien av rørene ble elementmetode-programmet ABAQUS/Explicit benyttet. For å modellere betongen ble den implementerte Concrete Damaged Plasticity (CDP) modellen brukt. I utgangspunktet ble CONWEP-modellen i ABAQUS brukt for å modellere trykkbelastningen fra eksplosjonen. En parameterstudie ble gjennomført på de store rørene, både armert og ikke armert. Generelt ble det observert at de vanlige betongrørene ble i overkant mye erodert på midten av røret, mens oppførselen til de armerte rørene ble godt gjengitt. I tillegg viste det seg at CONWEP-modellen ikke var i stand til å ta hensyn til refleksjoner av sjokkbølgen som følge av det lukkede eksplosjonsmiljøet. Dette ga en underestimering av trykket, spesielt lenger ut fra sentrum av røret. Til slutt ble det gjennomført Euleriske analyser av eksplosjonen i Europlexus, for å undersøke potensielle forbedringer i modelleringen av trykklasten. Mer komplekse effekter ble registrert med denne metoden, men størrelsen av trykket ble fortsatt underestimert.

FAGLÆRER: Professor Tore Børvik

VEILEDER(E): Professor Tore Børvik og Postdoktor Martin Kristoffersen

UTFØRT VED: SIMLab, Institutt for konstruksjonsteknikk, NTNU

Department of Structural Engineering
FACULTY OF ENGINEERING SCIENCE
NTNU – Norwegian University of Science and Technology

MASTER'S THESIS 2018

for

Nikolai Korvald Skaare

Submerged floating tunnels exposed to internal blast loading

1. INTRODUCTION

The Norwegian Public Roads Administration is conducting a large research project aimed at replacing the ferry connections along the E39 coastal highway route along the west coast of Norway with fixed connections. For the wide and deep fjords, a submerged floating tunnel (SFT) made of concrete has been suggested as an alternative. Reinforced concrete allows more or less any cross-sectional profile to be cast, and the buoyancy can easily be adjusted to the desired level. A potential hazard for such a structure is internal blast loading caused either by an accident or by a terrorist attack. It is important to verify that the structure is able to withstand a realistic blast load, or at least minimise the damage as a breach could have disastrous consequences. To assess the blast performance of concrete structures, plane concrete slabs and off-the-shelf precast concrete tubes have been subjected to blast loading. In addition, numerical simulations of these tests have been carried out. In this master's thesis, blast experiments using live explosives will be performed in collaboration with the Norwegian Defence Estates Agency. The data generated will be used for validation and verification of some frequently used numerical methods involving blast loading. Computational methods are now available to predict both the loading and structural response in these extreme loading situations, and experimental validation of such methods is necessary in the development of safe and cost-effective structures. In addition to simulating the experiments, full-scale simulations of an SFT is a viable goal.

2. OBJECTIVES

The main objective of the research project is to determine how concrete tubes behave under blast loading, and to validate to which extent this can be predicted using computational tools.

3. A SHORT DESCRIPTION OF THE RESEARCH PROJECT

The main topics in the research project will be as follows:

1. A comprehensive literature review should be conducted to understand the blast load phenomenon, blast load design, constitutive and failure modelling of concrete materials exposed to extreme loadings, explicit finite element methods, and possibly fluid-structure interaction.
2. Instrumented material testing of concrete cubes for validation of material models.
3. Proper constitutive relations and failure criteria are chosen and calibrated based on the material tests.
4. Experimental work on concrete tube components: Precast concrete tubes will be subjected to blast load from a C-4 charge. One charge position will be used – centrically in the cross-section.
5. Nonlinear finite element simulations of the field experiments will be performed, and the numerical results shall be compared and discussed based on the experimental findings.

Supervisors: Tore Børvik (NTNU) and Martin Kristoffersen (NTNU)

The thesis must be written according to current requirements and submitted to the Department of Structural Engineering, NTNU, no later than June 11th, 2018.

NTNU, January 15th, 2018

Tore Børvik
Professor

Acknowledgements

This thesis has been written in collaboration with the Structural Impact Laboratory (SIMLab) and Centre for Advanced Structural Analysis (CASA), connected to the Department of Structural Engineering at the Norwegian University of Science and Technology in the spring semester 2018.

Supervision and guidance has been given by Professor Tore Børvik and post-doc Martin Kristoffersen. Their support, counsel during the weekly meetings and encouragements throughout the past semester is highly regarded and a sincere thanks goes to the both of them.

Thanks to Knut Ove Hauge from the Norwegian Defence Estates Agency, for organizing the experimental tests performed at Østøya in March 2018. Additionally, a thanks goes to the Norwegian Public Roads Administration for initiating this research project. Would also like to express my gratitude to the CPU cluster *Snurre*, for providing the computational power to calculate the numerous numerical simulations performed in this thesis.

Lastly, a huge thanks goes to fellow students Olaf Kielland, Sigurd Lekve, Benjamin Elveli, Mads Iddberg, Vegard Haraldseid and Christoffer Martinsen for good discussions, thoughts, critique and ice creams in the sun.

Trondheim, June 11, 2018

Nikolai K Skaar

Nikolai Korvald Skaare

Abstract

In June 2017, the Norwegian parliament approved the plan of developing the E39 as an improved and continuous Coastal Highway Route between Kristiansand and Trondheim. The goal is to eliminate all ferry connections along the route and cut the current travel time by half. This includes long crossings over deep fjords, and unconventional methods are necessary to achieve this. One of the suggested alternatives is to use a Submerged Floating Tunnel (SFT). If the SFT were to be subjected to an internal explosion, either by accident or an intentional terrorist attack, it could have devastating consequences. Concrete is likely to be the main building material, owing to its low cost and versatility. It is therefore of interest to perform a small scale experimental study and numerical simulations to assess the potential and limitations of finite element programs in simulating concrete structures subjected to internal blast loading.

The main part of the experimental study in this thesis involved performing explosion tests on three different kind of concrete pipes; a total of 18 pipes were tested, 6 of each kind. The different pipes were the *BASAL Mufferør ig*, unreinforced, and the *BASAL Falsrør ig*, both reinforced and unreinforced. Dimensions of the pipes were 1500 mm in length, 200 mm inner diameter; and 2250 mm in length, 400 mm inner diameter, respectively. They were exposed to blast loading from centrically placed spherical C4 charges of varying size. For the smaller pipes a charge of 14 g was able to breach the pipe wall. The larger plain concrete pipes got through-thickness cracks at a charge size of 65 g and was split in two. In the case of the larger reinforced pipes, it was necessary with a charge of 300 g to create through-thickness cracks. At 500 g, the pipe wall was breached and large fragments were blown off.

For the numerical study of the pipes, the finite element analysis (FEA) software ABAQUS/Explicit was utilized. To model the concrete the implemented Concrete Damaged Plasticity (CDP) model was used. Initially, to model the pressure loading from the blast, the CONWEP model in ABAQUS was employed. A parametric sensitivity study on the larger plain concrete and reinforced pipes was performed. In general, the plain concrete pipes saw excessive erosion in the center part of the pipe, while the behavior of the reinforced pipes was well reproduced. Additionally, it was also seen that the CONWEP model was not able to take into consideration the reflections of shock waves due to confinement. This gave an underestimation of the pressure applied to the pipe, especially farther out from the center. Lastly, Eulerian analyses in Europlexus was conducted, to investigate potential improvements in describing the pressure loading. More complex effects were captured by this method, but the pressure was still underestimated.

Contents

1 Introduction **1**

2 Literature Review **5**

2.1 Previous research 5

2.2 Previous master theses 7

3 Theory **11**

3.1 Blast and explosions 11

3.1.1 Blast phenomena 11

3.1.2 Blast environments 14

3.1.3 Scaling 17

3.2 Prediction of blast loads 19

3.2.1 Empirical methods 19

3.2.2 Semi-empirical methods 20

3.2.3 Numerical methods 20

3.3 Structural response to blast loads 20

3.3.1 Impulsive loading 21

3.3.2 Quasi-static loading 21

3.3.3 Dynamic loading 21
3.4 Blast modeling 22
3.4.1 CONWEP model 22
3.4.2 Jones-Wilkins-Lee equation of state 23
3.5 Description of motion 24
3.5.1 Lagrangian description 24
3.5.2 Eulerian description 25
3.6 Explicit Finite Element Analysis 26
3.6.1 Element erosion 26
3.6.2 Eulerian mesh deformation 27
3.7 Computational Fluid Dynamics 27
3.7.1 Conservation laws 28
3.7.2 Finite Volume Method 30

4 Materials 33

4.1 Theory of plasticity 33
4.2 Concrete 35
4.2.1 The structure of concrete 35
4.2.2 Mechanical properties of Concrete 36
4.2.3 The concrete damaged plasticity model 40
4.3 Steel 42
4.3.1 Johnson Cook model 42

5 Experimental Work 45

5.1 Concrete cube compression tests 45
5.1.1 DIC 45

5.2 Pipe explosion tests 53
5.2.1 Small pipes 54
5.2.2 Large Pipes - PCC 58
5.2.3 Large Pipes - Reinforced 61
5.3 Pressure measurements 65

6 Numerical Study - Concrete Cubes 67

6.1 Workflow 68
6.2 Parameter study 69
6.2.1 Scale factor 69
6.2.2 Modulus of elasticity 72
6.2.3 Time period 74
6.2.4 Mesh size 76
6.2.5 Friction 77
6.2.6 Erosion 80
6.2.7 Material calibration 81

7 Numerical Study - Concrete Pipes 85

7.1 Small Pipes 86
7.2 Large Pipes - PCC 88
7.2.1 Effect of erosion criterion 90
7.2.2 Effect of concrete strength 90
7.2.3 Effect of mesh size 94
7.2.4 Effect of material calibration 94
7.3 Large Pipe - Reinforced 98
7.3.1 Effect of erosion criterion 100

7.3.2 Effect of concrete strength 100
7.3.3 Effect of mesh size 103
7.3.4 Effect of material calibration 103
7.4 Pressure considerations 105
7.4.1 CONWEP model 106
7.4.2 CFD simulations 111

8 Concluding Remarks 119
8.1 Summary and Discussion 119
8.2 Conclusion 123

9 Further Work 125

Appendices 133

A Concrete Data 135

B Pipe Information 139

C Material Parameters 143
C.1 CDP model: Jankowiak and Lodygowski 143
C.2 CDP model: Labibzadeh et al. 145
C.3 Johnson-Cook 148

D Experimental 149
D.1 Overview of experimental tests 149
D.2 Pressure measurements 151
D.2.1 Small pipes 151

D.2.2 Large pipes - PCC 151
D.2.3 Large pipes - Reinforced 151

E Subroutine 161

Nomenclature

Abbreviations

2D, 3D	Two-dimensional, three-dimensional
ABQ	ABAQUS
B31	Linear beam elements
C3D8R	Linear brick elements
C4	Composition C4 plastic explosive
CDP	Concrete Damaged Plasticity
CEL	Coupled Eulerian-Lagrangian
CFD	Computational Fluid Dynamics
CONWEP	Conventional Weapons Effects Program
CV	Control volume
DIC	Digital Image Correlation
DPDC	Dynamic Plastic Damage Concrete material model
EOS	Equation of state
EPX	Europlexus
ERO	Erosion
Exp	Experimental
FEA	Finite Element Analysis
FEM	Finite Element Method
FSI	Fluid-structure interaction
HCP	Hydrated Cement Paste
HJC	Holquist-Johnson-Cook material model
J-L	Jankowiak and Lodygowski configuration of CDP-model
JC	Johnson-Cook plasticity model
JWL	Jones-Wilkins-Lee
K&C	Karagozian & Case material model
Lab	Labibzadeh et al. configuration of CDP-model
MS	Mesh size
NTNU	Norwegian University of Science and Technology
PCC	Plain cement concrete
SFT	Submerged Floating Tunnel
SIMLab	Structural Impact Laboratory at NTNU

TC	Tie constraint
TNT	Trinitrotoluene (explosive)
TP	Time period

Greek letters

α	Angle of incidence
$\boldsymbol{\sigma}$, σ	Cauchy stress tensor, Stress
λ	Scale factor
ρ	Density
τ	Non-dimensional time
ε	Strain
ε_{crit}	Strain based erosion criteria

Roman letters

$\boldsymbol{v}, v$	Velocity
b	Exponential decay coefficient
E	Elastic modulus
E	Energy
e	Specific energy
E_c	Elastic modulus of concrete
E_i	Internal energy
E_k	Kinetic energy
E_{tot}	Total energy
F	Force
F	Friction coefficient
f'_c	Compression strength of concrete
f'_t	Tensile strength of concrete
i_{r+}	Specific impulse of positive phase
P, p	Pressure
R	Stand-off distance
T	Temperature
t	Time
t_a	Arrival time (of shock wave)
t_{d+}	Duration positive phase
W	Explosive mass
Z	Scaled distance

Chapter 1

Introduction

As part of the National Transport Plan (NTP) for 2018-2029 [1] it has been decided by the Norwegian parliament to improve and develop the coastal highway E39 [2]. The route runs from Kristiansand to Trondheim and connects many of the larger cities along the west coast like Stavanger, Bergen and Ålesund. Today, the stretch is approximately 1100 km long and requires seven different ferry connections, giving a travel time of about 21 hours. The ferries are time consuming and considered a bottleneck along these stretches. It has therefore been an ambition by the Norwegian government to build a continuous highway, and by that reducing the travel time by half. Building a continuous highway involves replacing the present ferry connections with bridges and tunnels. This entails crossing wide and deep fjords, e.g. the 3.7 km long and 1250 m deep crossing over Sognefjorden from Lavik to Oppedal, where new and unconventional methods are necessary. One proposal is to use a submerged floating tunnel (SFT) to achieve this (Fig. 1.1). A feasibility study has concluded that this is a viable concept [3].

There are several uncertainties associated with the concept and design of an SFT. One such uncertainty, which will be the main theme for this thesis, is the structural response in the event of an internal explosion. In particular, the local damage due to blast loading will be assessed. Considering the scale of the proposed SFT, concrete is likely to be used in the construction. Concrete has a low cost compared to other alternatives, and lot of knowledge about concrete has been accumulated over the years as it is frequently used in the building sector as well as the offshore sector.

An internal explosion in an SFT could potentially have massive repercussions. If the blast is powerful enough to produce through-thickness cracks in the tunnel walls, water could leak into the tunnel. A similar incident happened in 2015 in a subsea rock tunnel in Bremanger [4]. The tunnel suffered great damage and was partly flooded with water, after a tank truck containing 16 500 l of petrol exploded inside the tunnel. It is therefore of great importance to take a potential internal explosion into consideration in the structural design of an SFT.

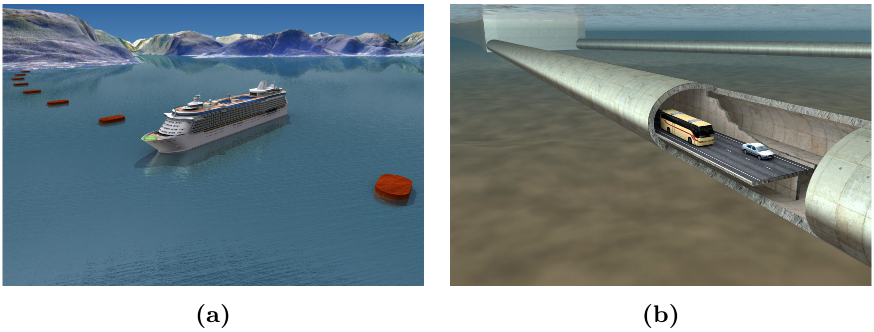

(a) (b)

Figure 1.1 – *A concept proposal of the Submerged Floating tunnel across Sognefjorden[2].*

Performing full scale tests on an SFT is not an option, both due to time and costs. It is therefore necessary to rely on small scale experiments and numerical methods. This thesis builds upon the work laid down in previous master theses by Haug and Osnes [5] in 2015, and Hillestad and Pettersen [6] in 2016. They investigated the response of concrete plates subjected to blast loading. The focus of this thesis will be to evaluate the structural response of tubular concrete structures exposed to blast loading.

Concrete is a brittle, pressure and rate dependent material, which is notoriously difficult to describe and simulate precisely. It is inhomogeneous of nature, and thereby inconsistent in its behavior, but modeled as a homogeneous entity by conventional material models. Several material models are available across various Finite Element Analysis (FEA) programs, but they differ greatly in complexity and ease of use. The more complex models require several parameters and extensive calibration. Previous master theses by Haug and Osnes, and Hillestad and Pettersen have also studied the modeling of concrete subjected to blast loading. Haug and Osnes focused on the Holmquist-Johnson-Cook (HJC) concrete model in IMPETUS Afea Solver [7], and found that it required an immense amount of tuning to get reasonable results. The Karagozian and Case (K&C) concrete damage model in LS-DYNA [8] however was relatively easy to use and gave promising results; due to time limitations, they did not have the resources to further investigate it. Consequently, Hillestad and Pettersen chose to focus on the K&C model in addition to investigating the potential of the CDP model in ABAQUS. To model the inhomogeneous behavior of concrete, two stochastic methods were also applied; one which they named the random element strength method, the other a mesoscale method. In general, the K&C model in LS-DYNA was better at simulating plain concrete, while the CDP model in ABAQUS did better in simulating reinforced concrete. In a paper written by Kristoffersen et al. [9], which this thesis also will build on, concrete pipes subjected to blast loading is simulated using Europlexus [10], performing both Lagrangian and full Fluid-Structure-Interaction (FSI) analyses. The material model used us the Dynamic Plastic Damage Concrete (DPDC) model in Europlexus. A full FSI approach proved to be superior to a pure Lagrangian approach.

For this thesis, it has been chosen to use ABAQUS and the CDP model. It is mostly due to the author's convention with the use of ABAQUS and the scripting interface it provides; the higher accuracy in simulating reinforced concrete is also a desirable attribute. An attempt to model the pressure loading based on a pure Eulerian analysis in Europlexus will also be made. An experimental study will be carried out, where small scale tests on commercially manufactured concrete pipes will be performed. Both plain cement concrete (PCC) and reinforced pipes will be assessed. During tests, pressure at various locations will be measured by pressure sensors as a tool for validation and verification of the applied loading in numerical simulations. The experimental work will act as a guide and reference to evaluate numerical models. Though, the aim is not to precisely replicate the experimental tests in the numerical simulations, but rather explore the weaknesses and strengths of existing numerical tools to describe blast loading and concrete behavior.

It should be noted that this thesis is the authors first experience with concrete as an engineering material. Concrete is thus only treated with a phenomenological approach.

An overview of the chapters in this thesis is presented below.

Chapter 2 - Literature Review

A short summary of previous research done on relevant subjects such as blast simulations, concrete modeling and other related experimental and numerical studies. Additionally, the two previous master thesis by Haug and Osnes [5] and Hillestad and Pettersen [6] will be reviewed.

Chapter 3 - Theory

The theoretical foundations of the different aspects in this thesis will be presented. This includes an introduction to fundamental blast theory and structural response to blast loads. Additionally, different methods to model blast loads and an overview of the governing equations in fluid mechanics will be given. A few aspects of Explicit finite element method which will also be highlighted.

Chapter 4 - Materials

General plasticity theory will be introduced. The mechanical properties and behavior of concrete will also be discussed more in detail. Lastly, a brief overview of the Johnson-Cook plasticity model.

Chapter 5 - Experimental Work

The introductory experimental work that was conducted to determine the properties of concrete is presented in this chapter. The experiments on concrete pipes exposed to C4 charges is also documented.

Chapter 6 - Numerical Study - Concrete Cubes

Numerical analysis of the concrete cube compression tests using the general CDP model in ABAQUS. A parameter study is performed.

Chapter 7 - Numerical Study - Concrete pipes

Numerical analysis of concrete pipes subjected to blast loading. Different parameters are altered to investigate the change in qualitative behavior. A closer look will be taken on the modeling of the blast load.

Chapter 8 - Concluding Remarks

A summary of the results and conclusion.

Chapter 9 - Further Work

A proposal of further improvements and problems to be addressed.

Chapter 2

Literature Review

A short summary of previous experimental and numerical research done on subjects related to this thesis will be given in this chapter. The previous work laid down in the master theses by Haug and Osnes [5] from 2015 and Hillestad and Pettersen [6] will also be presented.

2.1 Previous research

The most relevant previous research that has been conducted is the work by Kristoffersen et al. [9]. Both an experimental and a numerical study was performed on the same concrete pipes that will be assessed in this thesis. The FEA software Europlexus was used to perform both Langrangian and fully coupled FSI analyses. The material model used for the concrete was the Dynamic Plastic Damage Concrete (DPDC) model implemented in Europlexus, which includes both rate sensitivity and isotropic damage [10]. The Lagrangian approach was modeled by applying a pressure-time history to the inner surface of the pipe; the magnitude of the pressure is based on the charge size, distance to the charge and the angle between the elements surface normal and the vector between the surface and the charge. The Friedlander equation is used to describe the pressure-time history. In the FSI approach, the charge is modeled using the Jones-Wilkins-Lee (JWL) equation of state. The simulations provided good qualitative results; the fully coupled simulation was in better agreement with the experimental results, yet it is argued that the Lagrangian analyses are still useful despite their non-conservative results. The FSI simulation was able to account for confinement and reflections, thus gave a higher level of accuracy than the pure Lagrangian simulation, and it was also able to reproduce the cracks in a precise manner. Adaptive mesh refinement was said to aid in the description of crack propagation. In this paper no effort was made to calibrate the material model.

In another paper written by Kristoffersen et al. [11], concrete plates with and without reinforcement were tested in a shock tube. A numerical study was done on the plates using the finite element software ABAQUS/Explicit. The plates were modeled using 8-node linear brick elements with reduced integration (C3D8R) and assigned material properties by the Concrete Damaged Plasticity model in ABAQUS. For the reinforcement steel the Johnson-Cook (JC) elastic-viscoplastic material model is used and they are modeled by two-node linear beam elements (B31) and embedded in the concrete. Loading was applied uniformly over the plate, where the pressure-time history was defined by the Friedlander curve calibrated to the experimental data by a least-squares curvefit. The simulations gave decent qualitative predictions; it was seen that the damaged areas aligned with the reinforcements as was also seen in the tests. A case study was also performed on a circular and rectangular cross-section of an SFT. In this case, the blast was simulated by the CONWEP model implemented in ABAQUS. The circular cross-section appeared to be the better choice for an SFT.

A third paper by Kristoffersen [12] also looks at concrete plates tested in shock tube. In this paper a comprehensive material test for B20 and B45 concrete was also carried out, performing cube compression, cylinder compression and tensile splitting tests. As expected there was some statistical scatter in the results. The steel reinforcements were also tested to get the stress-strain relationship. Concrete plates with and without reinforcements were then tested in the shock tube. In the experiments, the B20 slabs suffered less cracking than expected compared to the B45 slabs. It was shown that the tensile strength is determining in the destruction of the plates, and the behavior of the B20 slabs is attributed to the tensile strength being similar to the B45 slabs. Adding reinforcements reduced the deformation and directed the cracks along the reinforcements. In the numerical simulations LS-DYNA was utilized, with the K&C concrete model. The simulations gave decent results, and it was found that the tensile strength was very influential on the qualitative results. The authors also further suggest to employ a mesoscale model to get more accurate crack patterns and detailed results.

Tiwari et al. [13] assessed the dynamic response of a tunnel in soil subjected to internal blast loading. The analysis is performed using ABAQUS, where the concrete pipe is modeled using the CDP model and the reinforcement is modeled using Johnson-Cook plasticity model. To describe the pressure-volume relationship of the explosive the John-Wilkins-Lee equation of state is used. The simulation is carried out using a coupled Eulerian-Lagrangian analysis, where the Eulerian description is used to model the domain in which the explosive propagates and the Lagrangian domain is the concrete tunnel and surrounding soil. A parametric sensitivity study was performed on the tunnel lining thickness, charge weight and angle of internal friction in the soil. The pressure from the blast on the inner surface of the tunnel was seen to increase with the charge weight, and plastic strain in the tunnel was also seen to increase.

A study by Burgan et al. [14] investigates the use of coupled and uncoupled analysis techniques in the assessment of blast wall response to explosions. The analyses are performed using ABAQUS. In the purely Lagrangian analysis the blast load is applied uniformly to the wall, where the pressure-time history is in a simplified multi-linear form. In the uncoupled analysis, a 1D and 2D Eulerian analysis was carried out to determine the pressure distribution and peak pressure on the wall. To model the loading an initial particle velocity was defined over a part of the Eulerian domain. The loading is then applied to the Lagrangian model. In the coupled analysis a 3D Eulerian domain is created and the Lagrangian wall is placed within the domain. It is found that with large structural deformations, there are significant differences between the uncoupled and coupled formulation, with the coupled being more accurate.

2.2 Previous master theses

Much of the work in this thesis will build upon and take inspiration from the previous master theses by Hillestad and Pettersen [6] in 2016 and Haug and Osnes [5] in 2015. In both of the theses concrete plates were subjected to a blast loading in the SIMLab shock tube facility. Haug and Osnes tested a total of 5 plates with a thickness of 50 mm subjected to different blast loads, where one of the plates was perforated by a projectile before testing to investigate the effect of initial damage to the plate (Table 2.1). Hillestad and Pettersen tested in total four plates, one plain concrete and one reinforced plate subjected to a maximum pressure of approximately 12 bar, in addition to one plain concrete and one reinforced plate subjected to a maximum pressure of approximately 17 bar (Table 2.2).

Haug and Osnes used the FEM programs IMPETUS and LS-DYNA to perform Lagrangian analyses of the concrete plates, in addition to Europlexus to perform coupled Eulerian-Lagrangian simulations of the shock tube and loaded plate. They focused mainly on the Holmquist-Johnson-Cook (HJC) model in IMPETUS, but it required considerable calibration for the simulations to resemble the physical tests. Yet, it overestimated the capacity of the plates and proved to be too ductile in general. They also performed a

Table 2.1 – *Overview of experimental work by Haug and Osnes [5].*

Haug and Osnes

Plate #	P_r [bar]	*Comments*
1	7.4	Only minor surface cracks
2	7, 11.99, 12	Subjected to three blasts, only surface cracks.
3	6.62	Was perforated by four 7.62 mm bullets before the blast. No additional damage.
4	29	Complete failure.
5	18.78	Deep cracks through the thickness.

small numerical study using the K&C model in LS-DYNA, to see if it gave improved results. According to them, the K&C model showed potential and required significantly less tuning, needing only three input parameters. It overestimated the concrete strength slightly; a 60% increase in loading was necessary to collapse the plate, but crack patterns were well captured. The effects of FSI to the shock tube experiments were also investigated by the use of the Europlexus software. They argued that FSI effects were small while computational costs were high, making an FSI analysis redundant to this particular problem.

Hillestad and Pettersen did a comprehensive numerical study where they used the FEM programs LS-DYNA and ABAQUS. They performed different material tests of concrete, including cube compression, tensile splitting and three point bending. The material tests were then modeled using the K&C Concrete Damage Model in LS-DYNA and the Concrete Damage Plasticity model in ABAQUS; both models were able to represent the main characteristics of the experiments. They also employed two different statistical approaches to model concrete. The first, named the random element strength method, gives a random strength to each element according to a normal distribution. The second method was a mesoscale method, which divides a finite element mesh into aggregates and cement, to more accurately represent the physical mesostructure of the concrete. It was seen that the random element strength method gave less ductile behavior for the K&C model, while the CDP model saw little change in softening behavior. Furthermore, it was highly dependent on the strength of the weakest elements and it was also quite mesh sensitive, requiring calibration for various mesh

Table 2.2 – *Overview of experimental work by Hillestad and Pettersen [6].*

Hillestad and Pettersen

Plate #	P_r [bar]	*Comments*
1	12.05	Plain concrete plate. Surface cracks.
2	12.27	Reinforced plate. Surface cracks.
3	16.55	Plain concrete plate. Surface cracks.
4	17.27	Reinforced plate. Surface cracks.

sizes. The mesoscale model was able to reproduce the same cube strength distribution as seen in the experiments and gave reasonable crack patterns. For the simulations of concrete plates, the extent of cracking was generally exaggerated in both LS-DYNA and ABAQUS, though the crack patterns were in agreement with experiments. LS-DYNA proved to give the best results in simulating the plain concrete pipes, while ABAQUS was more accurate in the representation of the reinforced plates. They implemented a strain-rate based erosion criteria in ABAQUS, which was seen to overly reduce the capacity of the plate. Lastly, the random element strength method and the mesoscale method was applied to the plates. The random element strength method gave little change in displacement, but was able to create more variable crack patterns. When using the mesoscale method the damage to the plate was overestimated, but the crack patterns created predicted realistic collapse mechanisms.

Chapter 3

Theory

In this chapter, the fundamental theory behind the work undergone in this thesis will be represented. The intention is to introduce basic concepts required to understand the principal parts of this thesis. Certain parts of the theory is too profound to be presented in full detail, and the reader will then be referred to further reading.

3.1 Blast and explosions

In this section, the mechanics behind the blast phenomenon will be explained.

3.1.1 Blast phenomena

A blast is defined as a pressure disturbance caused by a sudden release of energy [15]. Blasts are often associated with the detonation of an explosive charge. The term detonation refers to a very rapid and stable chemical reaction, i.e. combustion, which creates a supersonic exothermic front travelling through a medium that drives a shock front. However, there exists other blast sources than chemical reactions. In large, an explosion can be categorized as either chemical, nuclear or physical [16]. Nuclear explosions are created by the rapid release of energy caused by a chain reaction of fission processes in the fissile elements in the bomb (e.g. uranium-235 or plutonium-239) [17]. It can also be caused by a fusion process, but the latter often involves a fission process to initiate. Examples of a physical explosion would be a pressure vessel bursting, causing a rapid expansion of compressed air, or a rapid phase transition of a liquid to a gas. Chemical explosions is the most common and is what defines traditional explosives such as TNT and C4.

The energy released from an explosion expands rapidly and compresses the surrounding air, creating a blast wave radiating away from the blast source. Shock waves are high-pressure blast waves that propagate through a medium, e.g. air, at supersonic velocities. The wave is driven by the discontinuity in pressure, creating a disequilibrium between the highly compressed air in the blast wave and the undisturbed air in front. As the wave expands its strength decreases, its duration lengthens and it decelerates until reaching equilibrium with the surrounding air.

Shock waves are characterized by an instantaneous rise in pressure, called the compression phase, followed by a decay in pressure, an expansion wave, where the pressure returns to its ambient value. It should be noted that the pressure of a shock wave is overpressure, since it is relative to ambient conditions. After being compressed, the momentum of the gas causes an overexpansion and creates suction, called a negative phase (Fig. 3.1). As a result, at locations relatively far away from the point of detonation, pressures below the ambient pressure may be experienced after the passing of the shock wave.

The undisturbed shock wave is often referred to as the incident wave, and its pressure referred to as the incident pressure. When the blast wave interacts with a structure, it is reflected and reinforced, thus known as the reflected wave, and its pressure known as reflected pressure. The peak reflected overpressure, p_r, is always greater than the peak incident overpressure, p_{so}, from the same explosion. It has been shown to be up to 13 times higher [16].

The reflected overpressure is the actual loading to be considered in the blast-resistant design of a structure. A semi-empirical approach which is commonly used to model the pressure-time history is given by the modified Friedlander-equation,

$$p_r(t) = p_{r,max}\left(1 - \frac{t - t_a}{t_{d+}}\right)\exp\left(\frac{-b(t - t_a)}{t_{d+}}\right), \tag{3.1}$$

where $p_{r,max}$ is the peak reflected overpressure, t_a is the arrival time of the shock wave, t_{d+} is the duration of the positive phase and b is the exponential decay coefficient [18] (Fig. 3.1).

The magnitude and duration of the shock wave are significant parameters when considering the effect of a shock wave on a structure. By integrating

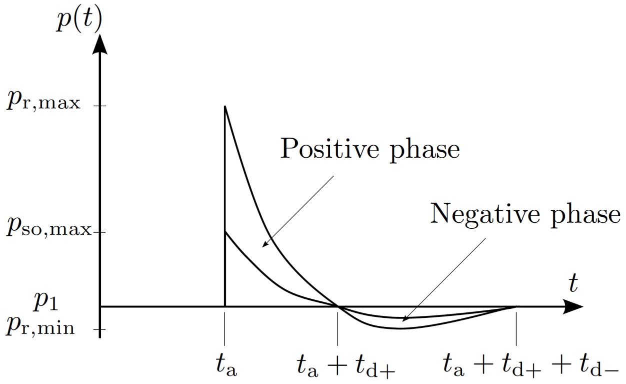

Figure 3.1 – *Typical incident and reflected pressure time histories; p_1 is the ambient pressure and t_{d-} is the duration of the negative phase. Adopted from V. Aune [18].*

the area underneath the pressure-time curve, the specific impulse is obtained. Impulse acted upon a body creates an equivalent change in momentum of that said body [19]. Thus, it is a measure of the energy from an explosion which acts upon a structure. By inserting the modified Friedlander equation (Eq. (3.1)) in the expression for the specific impulse (Eq. (3.2)), an analytical expression can be found. The specific impulse of the positive phase can thus be given as

$$i_{r+} = \int_{t_a}^{t_a+t_+} p_r(t)dt \tag{3.2}$$

$$= \frac{p_{r,max} t_{d+}}{b^2} \left[b - 1 + e^{-b} \right] . \tag{3.3}$$

The magnitude of the peak reflected overpressure is also dependent on the angle of incidence α. The loaded surface will experience the maximum reflected pressure when the blast wave impacts perpendicular to the surface, a so-called head-on pressure loading (Fig. 3.2a). Conversely, when the loaded surface is parallel to the path of the shock front, only loading from the incident pressure is applied. This scenario is dubbed a side-on loading (Fig. 3.2b). As introduced by Randers-Pehrson and Bannister [20], the effective pressure on a surface is thus given as a function of α by the following relation

$$p(t) = p_{so}(t)\left[1 + cos(\alpha) - 2cos^2(\alpha)\right] + p_r(t)cos^2(\alpha) \quad \text{for} \quad cos(\alpha) \geq 0 \tag{3.4}$$

$$p(t) = p_{so}(t) \quad \text{for} \quad cos(\alpha) < 0. \tag{3.5}$$

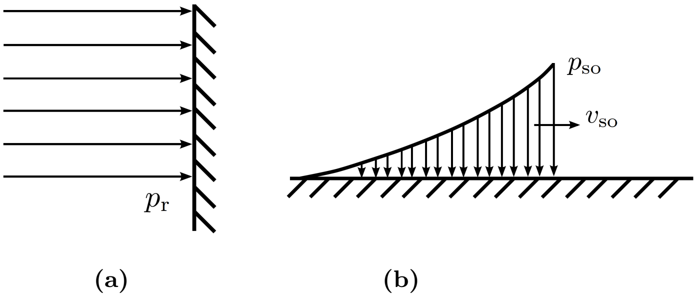

Figure 3.2 – *Illustration of head-on loading and side-on loading, adopted from V. Aune [18]. (a) head-on loading* ($\alpha = 0°$) *and (b) side-on loading* ($\alpha = 90°$).

3.1.2 Blast environments

Depending on the positioning of the explosive in relation to the target, different explosion and loading scenarios will develop. Some basic scenarios where the explosive charge is placed external to the target will be presented, as they provide the fundamental understanding for more complicated cases. The different scenarios are characterized by the distance H the explosive charge is placed above the ground and the distance R along the horizontal axis from the center of the charge to the target.

Free airburst

In the case where $H > R$ the blast wave hits the target before anything else, and the target is hit by the incident wave from the blast (Fig. 3.3). The loading could be either side-on, head-on or somewhere in between.

Airburst detonation

If $H < R$ it is called an airburst detonation. In this scenario, the blast wave will reflect off the ground before hitting the target (Fig. 3.4). The target will

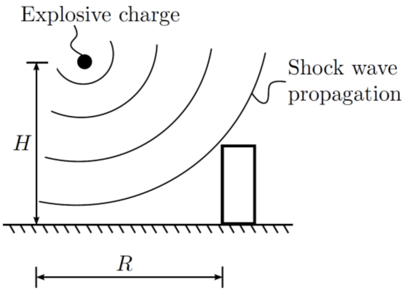

Figure 3.3 – *Illustration of a free airburst blast environment, $H > R$. Adopted from V. Aune et al. [16].*

then be hit partly or entirely by a Mach front. For these types of airbursts, Mach fronts are common. The reflected wave reaches up with the incident wave and they combine to form the path of the triple point.

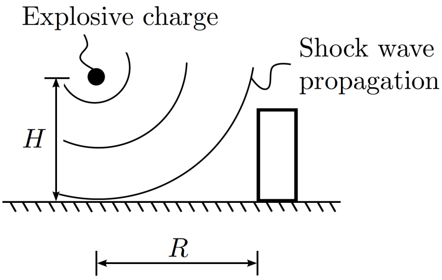

Figure 3.4 – *Illustration of an airburst blast environment, $H < R$. Adopted from V. Aune [18].*

Surface burst

If the explosive charge is located at, or very near, the ground, the blast wave will instantly reflect off the ground, thus creating a hemispherical blast wave which propagates outwards and hits the target (Fig. 3.5). The immediate reflection of the incident wave against the ground results in higher pressures, although no mach front. Under ideal conditions with a rigid ground surface, the resulting pressure would be twice as high as free airburst with equivalent explosive charge.

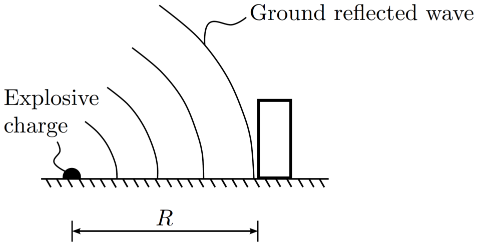

Figure 3.5 – *Illustration of a surface burst blast environment. Adopted from V. Aune [18].*

Internal blast

An explosion detonated inside a confined space will cause more damage than a similar free airburst explosion. It is caused by multiple shock reflections a higher resulting pressure on the boundaries, but will depend on the geometrical shape of the confined space [21][22].

A partially confined explosion is composed of two phases. A non-stationary phase and a quasi-static phase. The non-stationary phase consists of the initial blast followed by reflected pulses from the walls. These reflected pulses decays in magnitude and cause complex loading situations because each reflected wave will propagate and interact with other surfaces. The quasi-static phase is a result of the high pressure and high temperature gaseous products of the detonation expanding inside the structure, which is also called afterburn. It is characterized by a complex blast environment, a high pressure and has a much longer duration than the non-stationary phase.

Afterburn is a combustion process occuring when detonation products mix and react with oxidizers in the atmosphere [23]. The afterburn process appears when the appropriate conditions exist after the initial detonation, and has the potential to create a supplementary energy release. In a free airburst explosion the temperature decays rapidly with distance from the blast origin, and an afterburn process is not able to materialize. In a scenario where the explosive is detonated in confined conditions, the volume becomes pressurized over a longer time span, and temperature decays slowly. These conditions enable the afterburn process to occur.

3.1.3 Scaling

Due to the self-similar properties of the blast phenomenon, scaling of the blast parameters is a useful tool. The scalability allows data from one explosion test to be applied to a geometrically similar test which is either smaller or larger. The most usual form of scaling is the cube root scaling, also called Hopkinson-Cranz scaling. It shows the self-similarity of a blast wave by demonstrating that two explosive charges of different mass, but similar geometry and explosive material, will give geometrically equivalent blast waves at scaled distances and times if the ambient conditions are the same [16].

It is of interest to derive a relation between the peak pressure at a loaded surface at a given distance from the detonation of an explosive. One can then use the Buckingham's pi theorem to derive a relation between the different variables governing the physics of the problem. If one assumes that the governing variables are the peak pressure P, distance R, energy of the explosive E and density of air ρ. One can then further assume that there is a relation such that $\Phi(P, R, E, \rho) = 0$. The problem is only a geometrical similarity, therefore presumed invariable of time. The following dimension matrix can then be set up:

	P	R	E	ρ
kg	1	0	1	1
m	-1	1	2	-3
s	-2	0	-2	0

There are $m = 4$ quantities and the rank of the matrix is $r = 3$, thus there is $n = m - r = 1$ dimensionless variables. By balancing the units, the dimensionless quantity can then be found to be

$$\pi_1 = \frac{R}{E^{1/3}P^{-1/3}}. \tag{3.6}$$

The Buckingham pi theorem then states that there is an equivalent physical relation $\Psi(\pi_1) = 0$, which we assume to have a unique solution such that

$$\Psi\left(\frac{R}{E^{1/3}P^{-1/3}}\right) = 0 \quad \Rightarrow \quad \pi_1 = \frac{R}{E^{1/3}P^{-1/3}} = C \tag{3.7}$$

where C is a constant. The energy and weight of the explosive can simply be related through $E = eW$ where e is the energy per mass unit. Thus we can set up the relation

$$\frac{R}{W^{1/3}} = C\left(\frac{e}{P}\right)^{1/3}. \tag{3.8}$$

In Hopkinson-Cranz scaling, the aim is to determine at which distance, two charges of different size would produce the same peak pressure P (Fig. 3.6). For instance, consider two charges with mass W_1 and W_2, with the same specific energy, are measured to give the same peak pressure at locations R_1 and R_2 respectively. Then, $C\left(\frac{e}{P}\right)^{1/3}$ is constant and they can be related through

$$\frac{R_1}{W_1^{1/3}} = \frac{R_2}{W_2^{1/3}}$$

If now W_1 is chosen as the unit mass (1 kg), or equivalently E_1 as unit energy (1 kJ). This introduces the scaled distance Z which is defined as

$$Z = R_1 = \frac{R_2}{W_2^{\frac{1}{3}}} = \lambda R_2 \tag{3.9}$$

where $\lambda = 1/W_2^{1/3}$ is the scale factor. This is known as the Hopkinson-Cranz cube root scaling. It should be noted that Eq. (3.9) is preferred when comparing different types of explosions, due to possible differences in potential energy per unit mass. In a physical sense, the cube root scaling results from the spherical shape of the blast wave. As derived, the blast wave properties are proportional to the energy per unit volume; the volume, which in this instance is the volume of a sphere, is proportional to R^3.

When deriving the Hopkinson-Cranz scaling, light is shed on another relation of interest. From Eq. (3.8), at a fixed distance R for a given explosive with energy per mass unit e, the peak pressure P will be linearly proportional to the weight of the charge by the following relation

$$P = \frac{eD}{R^3}W \tag{3.10}$$

where $D = C^3$ for simplicity.

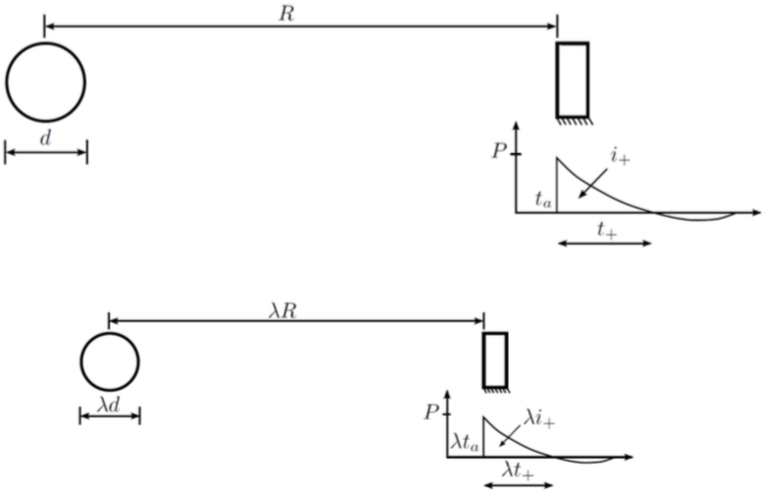

Figure 3.6 – *Hopkinson-Cranz scaling. In this figure* $R = R_2$ *and* $\lambda R = R_1$ *from Eq. (3.9). Figure adopted from V. Aune [18].*

3.2 Prediction of blast loads

There are several different approaches to determining the loading on a structure resulting from a blast. There are three main methods, empirical, semi-empirical and numerical methods. They all have their strengths and weaknesses, making them useful for different applications. This thesis will mainly focus on empirical and numerical methods.

3.2.1 Empirical methods

Empirical models are based on experimental data, and are thus limited by the scope of the experimental data on which the models are based. The most comprehensive experimental study done on this subject is the Technical report by Kingery and Bulmash [24] and the UFC-340-02 [25]. The experiments on which Kingery and Bulmash based their work, along with the equations they developed, form the groundwork of simplified models to predict blast loading from a given explosive weight at a known distance from the target. Of these models, the most commonly used is the Conventional Weapons Effects Program (CONWEP) [26] [16], which is also implemented in the ABAQUS software [27].

Empirical methods give an simplified and idealized representation of the blast loads for design purposes, but are significantly less time consuming compared to other methods. It gives a good prediction before other more complicated methods may be assessed.

3.2.2 Semi-empirical methods

Semi-empirical methods are based upon the foundation made by the empirical methods, but attempts to also consider the geometries of the problems, without employing numerical methods. Without going into further detail, the blast properties are found through empirical methods, but confined environments and reflective surfaces are accounted for by tuning blast parameters according to relevant physical experiments [16].

The same limitations apply to the semi-empirical methods as for the empirical ones. It is still less time-consuming than numerical methods, but it does not capture complex effects which may occur in more elaborate problems.

3.2.3 Numerical methods

Empirical and semi-empirical methods are mostly suited for simple geometries. Numerical methods however are very versatile and very precise given sufficiently fine discretization. They do require a much higher computational efforts than the two other methods, but with the processing power accessible today, it is still preferable in most cases.

Computational Fluid Dynamics (CFD) solves a flow problem by discretizing the computational domain into smaller computational control volumes. Over these control volumes the governing conservation equations of mass, momentum and energy are solved.

In shock wave propagation the velocity is high and viscous effects are small, thus it is assumed to be an inviscid problem. Turbulence and other viscous effects can then be neglected and the governing conservation equations are reduced to a simpler form.

3.3 Structural response to blast loads

The structural response to a load resulting from a blast wave, depends on both the magnitude and duration of the loading. There is also a strong relation between the natural frequency of a loaded structure element, which directly governs the response time, and the duration of the load function [16]. The relationship between these two factors can be divided into three loading domains, quasi-static, dynamic and impulsive loading (Fig. 3.7).

3.3.1 Impulsive loading

For an impulsive loading regime, the time scale of the loading duration is much shorter than the time scale of the system response. The loading is both applied and removed from the structure, before it has time to respond properly. Thus, the maximum response at time t_m is presumed independent of the shape of the load function.

3.3.2 Quasi-static loading

In the quasi-static regime, the time scale of the loading duration is longer than the time scale of the system response. The loading declines only slightly before maximum deformation of the system is achieved at time t_m. Response is only dependent on the peak load P_0 and system stiffness k. In similarity to the dynamic regime, the maximum response is not dependent on the loading history.

3.3.3 Dynamic loading

The dynamic loading regime falls in between the impulsive and quasi-static regime; the loading duration and the system response are at the same time scale. This creates a more complex response, which is dependent on both the loading profile and load history.

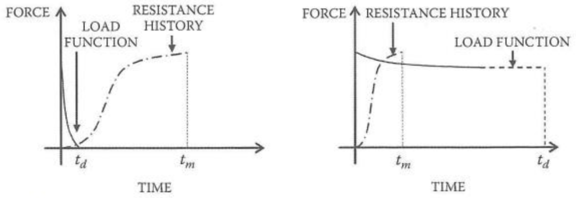

(a) IMPULSIVE

(b) QUASI-STATIC

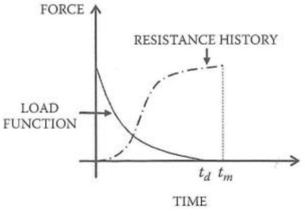

Figure 3.7 – *Illustrations of the different loading regimes. Adopted from T. Krauthammer [28].*

3.4 Blast modeling

In this section, different mathematical models to describe blasts and the resulting pressure loading will be introduced.

3.4.1 CONWEP model

To model a blast load in ABAQUS, there are several options. One of them is by the use of the CONWEP model which is implemented in the solver.

The CONWEP model estimates the following parameters based on a scaled distance: the maximum overpressure, the arrival time of the shock wave, the positive phase duration, and the exponential decay coefficient for both the incident pressure and the reflected pressure [27]. The scaled distance is determined by the distance between the loading surface and the source of the blast and the amount of explosive detonated. From the estimated parameters, the pressure-time history can be constructed. The mass of the explosive must be given in TNT equivalence.

The total pressure $p(t)$ on a surface, from a blast load, is a function of the incident pressure $p_{so}(t)$, the reflective pressure $p_r(t)$ and the angle of incidence α, defined as the angle between the surface normal and the vector from the surface to the explosion source. The total pressure is given by Eq.

(3.4) and (3.5).

The CONWEP model has some limitations however. Empirical data is only valid within a range of distances from the source, where the minimum distance is the radius of the charge. Beyond the maximum valid range, linear extrapolation is utilized to extend the maximum range where the reflected pressure decreases to zero. For distances exceeding the absolute maximum range no loading is applied. Furthermore, the CONWEP model does not take into consideration shadowing by intervening objects nor effects due to confinement [27].

3.4.2 Jones-Wilkins-Lee equation of state

An equation of state (EOS) is a thermodynamic constitutive equation relating state variables, such as for instance temperature, pressure and volume. Under a given set of physical conditions it describes the state variable of interest. An example of a commonly used equation of state is the ideal gas law. An EOS is often necessary in Eulerian analyses where the number of unknowns exceed the number of conservation equations.

The Jones-Wilkins-Lee equation of state describes the pressure generated by the release of chemical energy in an explosive [16]. It is said to only be valid for large charges [29]. The JWL equation of state can be written in terms of the internal energy per unit mass, E_m, as

$$p = A\left(1 - \frac{\omega\rho}{R_1\rho_0}\right)\exp\left(-R_1\frac{\rho_0}{\rho}\right) + B\left(1 - \frac{\omega\rho}{R_2\rho_0}\right)\exp\left(-R_2\frac{\rho_0}{\rho}\right) + \omega\rho E_m \tag{3.11}$$

where A, B, R_1, R_2 and ω are material constants depending on the type of explosive, ρ_0 is the density of the explosive and ρ is the density of the detonation products [27]. From the density, the volume V can also be described by the following relation

$$\frac{\rho_0}{\rho} = \frac{V}{V_0}. \tag{3.12}$$

The first and second term of the JWL EOS (Eq. (3.11)) represent the behavior during the detonation, while the last term describes the expanding behavior of the air after the release of energy during the detonation. The release of pressure is governed by an ignition law, which uses the detonation wave speed C_d.

In ABAQUS/Explicit, an arbitrary number of detonation points can be defined inside the explosive material. The coordinates of the detonation points must be defined together with a detonation delay time. Arrival time of detonation wave at a material point (t_d^{mp}) is calculated as the distance from the material point to the nearest detonation point divided by the detonation wave speed. The arrival time is stated as follows

$$t_d^{mp} = min\left[t_d^N + \frac{\sqrt{\left(\boldsymbol{x}^{mp} - \boldsymbol{x}_d^N\right) \cdot \left(\boldsymbol{x}^{mp} - \boldsymbol{x}_d^N\right)}}{C_d}\right] \tag{3.13}$$

where $\boldsymbol{x}^{mp}$ is the position of the material point, $\boldsymbol{x}_d^N$ is the position of the Nth detonation point, t_d^N is the detonation delay time of the Nth detonation point and C_d is the detonation wave speed of the explosive material. The minimum function in Eq. (3.13) is taken over the N detonation points.

3.5 Description of motion

The motion of a continuum, e.g. a fluid, can be described in a either a Lagrangian description or an Eulerian description [30]. They are two different ways to describe the motions of particles. In finite element formulations, the same descriptions can be applied, based on the same principles. Equally, the governing equations of motion can also be expressed in both an Eulerian and Lagrangian form.

3.5.1 Lagrangian description

In kinematics the motion of a particle is given by the time dependent position vector $\boldsymbol{x}(t)$. A finite continuum is made up of infinitely many particles. To describe the motion of the continuum one must then describe the motion of the singular particles, thus each individual particle must be identifiable. For identification, each particle is associated with a characteristic vector $\boldsymbol{\xi}$. The position vector $\boldsymbol{x}$ is such that at a chosen time t_0, $\boldsymbol{x}(t_0) = \boldsymbol{\xi}$. The motion of the whole continuum is then described by

$$\boldsymbol{x} = \boldsymbol{x}(\boldsymbol{\xi}, t). \tag{3.14}$$

The velocity for particle with label $\boldsymbol{\xi}$ is given by

$$\boldsymbol{u}(\boldsymbol{\xi},t) = \frac{d\boldsymbol{x}}{dt} = \left[\frac{\partial \boldsymbol{x}}{\partial t}\right]_{\boldsymbol{\xi}} . \tag{3.15}$$

Acceleration is found by differentiating once more. Traditionally this use of the independent variables $\boldsymbol{\xi}$ and t is called the Lagrangian description, but also referred to as the referential description. $\boldsymbol{\xi}$ is called the material coordinate. Eq. (3.14) also represents a mapping from the reference configuration to the actual configuration.

Likewise, in the discretization of a continuum in finite elements, the description of motion can be Lagrangian. Each discretized material particle is identified by a node and its motion through space and time is followed. Consequently, the mesh follows the motion of the continuum. This is the formulation most commonly used in solid mechanics, as the deformation of the solid is usually small and particles move in a predictable manner.

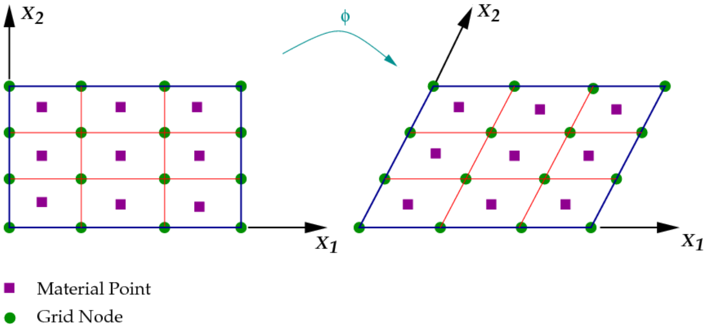

Figure 3.8 – *Lagrangian mesh motion. Figure taken from Wikiversity.org [31].*

3.5.2 Eulerian description

In some problems, the point of interest is fixed in space, e.g. a specific place or region of space. The independent variables are then the position $\boldsymbol{x}$ and time t. Eq. (3.14) can then be solved for $\boldsymbol{\xi}$, yielding

$$\boldsymbol{\xi} = \boldsymbol{\xi}(\boldsymbol{x},t). \tag{3.16}$$

This is the identifier of the material point which is at the place $\boldsymbol{x}$ at time t. With Eq. (3.16) $\boldsymbol{\xi}$ can be eliminated from Eq. (3.15) giving

$$\boldsymbol{u}(\boldsymbol{\xi},t) = \boldsymbol{u}\left[\boldsymbol{\xi}(\boldsymbol{x},t),t\right] = \boldsymbol{u}(\boldsymbol{x},t). \tag{3.17}$$

For a fixed $\boldsymbol{x}$, Eq. (3.16) describes the velocity at position $\boldsymbol{x}$ as a function of time. For a given t Eq. (3.16) expresses the velocity field at time t. The use of the independent variables $\boldsymbol{x}$ and t is called the Eulerian description, but may also be called the spatial description. $\boldsymbol{x}$ is sometimes referred to as the field coordinate. Through Eq. (3.14) all quantities given in material coordinates can be converted to field coordinates.

The Eulerian description is favored when dealing with problems related to fluid mechanics. Especially when dealing with steady flows, i.e. independent of time, the velocity field is the subject of interest, the paths of the individual particles are of secondary importance. With the use of finite elments with a Eulerian description, it is thus the computational domain which is discretized and the continuum is free to move through the static computational domain. The field variables are solved at each node whether material is present or not.

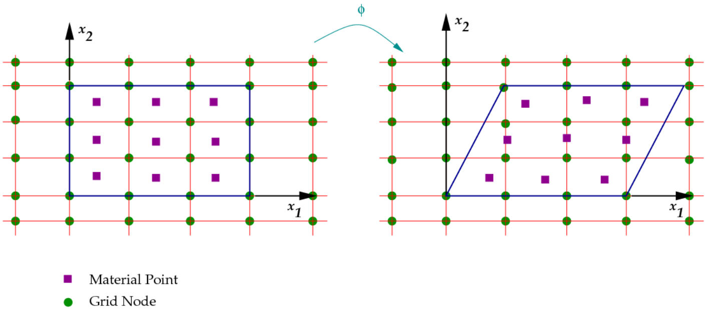

Figure 3.9 – *Eulerian mesh motion. Figure taken from Wikiversity.org [31].*

3.6 Explicit Finite Element Analysis

Finite Element Analysis (FEA) and continuum mechanics is a comprehensive topic. The basic theory of Explicit FEA is presumed known to the reader, but certain more advanced techniques and methods which will be applied in this thesis will be introduced.

3.6.1 Element erosion

To describe fracture propagation in a material in Explicit FEA, element erosion is commonly used [32]. When a preset fracture criterion is met in an integration point, the stress in the element is set to zero. The element is removed from the simulation when all or a user-defined number of integration points in the element has failed. In this manner, the crack propagation can be described in a qualitative way. Element erosion can be regarded as an abrupt strain softening process, since the element is removed and consequently so are the stresses in the element.

Finite element problems involving strain softening can often lead to strains localizing; as a result a highly mesh sensitive solution. Mesh sensitivity is a problem for strain softening materials. The localization of strains are determined by the characteristic element size. When the element size is reduced to zero, the plastic dissipation also goes to zero, which is an unphysical solution. Materials exhibiting strain softening are therefore dependent on a regularization technique to improve the numerical solution of the problem, for instance by introducing a characteristic length scale other than the element size or by introducing a viscoplastic material model.

3.6.2 Eulerian mesh deformation

In ABAQUS/Explicit it is possible to employ a Coupled Eulerian-Lagrangian analysis, where Eulerian material can interact with Lagrangian elements through general contact.

The algorithm used in ABAQUS/Explicit for performinig Eulerian analyses is known as Lagrange-plus-remap; using an operator split of the governing equations, giving a traditional Lagrangian phase of the time increment followed by an Eulerian transport phase of the time increment [27]. During the Lagrangian phase, nodes are temporarily fixed within the material and elements deform with the material. During the Eulerian phase deformation is suspended and elements with significant deformation are automatically remeshed. The technique applied in ABAQUS/Explicit is thus not a true Eulerian approach.

3.7 Computational Fluid Dynamics

Computational Fluid Dynamics (CFD) is a useful tool in engineering and research. It has become widely used in industry with the advancements in computational power and numerical methods. CFD is used to numerically analyze and solve problems involving fluid flow. The theory in this section will be influenced by the works of J. H. Spurk and N. Aksel [30] and J. Blazek [33] in addition to personal notes.

3.7.1 Conservation laws

The governing equations in fluid dynamics builds upon the principles of conservation of mass, momentum and energy. Conservation of a quantity implies that its total variation inside an arbitrary region Ω can be described as the net amount of the quantity moving across the boundary.

Consider a geometrically closed, imaginary region in space Ω, with boundary $\partial\Omega$. This is often referred to as a control volume (CV). A material with scalar quantity $b(\boldsymbol{x}, t)$ is moving in space with flux $\boldsymbol{j}(\boldsymbol{x}, t, b)$, where $\boldsymbol{x}$ is the position vector and t is time. Note that the description used is Eulerian. For sources and sinks inside the region Ω a general production density $q(\boldsymbol{x}, t)$ is prescribed. Now, the rate of change in the total amount of quantity b in Ω is equal to *minus* what is disappearing over the boundary *plus* what is produced. Thus the conservation law on integral form is given as

$$\underbrace{\frac{d}{dt}\int_{\Omega} b(\boldsymbol{x}, t) dV}_{\text{rate of change}} + \underbrace{\int_{\partial\Omega} \boldsymbol{j}(\boldsymbol{x}, t, b) \cdot \boldsymbol{n} dS}_{\text{flux}} = \underbrace{\int_{\Omega} q(\boldsymbol{x}, t) dV}_{\text{production}} . \tag{3.18}$$

If b and $\boldsymbol{j}$ are sufficiently smooth functions of $\boldsymbol{x}$ and t, the derivative with respect to t can be moved under the integral sign and the Divergence Theorem can be applied to the flux term. This yields

$$\int_{\Omega} \left(\frac{\partial b}{\partial t} + \nabla \cdot \boldsymbol{j} - q \right) dV = 0. \tag{3.19}$$

If the expression inside the integral is continuous the conservation law can be written in the following differential form

$$\frac{\partial b}{\partial t} + \nabla \cdot \boldsymbol{j} - q = 0. \tag{3.20}$$

One cannot always move the differential operator inside the integral, thus the integral formulation is more general and fundamental than the differential formulation.

The continuity equation

From Eq. (3.20) the governing equation for conservation of mass, the continuity equation can be easily derived in differential form by using the density

ρ as the conserved quantity. In this case the flux term is the amount of mass transported across a surface, which is linear proportional with the velocity field $\boldsymbol{v}$, thus $\boldsymbol{j} = \rho\boldsymbol{v}$. As no mass is produced or destroyed, $q = 0$. The continuity equation is stated as follows

$$\frac{\partial \rho}{\partial t} + \nabla \cdot (\rho \boldsymbol{v}) = 0 \tag{3.21}$$

and it ensures the conservation of mass at all times.

Navier-Stokes Equation

To derive the conservation of momentum equation, the conserved quantity is thus $b = \rho\boldsymbol{v}$. The flux term becomes $\boldsymbol{j} = \rho\boldsymbol{v} \otimes \boldsymbol{v}$ which is now a tensor. Momentum of an object is changed when acted upon by a force, thus the production term is the sum of surface and body forces on the CV. The production term then becomes $q(\boldsymbol{x}, t) = \rho\boldsymbol{f}_b(\boldsymbol{x}, t) + \boldsymbol{f}_s(\boldsymbol{x}, t)$. The surface forces only act on the boundary of the CV and can be rewritten by the Cauchy stress tensor $\boldsymbol{f}_s = \boldsymbol{\sigma} \cdot \boldsymbol{n}$. The differential form of the momentum conservation equation then becomes

$$\frac{\partial (\rho \boldsymbol{v})}{\partial t} + \nabla \cdot (\rho \boldsymbol{v} \otimes \boldsymbol{v}) = \rho \boldsymbol{f}_b + \nabla \cdot \boldsymbol{\sigma}. \tag{3.22}$$

The Cauchy stress tensor can be further decomposed into a hydrostatic and deviatoric part,

$$\boldsymbol{\sigma} = \frac{1}{3}\mathrm{tr}(\boldsymbol{\sigma}) + \boldsymbol{\tau} = -p\boldsymbol{I} + \boldsymbol{\tau}. \tag{3.23}$$

where p is the pressure and $\boldsymbol{I}$ is the identity matrix. Until now, the equations stated holds for continuum of all types, solid or liquid. Further, assumptions for a fluid will be made. The deviatoric stress tensor $\boldsymbol{\tau}$ can be expressed by a constitutive model of viscous flow related to the shear strain. This gives

$$\boldsymbol{\tau} = 2\mu\boldsymbol{\epsilon'} \quad \text{where} \quad \boldsymbol{\epsilon'} = \boldsymbol{\epsilon} - \frac{1}{3}tr(\boldsymbol{\epsilon'}) \tag{3.24}$$

and μ is the viscosity. The tensor $\boldsymbol{\epsilon}$ is defined as the symmetric rate of deformation tensor and is given by

$$\boldsymbol{\epsilon} = \frac{1}{2}\left(\nabla \otimes \boldsymbol{v} + (\nabla \otimes \boldsymbol{v})^T\right). \tag{3.25}$$

By inserting Eq. (3.24) and Eq. (3.25) in Eq. (3.22) the general Navier-Stokes equation for compressible Newtonian viscous fluid is yielded

$$\frac{\partial(\rho \boldsymbol{v})}{\partial t} + \nabla \cdot (\rho \boldsymbol{v} \otimes \boldsymbol{v}) = -\nabla p + \mu \Delta \boldsymbol{v} + \frac{1}{3}\mu \boldsymbol{v}(\nabla \cdot \boldsymbol{v}) + \rho \boldsymbol{f}_b. \tag{3.26}$$

Conservation of energy

From Eq. (3.20) the energy conservation equation can also be derived. In this instance it is the specific energy which is the conserved quantity, $b = \rho e = \rho(u+v^2/2)$ where u is the specific internal energy. The flux term is then related to the transport of energy and the diffusion of energy through Fick's law, thus $\boldsymbol{j} = \rho e \boldsymbol{v} - k\nabla T$ where T is the temperature and k is the diffusivity. Production of energy is the rate of work exerted on the system by external and internal forces plus heat sources, thus $q = \rho \boldsymbol{f}_b \cdot \boldsymbol{v} + (\boldsymbol{\sigma} \cdot \boldsymbol{n}) \cdot \boldsymbol{v} + \dot{q}_h$. By decomposing the Cauchy stress tensor into a hydrostatic and deviatoric part as before and using the definition of enthalpy $h = e + p/\rho$ gives the conservation law of energy in the differential form

$$\frac{\partial(\rho e)}{\partial t} + \nabla \cdot (\rho h \boldsymbol{v} - k\nabla T) = \rho\left(\boldsymbol{f}_b \cdot \boldsymbol{v}\right) + \nabla \cdot (\boldsymbol{\tau} \cdot \boldsymbol{v}) + \dot{q}_h. \tag{3.27}$$

3.7.2 Finite Volume Method

A common method used in many commercial CFD codes is the Finite Volume Method (FVM). The Finite Volume Method uses the conservation laws on their integral form. In similarity with FEA, the fluid domain is discretized into an arbitrary number of polyhedral control volumes. The divergence terms, or surface integrals in the integral form, in the conservation equations (Eq. (3.22), (3.26) and (3.27)) are approximated by the sum of fluxes crossing the individual faces of the control volume. The type of numerical scheme which is used to calculate the fluxes determines the accuracy of the spatial discretization. A common scheme is the cell-centered scheme, where flow quantities are stored at the geometrical centers of the grid cells. Accordingly, the control volumes are identical to the grid cells.

One of the advantages of the FVM is the flexibility. The implementation to both structured and unstructured meshes is simple, and makes it suitable for complex geometries. Furthermore, as the FVM is based on the conservation laws, the numerical scheme also guarantees the conservation of mass, momentum and energy.

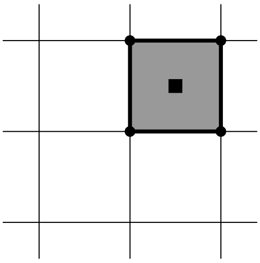

Figure 3.10 – *Example of a cell centered control volume in a structured mesh grid. Inspired by J. Blazek [33].*

Chapter 4

Materials

In this chapter, a basic introduction to plasticity theory in addition to mechanical properties and behavior of concrete will be given. Lastly, the Johnson-Cook plasticity model will be presented.

4.1 Theory of plasticity

Many materials, especially metals, are known to have an elastic behavior. A material is elastic if the deformation is reversible [34] [32]. However, the elastic behavior is often limited to small strains. Upon reaching a certain stress level, the material will start to deform irreversibly, i.e. plastic deformation, and adopt a nonlinear behavior. This limit stress level is called the yield limit. To model the characteristics of a material, constitutive relations have been developed which implements all the factors influencing the stress in a material. For an elastic-plastic material, the stress-strain relationship in the elastic domain is governed by Hooke's law, $\sigma = E\varepsilon$, while a more intricate constitutive equation is often used in the plastic domain.

There are three main components which build the foundation of plasticity theory, the yield criterion, the flow rule and the work-hardening rule. The transition from the elastic to the plastic region is governed by the yield criterion. The yield can be mathematically defined by a yield function f and plastic deformations take place for

$$f(\boldsymbol{\sigma}) = 0. \tag{4.1}$$

The yield function is written on the form

$$f(\boldsymbol{\sigma}) = \varphi(\boldsymbol{\sigma}) - \sigma_Y \leq 0 \tag{4.2}$$

where $\sigma_{eq} = \varphi(\boldsymbol{\sigma})$ is the equivalent stress and σ_Y is the flow stress or yield stress. The equivalent stress may be defined differently depending on the yield criterion. The elastic domain is described by the inequality $f(\boldsymbol{\sigma}) < 0$, $f(\boldsymbol{\sigma}) > 0$ is not defined.

As the material undergoes plastic deformation the yield strength increases, which is called work hardening. This may be introduced in Eq. (4.2) by writing the yield stress as a function of a hardening variable $R = R(p)$, where p is plastic deformation. This gives the following equation

$$f(\boldsymbol{\sigma}, R) = \varphi(\boldsymbol{\sigma}) - \sigma_Y(R) \leq 0 \tag{4.3}$$

where $\sigma_Y(R) = \sigma_0 + R$ is the flow stress of the material and σ_0 is the initial yield stress. As plastic deformation p increases, the isotropic hardening variable R and thus σ_Y increases as well (Fig. 4.1).

During plastic deformations mechanical energy is assumed dissipated as heat. The plastic flow rule assures non-negative dissipation and can be expressed by the yield function f as

$$d\boldsymbol{\varepsilon}^p = d\lambda \frac{\partial f}{\partial \boldsymbol{\sigma}}, \tag{4.4}$$

where factor $d\lambda$ is dubbed the plastic parameter. Non-negative dissipation also requires a convex yield surface. This rule (Eq. (4.4)) states that the plastic strain increment vector is parallel to the gradient of the yield surface at $\boldsymbol{\sigma}$. Thus plastic flow is parallel to the outwards normal of yield surface. This particular instance is also called the associated flow rule or normality rule.

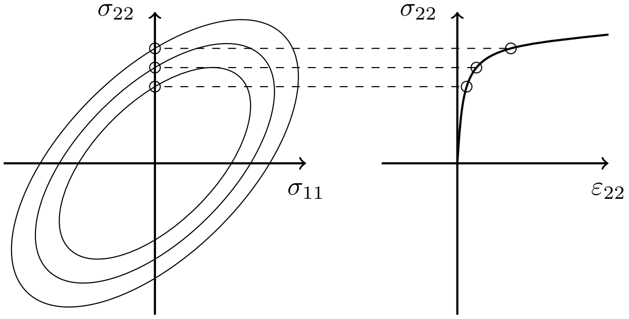

Figure 4.1 – *Isotropic hardening. The yield surface expands in stress space as the material work-hardens.*

4.2 Concrete

Concrete is a material which is frequently used in structural applications. It has several properties which makes it a favorable choice in many constructions. It is a durable material and has a low permeability [35], two important qualities when used for constructions in direct contact with water, such as for instance dams, canals, offshore platforms, or in this case an SFT. Other factors which makes concrete preferable are the low cost and its versatility in terms of size and shape. However, the behavior of concrete is slightly more complex and irregular compared to other structure materials such as aluminum and steel. To get a more profound understanding of the behavior of concrete, it is imperative to take a closer look at the macro- and microstructure. In this chapter some fundamental theory of concrete will be presented, going through the structure, the mechanical behavior and failure modes. Also, the concrete material model used in ABAQUS will be introduced. The theory in this section is greatly influenced by the work of W.-F. Chen [36], P.K. Mehta and P.J.M. Monteiro [37] and A. Neville [38], the reader is referred to these works for a more comprehensive understanding on the topic.

4.2.1 The structure of concrete

Concrete is a highly heterogeneous material. It consists mainly of two different phases, aggregate particles and hydrated cement paste (HCP) [37]. The particles are evenly dispersed in a matrix of hydrated cement paste (Fig. 4.2). The two phases are bound together when the cement reacts chemically with water, and potentially other additives, to form the hard matrix. This process is called the hydration of cement. Hydration is a gradual process, and as it proceeds the strength increases. When referring to the compression strength of concrete it is thus at 28 days after the hydration process started. This is chosen as a standard, the rate of the hydration process decreases over time, but still continues long after the standardized 28 days.

Numerous factors influence the strength concrete, though the most important factors are the porosity and the water-cement ratio [37][38]. In the process of making concrete, it is mixed with more water than the hydration process consumes. The excess water gives the concrete increased workability, but also decreases its strength. Water not consumed in the hydration process will remain in the microstructure pore space and weaken the concrete. Thus in general, a smaller water to cement ratio means higher strength, down to a theoretical limit.

To get a further understanding of the complexity of concrete, it is necessary to investigate the microstructure. At this level there are large variations and imperfections present, e.g. a multitude of voids in the cement. Neither the distribution of the phases nor the phases themselves are homogeneous. The HCP is composed of different types and amounts of solid phases, pores and microcaracks. The aggregate particles are mainly made up of natural gravel, crushed stone and sand, and vary thus greatly in both size, shape and physical properties. Additionally, a third phase could be said to exist, a transition zone in the interfacial region between the aggregates and the HCP. Among the three phases HCP, aggregate and transition zone, the latter is the generally the weakest [37]. Consequently, it has a great influence on the mechanical properties of concrete and is the reason for some of its main characteristics.

4.2.2 Mechanical properties of Concrete

One of the main features of concrete is its strength in compression, and brittle tensile behavior. The response under the two different loading regimes is quite different, and they will therefore be considered independently in the following section. Originally, a lot of microcracks are present in the concrete, especially in the transition zone between aggregate and mortar. During loading, it is the propagation of these microcracks that contribute to the non-linear behavior of concrete. The transition zone has a considerably lower tensile strength than the two other phases, and thus represent the weakest link in the composite system. It is the reason for the low tensile strength of concrete [36].

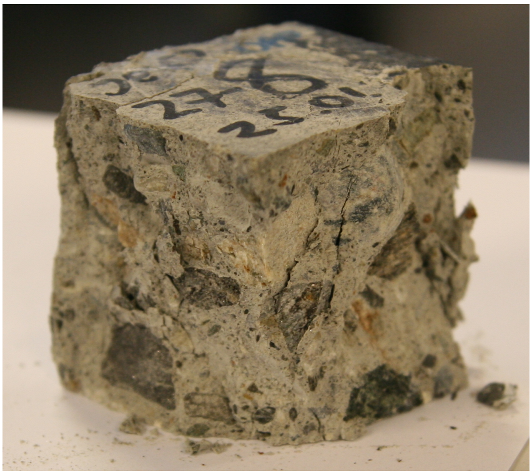

Figure 4.2 – *Concrete cube used in experiments. Aggregates embedded in the HCP matrix are visible, and fracture is seen to occur on the surfaces of the aggregates, in the transition zone.*

Compressive behavior

Under uniaxial compression the concrete will initially exhibit a near linear behavior. At around 30% of maximum compression strength f_c', the curve becomes non-linear. The non-linear behavior is mainly due to the propagation of microcracks in the transition zone [36]. The curvature increases further for higher stresses until the curve reaches its peak at f_c'. After this the stress-strain curve decreases until crushing failure occurs at ultimate strain ε_u.

The shape of the stress-strain curve is related to the propagation of microcracks in the concrete structure. In the near-linear area the cracks are virtually unchanged. The stress level at approximately 30% of f_c' is sometimes referred to as onset of localized cracking and proposed as a limit of elasticity [36]. At higher stresses, between $30\% - 75\%$ of f_c' cracks will start to extend, and for stresses above 50% of f_c', cracks at nearby aggregate surfaces will start to bridge through the mortar, called shear bond cracks [37]. For stresses above 75% of f_c' the system becomes unstable, the rate of crack propagation increases and even if the load is kept constant compressive failure can occur. The failure of concrete near f_c' is mainly caused by cracks in the mortar which connects with the cracks adjacent to aggregates. This internal damage will continue to accumulate with increasing compressive strain and the stress-strain curve starts to decrease; macroscopic cracks will also appear in the concrete.

The shape of the stress-strain curve for different compressive strengths is quite similar. In general the peak point is located around $\varepsilon = 0.002$ regardless of the strength, but higher strength concrete has a more brittle behavior with a more rapid post-peak drop (Fig. 4.3).

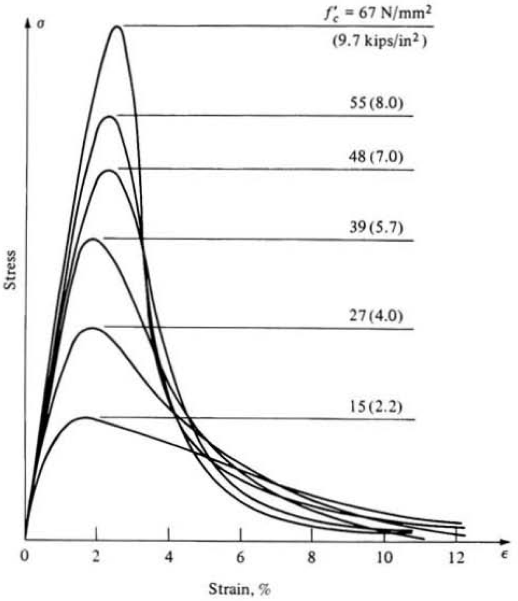

Figure 4.3 – *Stress-strain curves for concrete under uniaxial compression with different compressions strengths f'_c. Figure adopted from W. F. Chen [36].*

Tensile behavior

Under uniaxial tension, the concrete fails for a significantly lower stress than for uniaxial compression (Fig. 4.4). The shape of the stress-strain curve share similarities to the one for uniaxial compression. The curve is near linear up to around 60% of the uniaxial tensile strength f'_t; for stresses higher than this, the microcracks start to grow. The onset of unstable crack propagation starts at around 75% of f'_t. During tension, microcracks will start to propagate in a direction normal to the direction of loading. The forming and growth of new cracks will contribute to reduce the effective area over which the load is distributed. This again increases the stress at critical crack tips. In tension, the ultimate failure is eventually caused by a few bridging cracks through the mortar, in contrast to many cracks which is the reason for failure in compression. For further comparison, the tensile strength is usually 8-10 times lower than the compressive strength [39].

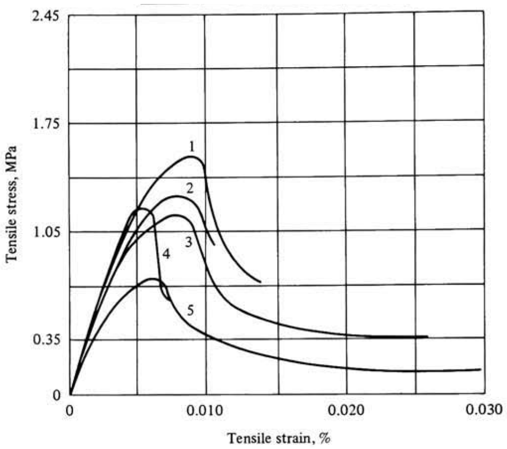

Figure 4.4 – *Stress-strain curves for concrete under uniaxial tension. Figure adopted from W. F. Chen [36].*

Biaxial and triaxial behaviour

Concrete is known to be a pressure dependent material. Confining pressures highly affect the behavior, by increasing the compressive strength and ductility. With sufficiently high confining pressures, the pressure will prevent cracks from propagating. It is observed that the compressive strength is increased under biaxial compression. Additionally, under biaxial compression the ductility of concrete increases compared to uniaxial compression.

In a biaxial compression-tension loading regime, the compressive strength decreases near proportionally to the applied tensile stress. The failure of concrete under biaxial stress happens with the fracture surface orthogonal to the direction of the maximum tensile stress or strain. Tensile strains are determining in the failure criterion and failure mechanism of concrete.

Under high confining stresses the possibility of bond cracking in concrete is greatly reduced. The failure mode goes from splitting to crushing of the HCP. The behavior of concrete also changes, it becomes less brittle and more plastic under higher confining pressures. Axial strength is observed to increase with increasing confining pressure.

Rate dependency

The response of concrete is affected by the loading rate. Mainly two factors contribute to the high strain rate effect, the viscoelastic character of the hardened cement paste and the time-dependent micro-crack growth [40]. This is argued however, and some researchers suggest that the increase of dynamic uniaxial strength is caused by the inertial confinement [41].

In general it is seen that the as the strain rate increases so does the ultimate strength. Strain rate dependence is also seen to be stronger for higher strain rates [42] [43]. It has been found that mortar is significantly rate-sensitive in the strain-rate range from $10^{-3}\,\mathrm{s}^{-1}$ to $1700\,\mathrm{s}^{-1}$. Rate dependence is weaker for strain rates below $400\,\mathrm{s}^{-1}$, above this transition rate, the dependence increases significantly.

Numerical modeling has been performed, investigating the effect of strain rate on reinforced concrete slabs subjected to blast loading in LS-DYNA [44]. It was found that including strain rate effects was important to get a good representation. Hillestad and Pettersen [6] also attempted to implement this in their model. With the lower pressure blasts, best results was obtained when strain-rate was omitted, the strength of the concrete was over-predicted giving smaller deformations than in the experiments. Though, at higher pressure blasts the correlation between experimental and simulated crack patterns improved.

4.2.3 The concrete damaged plasticity model

The Concrete Damaged Plasticity (CDP) model is designed for modeling plain and reinforced concrete in addition to other brittle materials. It is intended for use with concrete subjected to either dynamic, monotonic or cyclic loading under low confining pressures. The model builds upon concepts of isotropic damaged elasticity in combination with isotropic tensile and compressive plasticity to represent the inelastic behavior of concrete. Furthermore, it aims to capture the effects of irreversible damage associated with the failure mechanisms that occur in concrete [27] [45].

In general the model is a continuum, plasticity-based damage model. The two main failure mechanisms are tensile cracking and compressive crushing. The failure is connected the tensile and compressive equivalent plastic strains, $\tilde{\varepsilon}_t^{pl}$ and $\tilde{\varepsilon}_c^{pl}$ respectively, which governs the evolution of the yield surface. The yield function is adopted from Lubliner et al. [46] with modifications as proposed by Lee and Fenves [47] to account for different evolution of strength under tension and compression. The yield function is given by

$$F(\bar{\boldsymbol{\sigma}}, \tilde{\boldsymbol{\varepsilon}}^{pl}) = \frac{1}{1-\alpha}\left(\bar{q} - 3\alpha\bar{p} + \beta(\tilde{\boldsymbol{\varepsilon}}^{pl})\langle\hat{\bar{\sigma}}_{max}\rangle - \gamma\langle-\hat{\bar{\sigma}}_{max}\rangle\right) - \bar{\sigma}_c(\tilde{\varepsilon}_c^{pl}), \quad (4.5)$$

where $\bar{p}$ is the effective hydrostatic pressure, $\bar{q}$ is the Mises equivalent effective stress, $\bar{\boldsymbol{\sigma}}$ is the stress tensor and $\hat{\bar{\sigma}}_{max}$ is its algebraically maximum eigenvalue, i.e. maximum principal effective stress. In biaxial compression, with $\hat{\bar{\sigma}}_{max} = 0$, Eq. (4.5) reduces to the Drucker-Prager yield condition. The parameters β, α and γ are dimensionless material constants governing the pressure sensitivity and shape of the yield surface in the deviatoric plane (Fig. 4.5). Lastly, $\bar{\sigma}_c(\tilde{\varepsilon}_c^{pl})$ is the effective compressive cohesion stress.

The effective stress is defined as

$$\bar{\boldsymbol{\sigma}} \equiv \boldsymbol{D}_0^{el} : (\varepsilon - \varepsilon^{pl}) \tag{4.6}$$

where $\boldsymbol{D}_0^{el}$ is the initial, undamaged, elastic stiffness of the material. The effective stress $\bar{\boldsymbol{\sigma}}$ is related to the Cauchy stress $\boldsymbol{\sigma}$ through the scalar degradation relation

$$\boldsymbol{\sigma} = (1 - d)\bar{\boldsymbol{\sigma}}, \tag{4.7}$$

where d is the scalar stiffness degradation variable, with $d \in [0, 1]$ where 0 equals no damage. There are two damage variables, the tensile d_t and the compresssive d_c. The factor $(1 - d)$ represents the ratio of the effective load-carrying area to the overall section area. The model is based upon continuum mechanics, thus there is no tracking of cracks developing at the material integration point. Though, the scalar damage parameter d simulates cracking by reducing the overall stiffness in the model. The consequence of this is that element erosion is not directly available in the CDP-model. Alternatively one can visualize the maximum principal strain to get a notion of the cracks.

The full theory behind the CDP model is too comprehensive to be explained here in detail. For further reading please refer to the Abaqus Analysis User's Guide [27], Abaqus Theory Guide [45] in addition to the work done by Lubliner et al. [46] and by Lee and Fenves [47], on which the CDP model is based on.

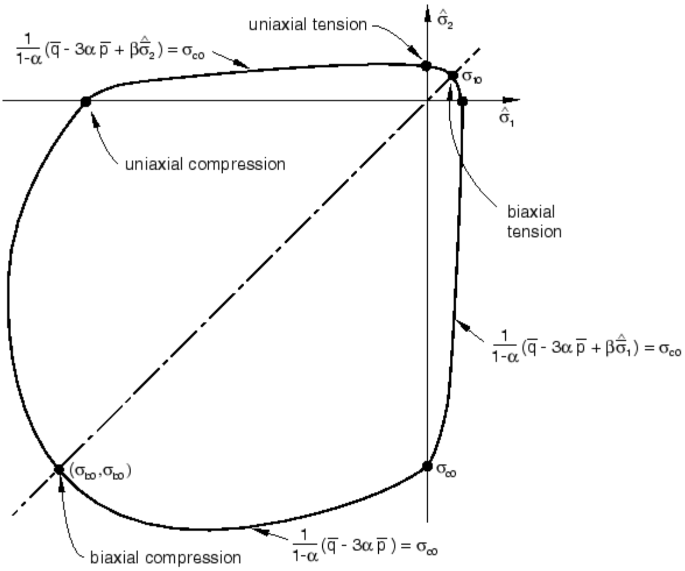
uniaxial tension
$\hat{\sigma}_2$
$\frac{1}{1-\alpha}(\bar{q} - 3\alpha\bar{p} + \beta\hat{\sigma}_2) = \sigma_{co}$
σ_{t0}
$\hat{\sigma}_1$
uniaxial compression
biaxial tension
$\frac{1}{1-\alpha}(\bar{q} - 3\alpha\bar{p} + \beta\hat{\sigma}_1) = \sigma_{co}$
$(\sigma_{b0},\sigma_{b0})$
σ_{c0}
biaxial compression
$\frac{1}{1-\alpha}(\bar{q} - 3\alpha\bar{p}) = \sigma_{c0}$

Figure 4.5 – *The yield surface of concrete in the CDP model, as described by Eq. 4.5. Figure taken from ABAQUS User's Analysis Guide [27].*

4.3 Steel

In concrete reinforcements, steel is often the preferred choice due to its ductile behavior and high tensile strength [48].

4.3.1 Johnson Cook model

To describe the plastic behavior of steel in this thesis, the Johnson-Cook (JC) constitutive model is used [34][32]. In the JC constitutive model, the equivalent stress is expressed in terms of equivalent plastic strain, plastic strain rate and temperature as

$$\sigma_{eq} \equiv (A + Bp^n)(1 + C\ln(\dot{p}^*))(1 - (T^*)^m) \quad \text{for} \quad f > 0 \tag{4.8}$$

where A is the initial yield stress, often denoted by σ_0. The term Bp^n is governing the work-hardening described by the power law, where B and n are material parameters and p is the equivalent plastic strain. The second factor describes the strain rate hardening, where C is a material constant governing the rate sensitivity and $\dot{p}^* = \frac{\dot{p}}{\dot{p}_0}$ is the dimensionless plastic strain rate where $\dot{p}_0$ is the reference strain rate. The last term describes the thermal softening where T^* is the dimensionless temperature defined as

$$T^* = \frac{T - T_0}{T_m - T_0} \quad \text{with} \quad T^* \in [0, 1]\,,$$

and m controls the temperature sensitivity. This model is also available in ABAQUS [27].

Chapter 5

Experimental Work

A series of concrete cube compression tests and blast tests on concrete pipes were carried out as part of the experimental study in this thesis. These tests will be further presented in this chapter.

5.1 Concrete cube compression tests

Concrete cubes measuring approximately 50 mm × 50 mm were cut out from original 100 mm × 100 mm concrete compression test cubes. This resulted in 8 smaller cubes per large cube. These smaller cubes were needed to perform a Digital Image Correlation (DIC) analysis, in which strains are measured during the compression in an effort to establish a stress-strain relationship for the concrete. The cubes which were not used for DIC were solely tested in a normal compression test. This type of test only gives the maximum force measured during the compression process of the cube.

5.1.1 DIC

DIC is an optical technique used for measuring strains and displacement in a material test. It can be used in both two dimensions (2D) and three dimensions (3D), but in this paper only 2D-DIC was used. To be able to track the deformation in the concrete by DIC-analysis, the cubes were painted with a speckle pattern. During the compression, pictures of the respective cubes were taken by a camera, at 2 frames/s. The DIC software eCorr was utilized to perform the DIC-analyses [49]. In eCorr, a mesh is

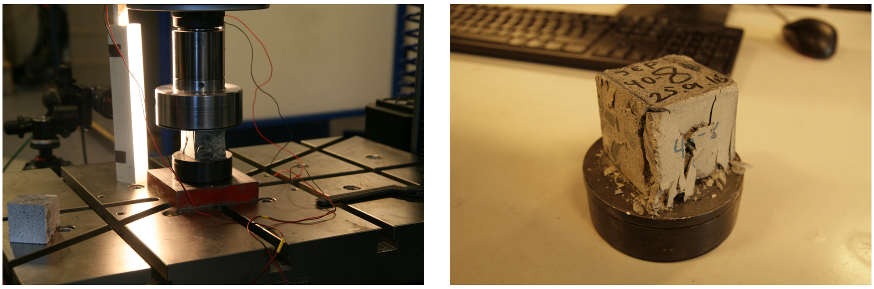

(a) *A picture of the test setup, with a concrete cube under loading.*

(b) *A picture of cube 40-8 after testing. Cracking mainly along the sides and edges.*

Figure 5.1

generated on the first image from the camera (where the specimen has no deformation). Then, subsequent pictures are used together with the mesh to track the speckles and measure strains as the specimen deforms.

During the DIC-tests, the cubes were compressed in an Instron 5985 machine, with a 250 kN load cell (Fig. 5.1a). The compression test was deformation controlled, with a rate of 2 mm/ min. Force was also logged continuously throughout the compression process. Manufacturer specifies a load measurement accuracy of ±0.5% of reading, down to 1/1000 of load cell capacity [50]. The force measurements together with the strain measurements from the DIC allows the tracking of the compressive behavior of concrete accurately. However, DIC is not intended for brittle materials like concrete, but rather more ductile ones like steel where also deformations are larger. The strains in concrete are very small, but an effort to perform a DIC-analysis was made nevertheless.

All the three cubes were successfully tested to fracture. The concrete was mainly cracking up and spalling off on the sides of the cube, where the largest tensile stresses occured (Fig. 5.1b).

Analysis

In total, three cubes were tested for the DIC. Each of the specimens were meshed up with standard 25 *pix* × 25 *pix* Q4 elements before the analysis was run (Fig. 5.2a)[49]. After completed analysis a field map visualizing the strains were applied to the mesh. This field map was very successful in identifying initiating cracks (Fig. 5.2c). However, when the cracks grew too large, the deformation from one frame to the next became too large for the

DIC to keep track. This made the mesh severely distort after the specimen started to fracture (Fig. 5.2d).

The elongation of the specimen was also measured, by lining out elongation vectors over the mesh (Fig. 5.2b). It was chosen to use multiple vectors over the mesh, 5 to be exact, so the average of them could be used to get a more general measurement of the whole specimen. Engineering strains were extracted directly from the vectors and synchronized with the force measurements from the Instron 5985 machine.

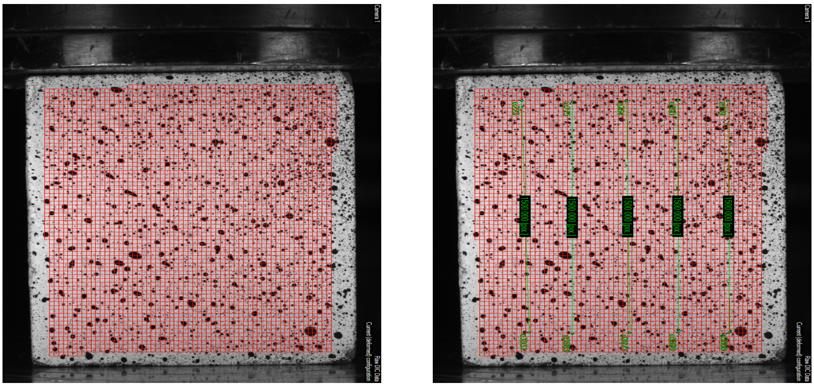

(a) *The initial mesh applied over the speckle pattern of the cube.*

(b) *The initial mesh with the 5 evenly spaced vectors drawn across the mesh.*

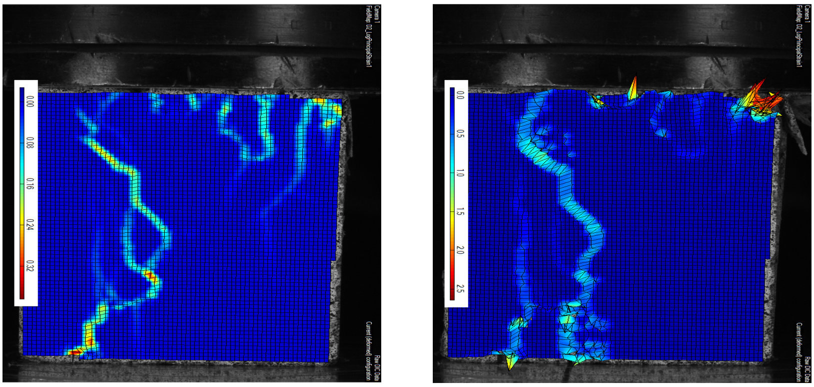

(c) *Field map of strain before the initiation of cracking. The places where cracks appear are easily seen from the brighter areas in the field map.*

(d) *Field map of strain after the initiation of cracking. The mesh is severely distorted in different places, but the cracks are still visible as the brighter areas in the field map.*

Figure 5.2 – *DIC-analysis of cube 40-8.*

Results

Force applied to the concrete cubes was recorded throughout the tests (Fig. 5.3). The initial time t_0 was set to the time instance when the beam was as closest to zero, before initiating the downward movement. This was achieved to get the curves aligned. Consequently, the time scale in Figure 5.3 does not correspond to the true time of the experiment. Furthermore, the curves are only drawn to the point of maximum displacement. The trend is similar for all the curves, as time and displacement proceeds the force increases. Eventually, the slope declines, a peak is reached and the force drops abruptly. Though, after the rapid drop, the curves start to flatten out again and soon after the experiment is terminated.

From the DIC-analysis, the engineering strain was extracted from the vectors which were drawn across the mesh. The elongation curves for the different vectors agree well up until a certain point, after this the the strain measurements for each of the vectors in a specimen starts to diverge significantly (Fig. 5.4a). This is caused by the mesh becoming distorted by the large deformations that occur together with the initiation of fracture. It becomes futile to attempt measuring any strains after this. The maximum force is measured shortly after the initiation of fracture, implying that fracture is closely connected to the yielding of the concrete.

The strain measurements up until fracture gave reasonable results, after fracture they were not of much use. Therefore, a cut-off value for the strain and force data was chosen to be when the statistical variance between the strain measurements exceeded 5×10^{-6}, which correlated well with the initiation of fracture (Fig. 5.4a). The maximum force was included in the measurements before the cut-off value was reached, for all the tests. The stress-strain

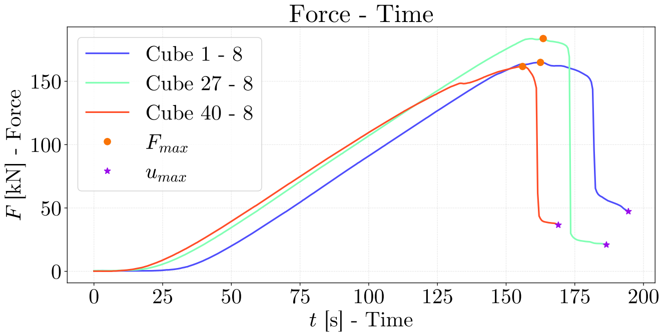

Figure 5.3 – *Force curves measured from DIC-tests.*

curve is therefore able to give experimental results up to maximum stress. The stress given is the engineering stress, where the area used is from measurements of the cube area before testing. As a result, the stress-strain curve for cube 27-8 proceeds as expected up until a strain of approximately $\varepsilon_e = 0.0035$, where the strains start to diverge and the curve loses its validity (Fig. 5.4b). The stress-strain curves for the three different cubes appear to correlate well with each other (Fig. 5.5).

There was some statistical variation in the compression strengths of the different cubes tested (Fig. 5.6). The average compression force measured was 183.67 kN and the corresponding average compression strength was found to be 79.81 MPa. A full overview of the experimental results can be found in Table 5.1.

Table 5.1 – *Full results from the experimental concrete cube tests. The average force and stress for the whole table is given at the bottom.*

	Cube 1		*Cube 27*		*Cube 40*	
Part	F [kN]	f'_c [MPa]	F [kN]	f'_c [MPa]	F [kN]	f'_c [MPa]
1	205.11	83.35	203.70	82.47	197.56	84.75
2	181.42	82.09	183.09	78.84	171.60	77.68
3	213.22	83.44	208.73	82.35	165.45	73.07
4	193.98	81.85	202.32	87.47	137.62	58.21
5	180.60	76.35	191.52	81.45	201.21	85.22
6	171.29	77.38	191.92	85.60	188.82	84.22
7	173.08	77.86	175.89	79.29	159.66	73.21
8	164.90	70.61	183.73	78.81	161.67	68.11
	Average F [kN]			*Average* f'_c [MPa]		
	183.67			79.81		

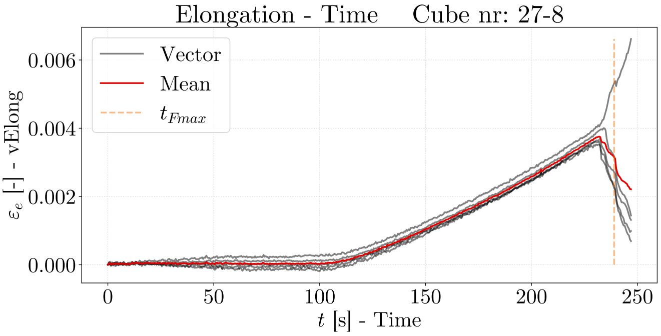

(a) *The strain measurements from the vectors over the course of time in grey. Orange dashed line is the time when the maximum force is measured.*

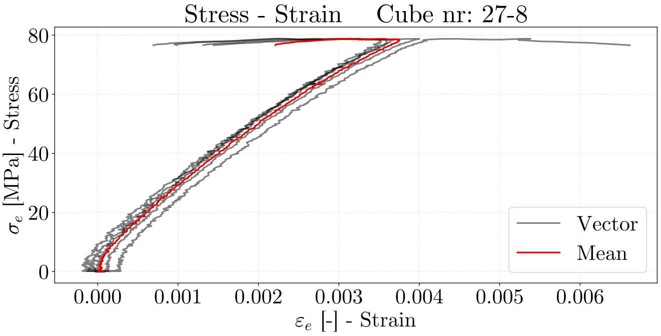

(b) *The stress-strain relationship for each of the individual vectors.*

Figure 5.4 – *Post-processed data from the DIC-analysis of cube 27-8. Red line is the mean of all the vectors. Data is only plotted up until the set cutoff value is exceeded.*

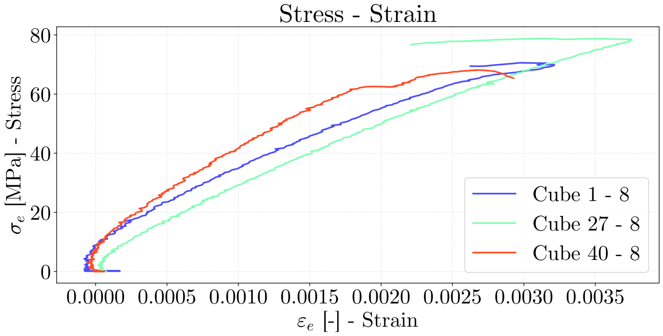

Figure 5.5 – *Mean stress-strain curves from all the cubes in the DIC-analysis.*

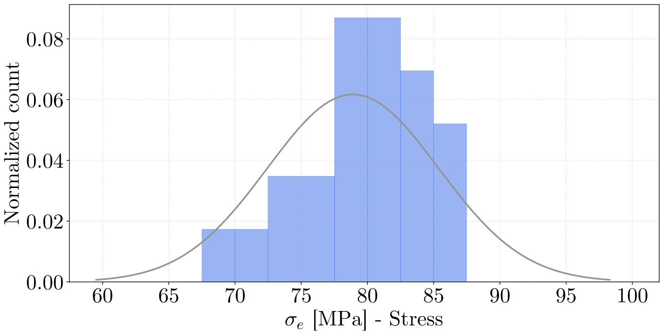

Figure 5.6 – *Histogram of the different compression strengths measured from all the tested cubes, together with a normal distribution. Bin width is* 2.5 MPa*.*

5.2 Pipe explosion tests

A series of experiments were conducted at the facilities of the Norwegian Defence Estates Agency at Østøya in Norway. The experiments consisted of explosion tests on concrete pipes. The aim of the experiments was mostly to get a qualitative impression of the behavior and failure modes, rather than do quantitative measurements of the concrete. Three different types of pipes were used in the tests. The smaller type of pipes were the plain cement concrete (PCC) *BASAL Mufferør ig*, while the larger type of pipes were the *BASAL Falsrør ig*, both reinforced and PCC. The pipes were provided by the concrete manufacturer BASAL [35][51]. Using mass produced commercial pipes ensures consistent geometry and material properties. The concrete is regularly sampled by the producer, and cube compression tests are performed throughout the curing process. Producer specifies a cube compressive strength f_c' of 38.2 MPa, 64.1 MPa and 83.3 MPa from samples taken 1 day, 7 days and 28 days into the curing process, respectively (App. A).

In the test series conducted during this thesis, a total of 18 tests were performed. Of the 18 tests, there was 6 tests of each of the three pipes exposed to different loadings. Earlier similar tests have also been done, of which the data was made accessible [9].

The explosive used was a spherical charge of C4 which was placed in the center of the pipe. Previously, placements such as interior and exterior contact charges have been explored, but experiments in this test series was only performed with centrically placed charges.

As mentioned, the experiments were mainly qualitative rather than quantitative, thus no efforts were made to measure deformation in the concrete pipes. This is due to the small deformations of concrete before tensile fracture and concretes inconsistent response, making it difficult and ineffective. However, for the purpose of validation and verification of the loading, and possible CFD-simulations, pressure was measured at different locations by Kistler 603B piezoelectric pressure sensors. There was six pressure sensors placed on the ground, distanced in direction along the longitudinal axis of the pipe, three on each side (Fig. 5.7). The sensors were placed in rising order, 210 mm, 610 mm and 1410 mm from the pipe end. In addition, two pressure sensors, sensor 7 and 8, were drilled into the pipe, location varying on the type of pipe (Fig. 5.8).

The experiments were filmed with a Phantom Miro LC310 (1280x800 @ 3268 fps), one camera filming from the front and one from the side.

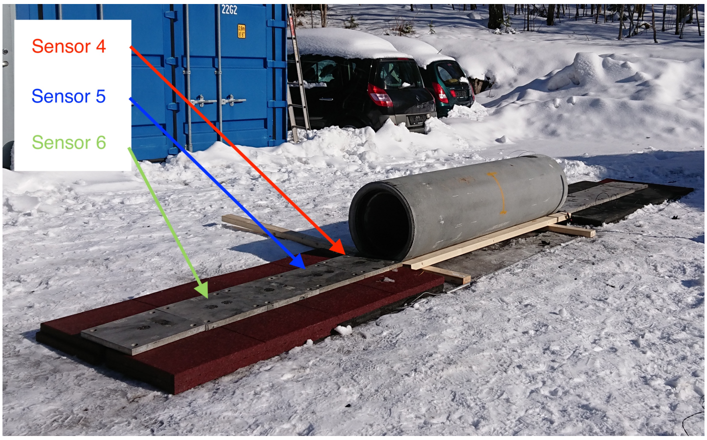

Figure 5.7 – *Pressure sensors placed outside the pipe. Sensors 1, 2 and 3 are placed in the same manner on the opposite end of the pipe.*

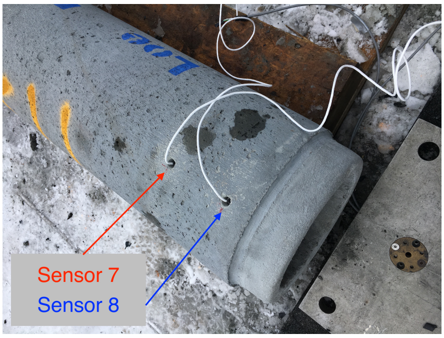

Figure 5.8 – *Pressure sensors 7 and 8 drilled into a BASAL Mufferør ig.*

5.2.1 Small pipes

The smaller type of pipes used were the *BASAL Mufferør ig*, 200 mm inner diameter and 1500 mm in length [51]. In the pipe, two holes were drilled to insert pressure sensors. The holes were drilled approximately 100 mm and 200 mm from the smaller opening of the pipe, making the internal distance between the sensors 100 mm (Fig. 5.8).

When performing tests with charges of different sizes, the subject of interest is the capacity of the pipe, i.e. at which point does it fail. Initially, two tests were performed with respectively 20 g and 10 g of C4. In the first test, after experience from earlier tests, it was quite certain the pipe would fail, and in the second test it was quite certain the pipe would not fail. This was intended to establish a lower and upper limit to the point of failure, subsequent tests would then be performed within the range from 10 g to 20 g. As expected, exposed to 20 g C4 the pipe was destroyed; whereas the second test, with 10 g C4, yielded no visible damage on the concrete pipe.

Using a charge of 12 g produced minor cracks, but no fragmentation. When increasing the charge from 12 g to 14 g there is a change in failure mode, the pipe goes from cracking to fragmenting (Table 5.3). These results are in compliance with previous findings. From the experimental tests performed in October 2017 [9], it was found that 13 g of C4 was required to produce through-thickness cracks (Table 5.4).

From high-speed footage one can see the difference between the two loading scenarios. For 12 g the pipe remains intact throughout the whole explosion. At a 14 g charge the pipe initially cracks at the middle, then the cracks propagate outwards creating large fragments which are blown outwards by the pressure inside the pipe. The majority of the damage occurs in the vicinity of the charge, the pipe ends remain fairly undamaged (Table 5.2).

Subsequently, charges of 16 g and 18 g were tested. The pipe fragmented again in both cases, but as the loading intensifies, the pipe fragments in smaller pieces. Afterburn could also be speculated to occur, observing high pressure air being blown out of the pipe long after the passing of the shock wave.

Table 5.2 – *Pipes subjected to* 12 g *and* 14 g *of C4 at frames 5, 50 and 200 after detonation. Shot with Phantom Miro LC310.*

Frame 5	12 g	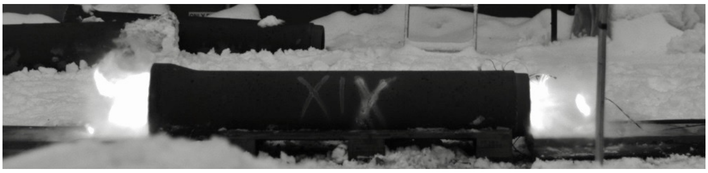
	14 g	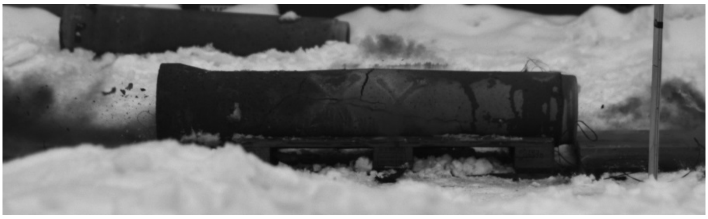
Frame 50	12 g	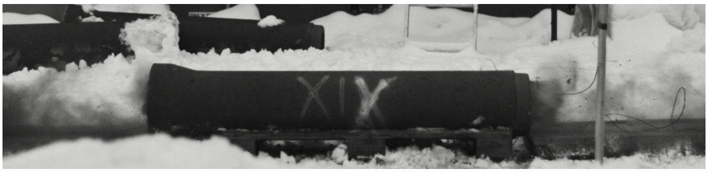
	14 g	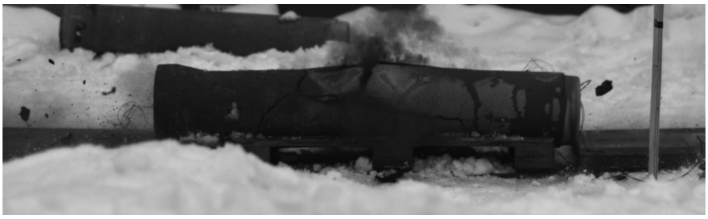
Frame 200	12 g	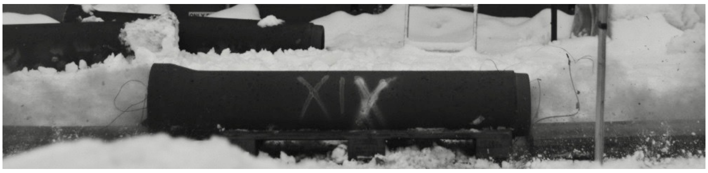
	14 g	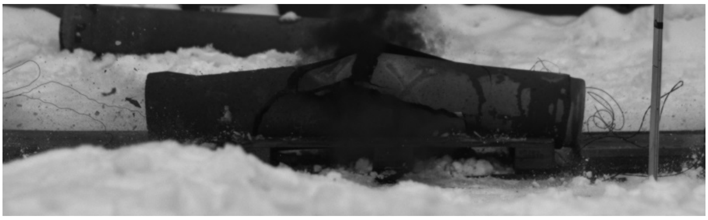

Table 5.3 – *Overview of tests performed on BASAL Mufferør ig.*

W [g]	Z $\left[\mathrm{m\,kg^{-1/3}}\right]$	*Test*	*ID*	*Failure mode*
10.0	0.464	2	XVIII	No failure
12.0	0.437	3	XIX	Cracking
14.0	0.415	4	XX	Fragmentation
16.0	0.397	5	XXI	Fragmentation
18.0	0.382	6	XXII	Fragmentation
20.0	0.368	1	XVII	Fragmentation

Table 5.4 – *Overview of experimental tests performed on BASAL Mufferør ig in October 2017 [9].*

W [g]	Z $\left[\mathrm{m\,kg^{-1/3}}\right]$	*ID*	*Failure mode*
10.0	0.464	III	No failure
12.5	0.431	IV	Cracking
13.0	0.425	XIV	Fragmentation
13.5	0.420	VI	Fragmentation
14.0	0.415	V	Fragmentation
15.0	0.405	II	Fragmentation
25.0	0.342	I	Fragmentation

5.2.2 Large Pipes - PCC

The larger type of pipes used were the *BASAL Falsrør ig*, 400 mm innner diameter and 2250 mm in length. The pipe was available as both reinforced and unreinforced (PCC), the latter will be discussed in this section. As with the smaller pipes, two holes were drilled in the pipe and pressure sensors were inserted. The holes were placed approximately 150 mm and 200 mm from the smaller opening of the pipe, giving an internal distance of 100 mm between the sensors.

The first test conducted with the PCC *BASAL Falsrør ig*, was with a charge of 150 g C4. The whole pipe was cracked into multiple pieces, not only at the middle, which were blown outwards by the blast. The muzzle ring at the narrowing end of the pipe also got blown off, probably by elastic stress waves concentrating in the narrowing, causing the concrete to fracture at this point.

The next two tests performed on the PCC *BASAL Falsrør ig*, were effectuated with charges of 100 g and 50 g C4 respectively. Using 100 g C4 resulted in the whole pipe shattering, but in considerably larger pieces than in the test with 150 g C4. A charge of 50 g resulted in no visible damage to the pipe (Table 5.6). Having established this, it was of interest to narrow down the interval where the point of failure would exist.

Subsequent tests was then performed with charges of 75 g and 65 g C4. When utilizing 75 g C4, the pipe got large longitudinal through-thickness cracks, creating large fragments. Rather than the pieces being blown outwards, as seen for higher loading scenarios, the pipe more or less collapsed. The concrete pieces appeared to be too large and heavy for the internal pressure in the pipe to scatter them. To check the consistency of the results, a second test with 75 g C4 was performed, and it produced very similar results in terms of failure mode. Reducing the charge size further down to 65 g yielded two large longitudinal through-thickness cracks, one on the top and one on bottom of the pipe, making the pipe split into two halves (Fig. 5.9). Full overview of the tests performed on PCC *BASAL Falsrør ig* can be found in Table 5.5. It is noted that the larger pipes fail at a larger scaled distance than the smaller pipes, implying that the relative capacity is smaller (Table 5.5). Also, the thickness to radius ratio is higher for the larger pipes which should imply them being stronger, contrary to what is observed.

Naturally, the pipes got increasingly more damaged as the loading intensified. From 50 g to 65 g it went from being visibly undamaged to having two longitudinal through-thickness cracks, splitting the pipe in two halves. It is a relatively short interval, in which the level of destruction goes from being uncritical to critical. A further increase in the charge size made the pipe shatter into smaller pieces. As the pieces got smaller, they were also scattered further out by the blast pressure. It was also observed some degree of afterburn on the high-speed footage. High pressure air was blown out of the pipe a significant time delay after the shock wave, and also contributing to the scatter of the concrete fragments.

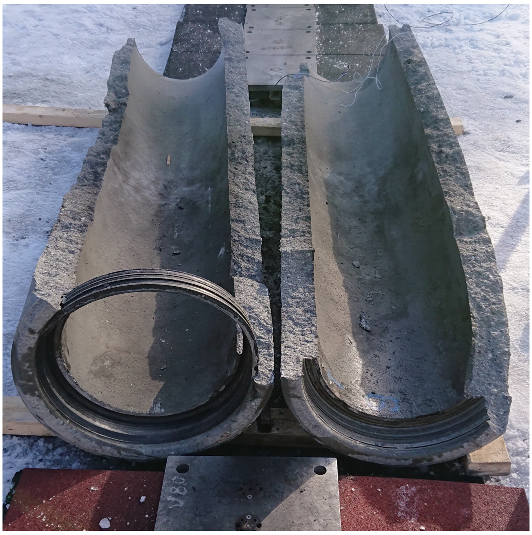

Figure 5.9 – *PCC BASAL Falsrør ig subjected to* 65 g *C4*

Table 5.5 – *Tests performed on plain cement concrete BASAL Falsrør ig.*

W [g]	*Z* $[\mathrm{m\,kg^{-1/3}}]$	*Test*	*ID*	*Failure mode*
50.0	0.543	12	VI	No failure
65.0	0.497	16	X	Cracking
75.0	0.474	13	VII	Fragmentation
75.0	0.474	14	VIII	Fragmentation
100.0	0.431	11	V	Fragmentation
150.0	0.376	7	I	Fragmentation

Table 5.6 – *Frame 200 after detonation, for four different pipes subjected to 50, 75, 100 and* 150 g *C4. Shot with Phantom Miro LC310.*

	Frame 200
50 g	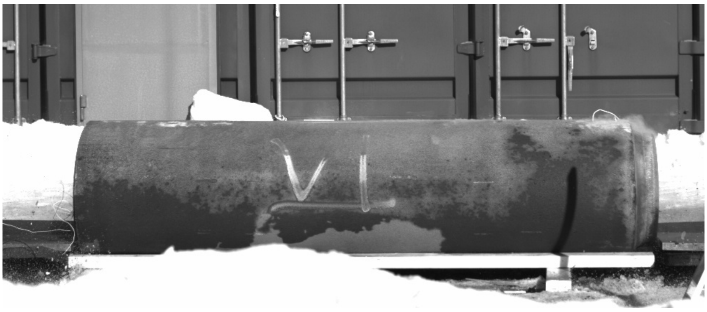
75 g	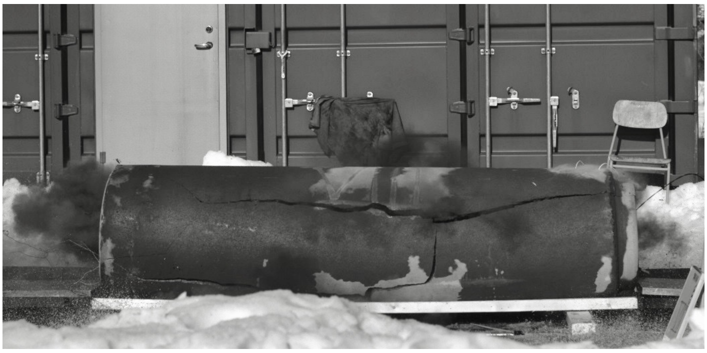
100 g	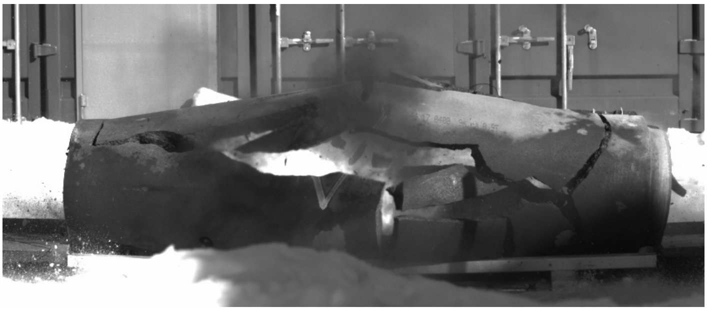
150 g	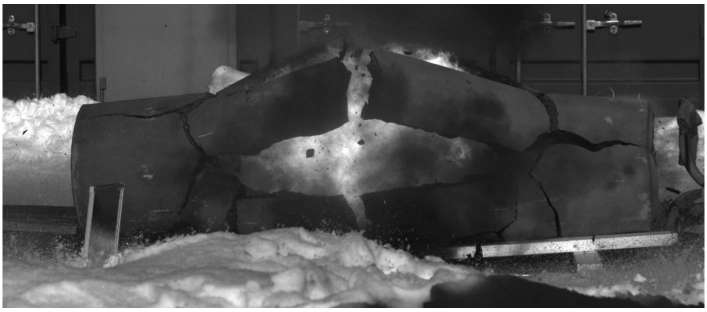

5.2.3 Large Pipes - Reinforced

The reinforced *BASAL Falsrør ig* were also tested. The reinforced pipes had the same dimensions as the PCC *BASAL Falsrør ig*. The pipe was reinforced both in the circumferential and longitudinal direction. A total of 12 rebar steel rods with a diameter of 8 mm was placed evenly around in the cross-section of the pipe, mid-placed across the thickness. On the outside of the rods, a rebar steel helix was wound, 6 mm in diameter, with approximately 100 mm of elevation per rotation. Pressure sensors were also inserted into two holes drilled in the pipe, at the same positions as for the PCC pipes.

The first test performed, employed a charge of 150 g C4. This is the only charge size which have been tested on both the reinforced and unreinforced concrete pipes. The behavior of reinforced and unreinforced concrete is thus directly comparable from these tests. Unlike the PCC pipe, the reinforced pipe did not get fragmented. Only minor cracks in the longitudinal direction were visible on the outside of the pipe, stretching from the middle and outwards. The cracks were evenly distanced in the circumferential direction, seemingly in correlation with the placement of longitudinal reinforcement. Some small cracks were also visible in the circumferential direction on the outside of the pipe, near the middle. The muzzle ring at the narrow end of the pipe got shattered and blown off, in similarity to what was seen at 150 g for the PCC pipe. Again, this is probably due to the concentration of elastic stress waves.

In the following tests on the reinforced *BASAL Falsrør ig*, the charge size was gradually increased from 150 g to 500 g (Table 5.7). Naturally, the level of destruction increased progressively with the loading intensity. At a charge of 200 g, there was still only minor cracks visible in the longitudinal and circumferential direction, although somewhat more profound and visible than for 150 g; the muzzle ring also broke off into several pieces. Increasing the charge to 300 g gave even larger cracks, and small pieces of concrete fell off in the intersection between the cracks in the longitudinal and circumferential direction at the middle (Fig. 5.10a). Some longitudinal cracks at the inside of the pipe were also visible (Fig. 5.10c). At the narrow end of the pipe, the muzzle ring got broken off and the opening got severely cracked.

A charge of 400 g C4 was then tested; cracks were even larger and more profound, and several pieces of concrete spalled off (Fig. 5.10b). There were continuous cracks from the middle of the pipe all the way to the narrow end of the pipe. The muzzle ring got blown off and shattered along with major parts of the opening. Another test with 400 g C4 was also performed to check the consistency of results. Both of the tests displayed similar behavior.

The largest charge that was tested was 500 g of C4. This resulted in fairly large damage to the pipe. In the vicinity of the charge, large pieces of concrete blew off and exposed the reinforcements. The pipe walls were breached, and large continuous longitudinal cracks spreading from the middle part of the pipe and outwards to the ends. The narrow end of the pipe got severely damaged, with large fractures and large pieces breaking off together with the muzzle ring.

Through the tests conducted, the pipes got increasingly more damaged as the loading intensified. At 150 g C4 there were only minor cracks visible, but at 500 g the pipe got severely damaged in proximity to the charge. It is noteworthy how much effect the reinforcement had on the strength of the pipe. The reinforced pipes are able to withstand almost half the scaled distance of the plain concrete pipes before the wall is breached (Table 5.7). The blast wave creates tensile stress in the pipe, mainly in the circumferential direction making the pipe crack up in the longitudinal direction. Concrete is weak in tensile stress, thus the added reinforcement aids in absorbing these tensile stresses and significantly strengthen the concrete under the applied blast load. This not only makes the reinforced pipes stronger, but it also makes the destruction process under increased loading much more gradual, compared to the unreinforced pipes. The unreinforced went from being visibly undamaged at 50 g C4, to having large longitudinal cracks at 65 g C4, an increase in loading size of 30%. For the reinforced pipes, from being nearly undamaged at 150 g, it was necessary with an increase in charge size up to 100-200% before any critical damage was visible.

Table 5.7 – *Tests performed on reinforced BASAL Falsrør ig.*

W [g]	*Z* $\left[\mathrm{m\,kg^{-1/3}}\right]$	*Test*	*ID*	*Failure mode*
150.0	0.376	8	II	Cracking
200.0	0.342	9	III	Cracking
300.0	0.299	10	IV	Cracking and spalling/scabbing
400.0	0.271	15	IX	Cracking and spalling/scabbing
400.0	0.271	18	XII	Cracking and spalling/scabbing
500.0	0.252	17	XI	Cracking and fragmentation

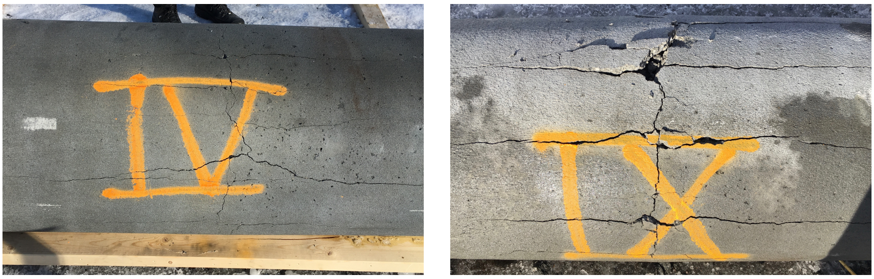

(a) *Reinforced BASAL Falsrør ig subjected to* 300 g *C4. Exterior cracks visible in longitudinal and circumferential direction.*

(b) *Reinforced BASAL Falsrør ig subjected to* 400 g *C4. Exterior cracks visible in longitudinal and circumferential direction.*

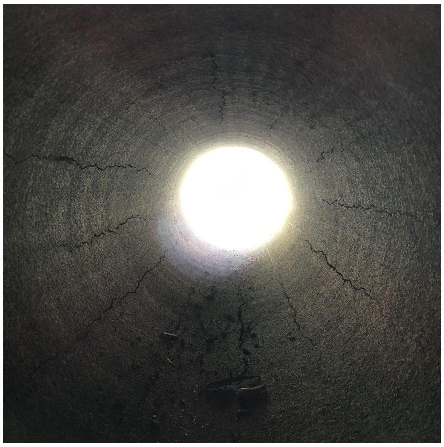

(c) *Reinforced BASAL Falsrør ig subjected to* 300 g *C4. Interior cracks visible in longitudinal direction.*

Figure 5.10 – *Exterior and interior views of pipes subjected to* 300 g *and* 400 g *C4.*

Table 5.8 – *Frame 200 after detonation, for three different pipes subjected to* 150 g, 300 g *and* 500 g *C4. Shot with Phantom Miro LC310.*

	Frame 200
150 g	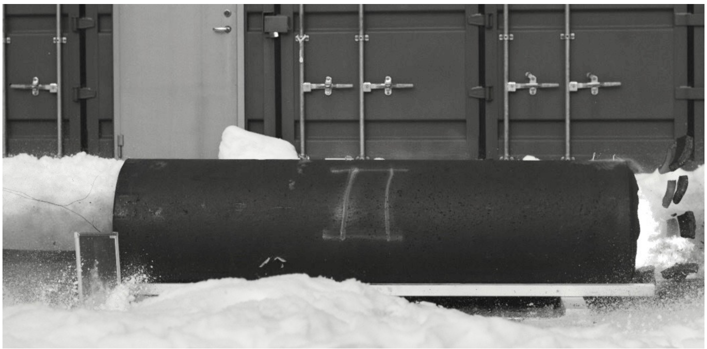
300 g	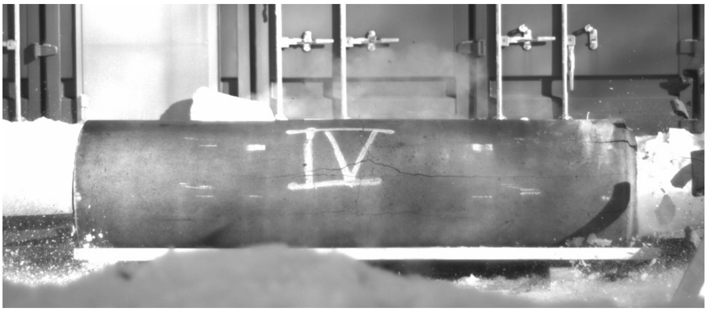
500 g	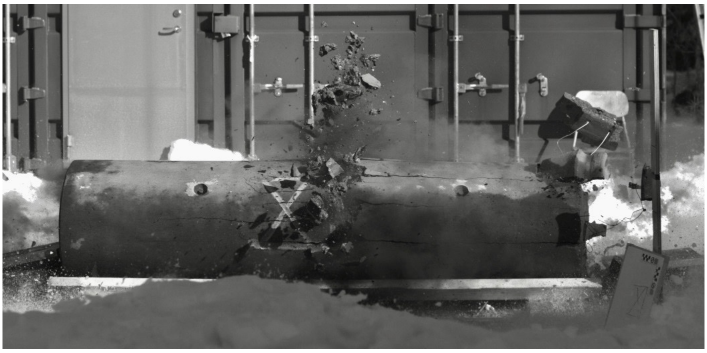

5.3 Pressure measurements

In the theory chapter, it was shown through a scaling law that there is a linear relationship between the size of the charge and the maximum pressure at a location. It was therefore of interest to verify this theory. In general, there was a lot of inconsistent pressure recordings, though pressure sensors 3, 4 and 5, in addition to 8, gave steady results, apart from a few exceptions. The data from these exceptions were omitted from the analysis. By plotting the maximum pressure measured at the different sensors against the charge size, a clear linear trend is visible (Fig. 5.11a) (Fig. 5.11b). The slope of the curve also increases as the distance to the pipe decreases; sensor 4 being closest to the pipe and 3 being farthest away in Figure 5.11a. Sensor 8 is closest of them all, and it was necessary to plot in a different window because of the large differences in slope and magnitude.

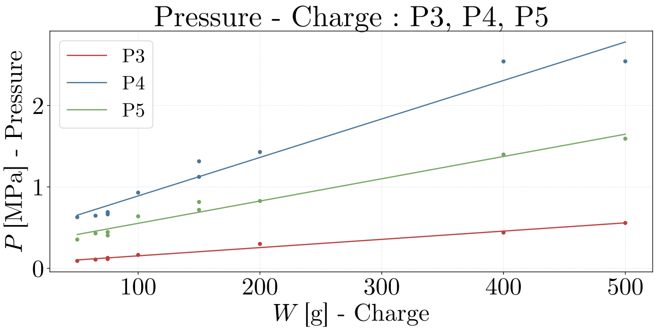

(a) *Maximum pressure measured at sensor 3, 4 and 5 for different sized charges.*

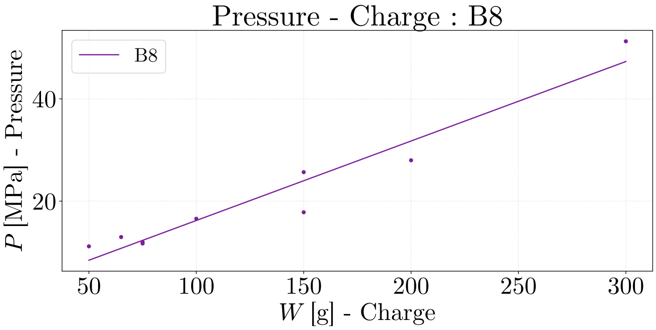

(b) *Maximum pressure measured at sensor 8 for different sized charges.*

Figure 5.11 – *Linear relations for increasing charge and maximum pressure.*

Chapter 6

Numerical Study - Concrete Cubes

The concrete cubes were modeled using the Concrete Damaged Plasticity (CDP) model in ABAQUS. The CDP model requires several parameters with extensive calibration for each of them. Calibration of the CDP model is not within the scope of this study. The most known work on this is done by Jankowiak and Lodygowski [52], and the parameters they have found is employed in the simulations done in this thesis. Rate dependency is not readily available in the CDP model in ABAQUS, it must be calibrated using tabulated data for tensile stiffening or compressive hardening [27]. This was not a part of this study either, so the concrete will be modeled as rate independent. For simplicity the configuration of the CDP model proposed by Jankowiak and Lodygowski will be referred to as the J-L configuration.

The aim was to investigate the behavior of the CDP model under variation of different material parameters and erosion, with the compression cube tests working as a reference. By this a cube with dimensions 50 mm × 50 mm × 50 mm was assigned properties by the J-L configuration of the CDP model. Furthermore, two analytical plates were set up, one which the cube stands on, the other plate moves down with a constant velocity and compresses the cube. The moving plate is given a velocity resulting in a displacement of 1.5 mm from the top of the plate, which is approximately the same as the maximum displacement in the experimental tests.

The ABAQUS Scripting Interface and Python was extensively used throughout this thesis, both in pre- and post-processing. An elaborate system of scripts were created as the foundation for the data analyses performed. A short presentation of this system will be given in the following section.

6.1 Workflow

One of the main advantages of ABAQUS, from a user's perspective, is the scripting interface it provides. The ABAQUS scripting interface is an extension of the Python object-oriented programming language [53] [54]. The ABAQUS Scripting Interface can be used to create and modify components of an ABAQUS model, read and write to an ABAQUS database and several other things. In this thesis, it has been used as much as possible together with regular Python programming, to automate processes and reduce unnecessary repetitive tasks. Throughout the thesis an elaborate system of scripts have been made, to function in all the steps of the process from making a model to plotting the results. An overview of the workflow is presented in Fig. 6.1.

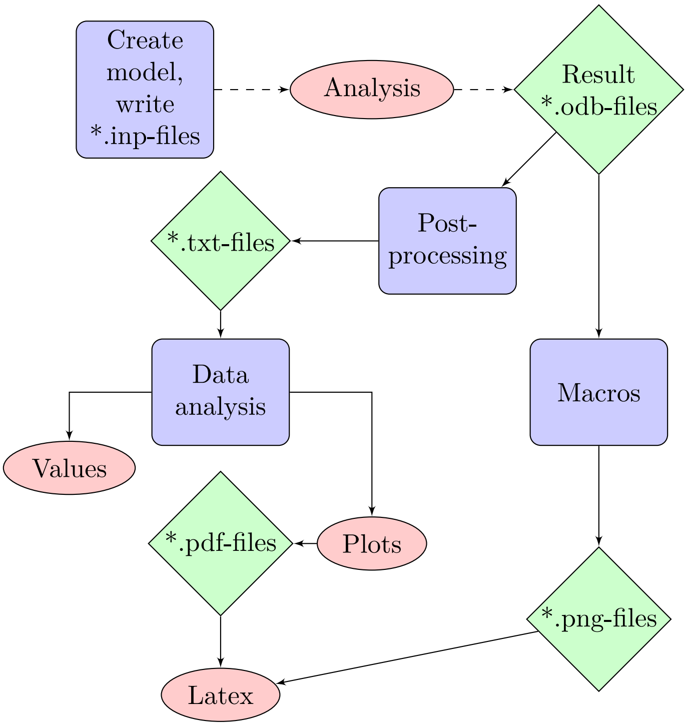
Create model, write *.inp-files
Analysis
Result *.odb-files
Post-processing
*.txt-files
Data analysis
Macros
Values
*.pdf-files
Plots
*.png-files
Latex

Figure 6.1 – *Blue boxes represent scripted tasks. Green diamonds represent file storage. Red ellipses represent other tasks and processes. Solid lines, files are pushed and pulled automatically by scripts. Dashed lines, files are moved manually.*

Different scripts were made to model the cubes, plain concrete pipes and reinforced pipes. These scripts created the **.inp*-files necessary to submit the analyses. In the parameter studies, the names of the **.inp*-files were automatically generated depending on the altered parameter, to differentiate the files easily. For instance, a cube with mesh size 5 mm would contain *'_MeshSize_5_0'* in the filename. Analyses were performed on the CPU cluster *Snurre*, thus files had to be uploaded and downloaded manually. Thereafter another script extracted relevant data from the result **.odb*-files and wrote them into **.txt*-files, for faster file reading when plotting. Other scripts were then able to access these **.txt*-files and could store them into objects. Working with objects made it easier to handle and classify the data. From the objects the data could be plotted and values of interest could be printed. By reading the filename, the objects could be differentiated and automatic labeling of plots was accomplished. The most relevant plots were saved in a folder system which the Latex compiler accessed, thus ensuring plots automatically stayed updated. For the extraction of figures from the **.odb*-files, macros were used.

6.2 Parameter study

It is of interest to investigate the impact different parameters has on the results of the simulation. The first parameter which was investigated was a scale factor, in which the tabulated compression hardening and tensile stiffening values were scaled by different factors (Table C.2)(Table C.3). The scale factor was then interpolated to match the compression strength of the experimental cubes. Other parameters that were studied was the E-modulus, the time period of the simulation, mesh size, friction coefficient, erosion criterion and lastly another configuration of the material model.

The basis model for the parameter study was modeled with a mesh size (MS) of 1 mm, a friction coefficient (F) of 1 and a time period (TP) of 0.010. No erosion was activated for the base model. When scale factor is not altered, a value of $\lambda = 1.43$ is used to give the same compression force as in the experiments.

6.2.1 Scale factor

The purpose of the scale factor is to scale the tabulated values for compressive hardening as well as the tensile stiffening by a factor λ, to alter the compressive and tensile strength of the concrete. Other material parameters are left unchanged. Scale factor $\lambda = 1$ corresponds to the initial parameters.

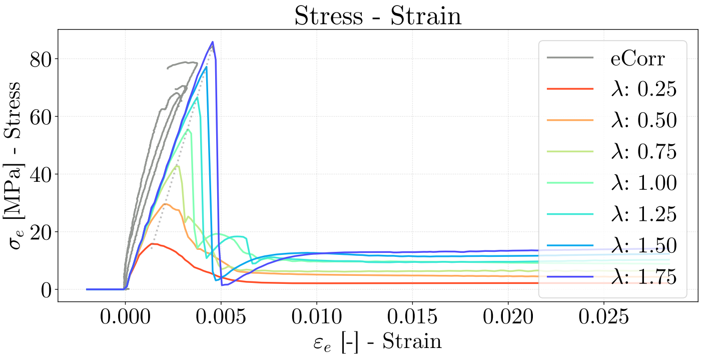

Figure 6.2 – *Stress-strain curves for the different scale factors. Dotted grey line emphasizes the trend of peak stress for increasing scale factor.*

Scale factors evenly distributed within the interval $\lambda \in [0.25, 1.75]$ was chosen. The trend when increasing the scale factor is quite obvious. For higher scale factor the concrete is given a higher compressive strength (Fig. 6.5), and a higher resultant force is measured (Fig. 6.3a).

When looking at the engineering stress-strain curve for the different scale factors it is seen that the point of peak stress occurs at higher strains as the scale factor increases (Fig. 6.2). The slope of the curve correlates quite well with the stress-strain curves from the DIC. Though, the stress-strain curve for the higher scale factors appear somewhat tilted. This is due to the E-modulus being kept constant at $E = 19\,700.0\,\mathrm{MPa}$ regardless of the scale factor. It seems to put constraints on the curve, and to reach a higher compressive stress the curve peak must move to higher strains. Additionally, this causes a somewhat unnatural post yield behavior for the higher scale factors, with a rapid post peak drop before almost dropping to zero and then rising again; i.e. a significantly higher degree of strain softening. For the lower scale factors the stress-strain curve resembles more the characteristic stress-strain curve that is known for concrete. It is peculiar to observe that for a scale factor of $\lambda = 1$ the stress-strain curve shows some fluctuations, considering that this is the original configuration provided by Jankowiak et al [52]. It could be caused by the time scaling of the model or perhaps some contact issues. However, the purpose of these simulations and the parameter study is mainly to investigate the effect of varying different parameters and possibly identify the cause for the aforementioned instabilities. Observing some small instabilities here in the simulations is therefore not a large concern.

From experimental tests the force applied to the concrete cubes was mea-

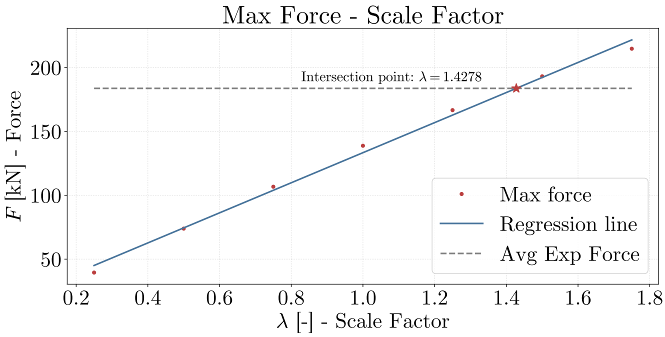

(a) *Maximum force from simulation against scale factor of simulation.*

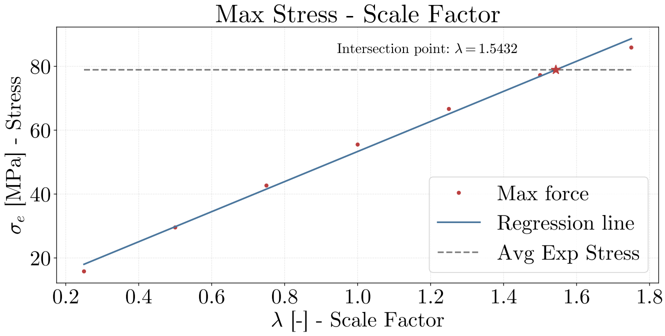

(b) *Maximum stress from simulation against scale factor of simulation.*

Figure 6.3 – *Interpolation to find the different scale factors giving (a) same resultant force and (b) same compressive strength.*

sured and the engineering stress was calculated. The same procedure was used in the simulations to find the compressive strength of the cube. The maximum compressive forces obtained from the different simulations were compared to the average maximum compression force from experiments. In the same manner the maximum engineering stresses from simulations were compared to the average experimental compression strength. A linear regression model was used to find the trend between increasing scale factor and increasing force and stress. Then the scale factor was interpolated so the values from the simulation matches the values from the experiments (Fig. 6.3).

When scaled to give the same maximum force, the scale factor was found to be approximately $\lambda = 1.43$. This corresponds to a measured engineering stress, i.e. the resultant force divided by the area of the cube, of 74.01 MPa. This is because the simulated model was created with the idealized cross-sectional area of 2500 mm^2, while the nominal experimental cross-sectional area was 2327 mm^2.

A scale factor of $\lambda = 1.54$ gives the same compression strength, $f'_c = 78.90$ MPa. Though the theoretical compression strength, i.e. the maximum scaled compression hardening value, was found to be 77.17 MPa. In general it was seen a slightly higher measured compression strength than theoretical compression strength (Table 6.1).

Table 6.1 – *Theoretical and measured compression strength for different scale factors.*

λ	0.25	0.5	0.75	1.0	1.25	1.5	1.75
f'_c, theoretical	12.50	25.00	37.51	50.01	62.51	75.01	87.51
f'_c, measured	15.80	29.56	42.67	55.50	66.65	77.24	85.87

6.2.2 Modulus of elasticity

For concrete, the modulus of elasticity E_c is highly dependent on compressive strength [36]. The shape of the stress-strain curve should also be similar for concrete of low, normal and high strength, with the peak close to the strain value $\varepsilon_e = 0.002$. The E-modulus is connected to the maximum compressive strength of concrete through an empirical relation

$$E_c = \rho_c^{1.50} \times 0.043\sqrt{f'_c} \quad \text{[MPa]} \tag{6.1}$$

where ρ_c is the density of the concrete, and f_c' is the compressive strength [36][55]. This empirical relation was used to adjust the E-modulus, as the compression strength, and tensile strength, was scaled.

The effect of the adjustment, is quite clear. The tilt that was seen for the higher scale factors are gone, and the peaks are much more aligned vertically around $\varepsilon_e = 0.002$. This is further emphasized by the grey dotted line (Fig. 6.4).

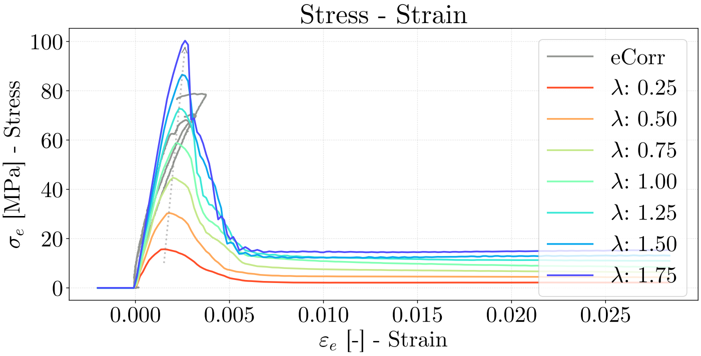

Figure 6.4 – *Stress-strain curves for the different scale factors. Dotted grey line emphasizes the trend of peak stress for increasing scale factor.*

The relation between scale factor and maximum compression force was found. Using the empirical formula (Eq. 6.1), resulted in a generally higher E-modulus for the concrete and by that a stiffer behavior. To then achieve the same displacement of 1.5 mm much higher forces were required and higher stresses obtained. By interpolation, the scale factor corresponding to the maximum average experimental force was found to be $\lambda = 1.26$. This gives a theoretical compression strength of $f_c' = 63.34\,\mathrm{MPa}$ from the tabulated values given to the CDP model.

To achieve the same compression strength as in the experiments, a scale factor of $\lambda = 1.36$ was necessary (Fig 6.5). This corresponds to a theoretical compression strength of $f_c' = 68.16\,\mathrm{MPa}$. It is interesting to observe how there is a much larger difference between the theoretical compression strength and the maximum measured engineering stress when the adjustment of the E-modulus is included (Table 6.2). It appears that it is not necessarily the tabulated compression hardening values alone that dictate the maximum compression strength in the CDP model.

The shape of the stress-strain curve resembles more what one would expect from the stress-strain curve of concrete. The slopes of the curves with $\lambda =$

Table 6.2 – *Theoretical and measured compression strength for different scale factors with adjusted E-modulus.*

λ	0.25	0.5	0.75	1.0	1.25	1.5	1.75
f'_c, theoretical	12.50	25.00	37.51	50.01	62.51	75.01	87.51
f'_c, measured	15.68	30.35	44.73	58.82	72.74	86.52	100.33

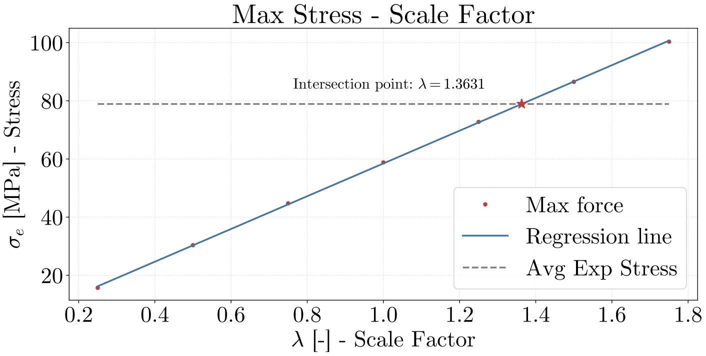

Figure 6.5 – *Maximum stress from simulation against scale factor of simulation. Interpolation to find the scale factor corresponding to the same compression strength as in the experiments.*

1.00 and $\lambda = 1.25$ also correlate well with the stress-strain curves from the DIC. Considering that the resulting scale factor was found to be $\lambda = 1.36$, this result seems to be in fairly good agreement with experimental tests. There is the near-linear behavior in the beginning, before the concrete yields and the slope of the curve starts to reduce around 75 % of the maximum compression strength f'_c. After the peak, the curve decreases and flattens out. In some of the curves, some oscillations are present for the higher scale factor. The critical time step is reduced due to the increased E-modulus while the time period of the simulation is being kept constant. Thus for the simulations with the highest E-modulus, it appears that the time scaling should be altered if more accurate results were to be achieved.

6.2.3 Time period

Since the experimental compression tests of the cubes were quasi-static, it is common to use time scaling to prevent unnecessarily long and tedious

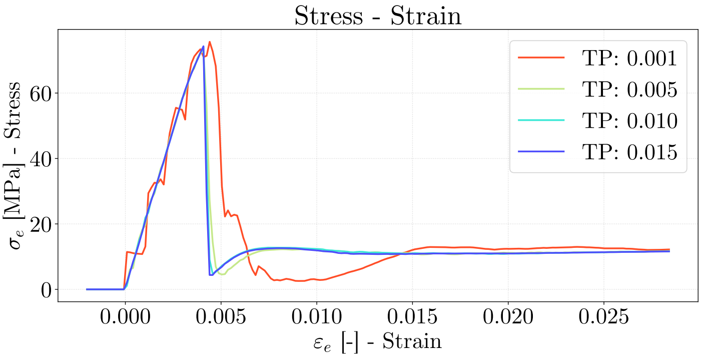

Figure 6.6 – *Stress-strain curve for varying time period.*

simulations. Another option is mass scaling, but by the author's convention, time scaling was chosen. This method is commonly used, but it is important to take care not to scale the time excessively. To ensure this, it is important to ensure that the kinetic energy stays low compared to the internal energy.

It is observed that as the time period of the simulation is scaled down, the stress-strain curve becomes increasingly unsteady and fluctuating. Altering the time period from $TP = 0.015$ to $TP = 0.005$ however, does not yield much difference. It is first when the time period is set to $TP = 0.001$ that large fluctuations become observable.

When looking at the ratio of kinetic to internal energy, throughout the simulation time, it is seen that there is a lot of kinetic energy for $TP = 0.001$ (Fig. 6.7). In the beginning it is high, due to internal energy being low, but as the simulation proceeds it continues to stay relatively high compared to the other simulations. Yet it is not critically high. It is normally recommended that it should be less than 5 %, whereas for $TP = 0.001$ it has a maximum of $\sim 8\%$, though only for a short period. For the other simulations a small peak is observed near $\tau = 0.25$, though the ratio of kinetic to internal energy stays between 2-3 % at its maximum.

In general, the total energy, which in ABAQUS is the same as the energy balance, of a simulation should converge towards a constant value, ideally zero. Especially for a static or quasi-static analysis, the total energy should be zero or close to zero, to ensure that no additional kinetic energy has been created in the simulation [27]. The total energy is low and close to zero for all the different time periods, though the highest total energy occurring for a time period of $TP = 0.001$.

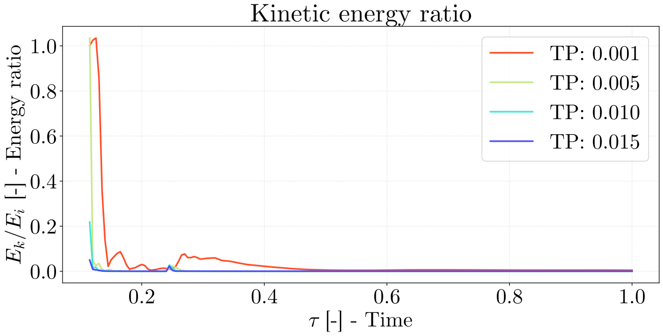

Figure 6.7 – *Development of the ratio of kinetic energy to internal energy against non-dimensional time for different time periods.*

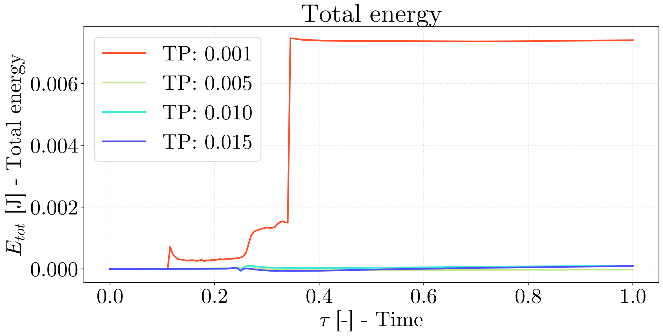

Figure 6.8 – *Development of the ratio of kinetic energy to internal energy against non-dimensional time for different time periods.*

Although the energy balances were acceptable for all the simulations, it was seen from the stress-strain curve that large fluctuations occurred when the time period was scaled down to $TP = 0.001$. From a time period of $TP = 0.005$ and higher however, the stress strain curve and the energy balances were very similar.

6.2.4 Mesh size

An important parameter to investigate is the mesh size. A fine mesh is desirable because it enhances the accuracy of the solution, but it also greatly increases computational costs. It is therefore interesting to find a mesh size which provides the required accuracy, while still keeping computational costs

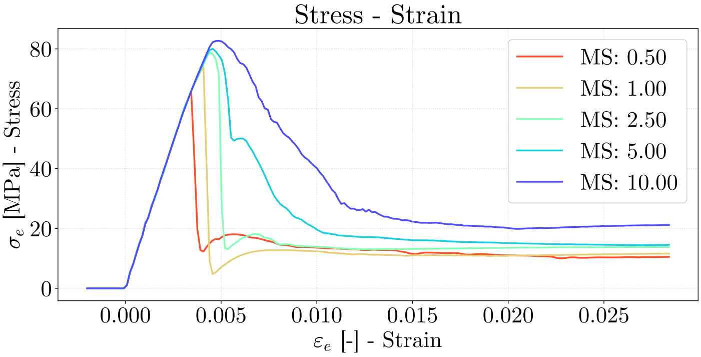

Figure 6.9 – *Stress-strain curve for varying mesh size.*

low.

Increasing the mesh size resulted in a generally higher peak stress. Linear C3D8R elements are used, so fewer elements does give a more rigid behavior. Furthermore, for a mesh size higher than $MS = 2.5\,\text{mm}$ the rapid drop after peak stress becomes more flattened out and diffuse. For mesh sizes less than and including $MS = 2.5\,\text{mm}$, there is an abrupt post peak softening phase, before the curve rises slightly again and flattens out. The largest dip happens for $MS = 1.0\,\text{mm}$.

The material model appears to be significantly mesh dependent, with a more severe strain-softening as the mesh size decreases. It is seen that as the mesh size increases, the strains tend to be more smeared out and localize less, resulting in generally smaller strain values (Fig. 6.10).

More kinetic energy occurred when the mesh size was reduced, though the values were generally low, also for the total energy. Thus, the energy balances were in order.

6.2.5 Friction

The interactions between the cube and the plates were modeled with a tangential friction coefficient. From previous simulations it has been discussed that some irregularities in the simulations could be caused by contact problems. Further study of the effect of varying friction coefficient could therefore provide more insight. For comparison, a model with a tie constraint between the bottom of the cube and the bottom plate was also added to the study, this would correspond to a infinite friction coefficient.

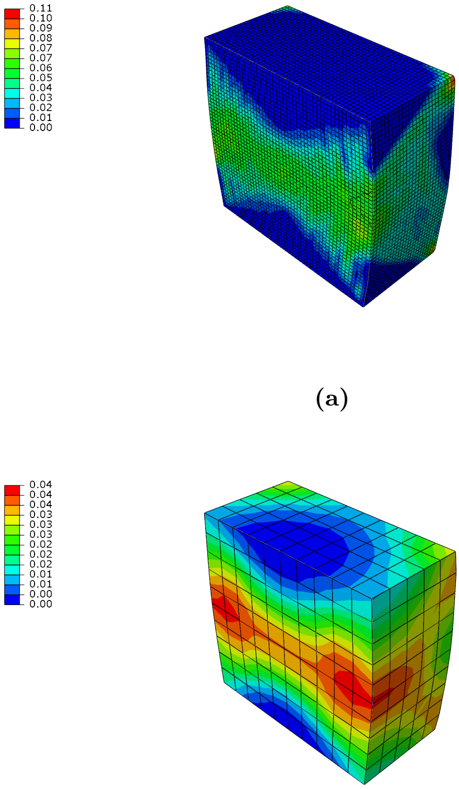

(a)

(b)

Figure 6.10 – *Equivalent plastic strain at maximum displacement. Viewcut through the middle for a cube with mesh size (a)* 1 mm *and (b)* 5 mm*.*

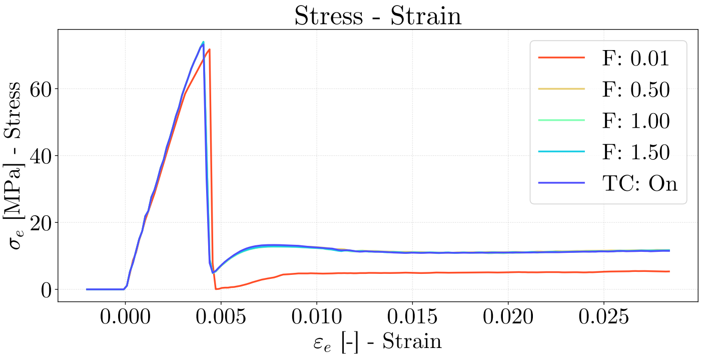

Figure 6.11 – *Stress-strain curve for varying friction coefficient and tie constraint.*

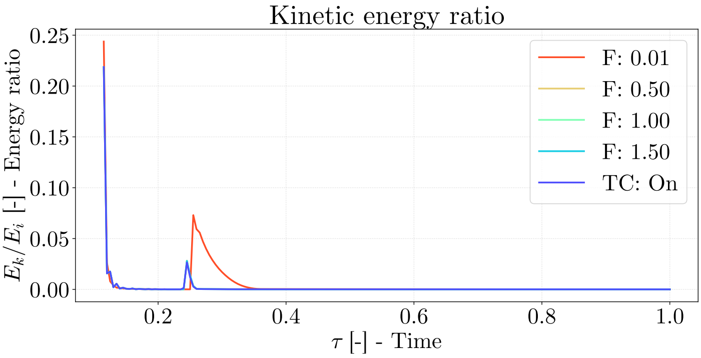

Figure 6.12 – *Ratio of kinetic to internal energy throughout the simulation for varying friction coefficients and tie constraint.*

For a friction coefficient of $F = 0.01$, which corresponds to a near frictionless description, the stress-strain curve shows a larger dip after peak stress, almost down to zero. For the higher friction coefficients and the tie constraint there is hardly any differences in the stress-strain curve.

The kinetic energy ratio is reduced when friction is introduced (Fig. 6.12). Between $\tau = 2$ and $\tau = 3$, there are some peaks in the kinetic energy ratio. For $F = 0.01$ the maximum ratio of kinetic to internal energy is approximately 7 %, seen from this peak. For the higher friction coefficients and the tie constraint, the ratio stays below 5 % with a peak of around 3%. Anyhow, the kinetic energy ratio is never particularly high for either of the simulations and it tends towards zero as the simulation proceeds. The results does suggest that introducing friction to the model is a good idea.

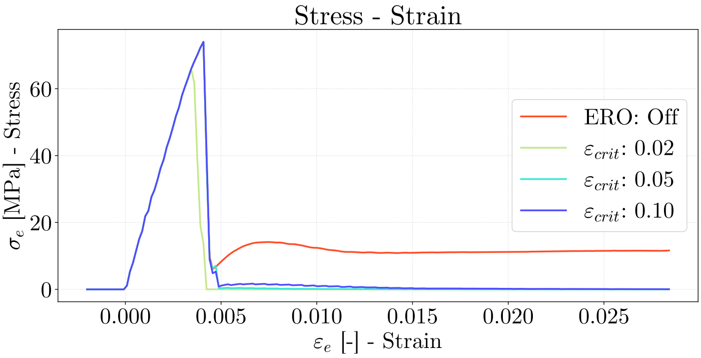

Figure 6.13 – *Stress-strain curve for varying erosion criterion and no erosion.*

Though the sensitivity to the magnitude of the friction coefficient is very small, so a particular value seems unimportant as long as it is not close to zero or above 0.5 to be on the safe side. In short, there appears to be no contact problems in this model.

6.2.6 Erosion

In the real physical world, the concrete cracks up and falls apart. Previous simulations has not captured this phenomenon, the concrete has deformed, but has not fractured. In ABAQUS it is possible to introduce element erosion by the use of a subroutine. The subroutine is given an erosion criterion related to the strain in a element. If the strain exceeds the erosion criterion, the element is removed, or eroded. The values for the erosion criterion used in the following simulations are $\varepsilon_{crit} \in [0.02, 0.05, 0.10]$. Hillestad and Pettersen used an erosion criterion of $\varepsilon_{crit} = 0.01$, but found that this gave immoderate erosion [6].

For an erosion criterion of $\varepsilon_{crit} = 0.02$, the stress-strain curve does not reach the same peak as when erosion is not activated. The concrete fails before reaching maximum stress, since the stress rapidly drops to zero during the hardening phase. When the erosion criterion is increased further, a higher maximum stress is reached, the same as when erosion is not activated. Although, with erosion activated the stress drops to zero after the peak; without erosion the stress eventually stabilizes to a constant value. With erosion, an excessive amount of elements are eroded such that stresses are no longer able to propagate through the cube. This is not in compliance with the physical experiments. In the experiments, it was seen that after the maximum force occurred, the displacement continued while the force saw a rapid drop. Though eventually the force curve started to flatten out and did not drop directly to zero, like was seen from the simulations.

Exaggerated erosion was seen, even as the erosion criterion was increased to $\varepsilon_{crit} = 0.10$ (Fig. 6.14). Thus, the strength of the cubes were underestimated. For the lowest erosion criterion $\varepsilon_{crit} = 0.02$, there was some kinetic energy being created in the model, due to some actual movement of detached elements. The kinetic energy is still very low, and other energy balances was in order.

6.2.7 Material calibration

Another configuration of the CDP model was proposed by Labibzadeh et al. [56] for a concrete with compression strength of $f_c' = 37.5\,\text{MPa}$. They did a series of experimental and numerical tests and used error minimizing functions to tweak the material parameters. Here, the values they have found has merely been adopted and scaled to see how the behavior changes and differs from the configuration proposed by Jankowiak et al. [52]. Having also seen that the J-L configuration has not yielded results completely as expected, giving a stress-strain curve with a very sharp peak rather than the characteristic smooth *bell-shape*, it is of interest to investigate other configurations of the CDP model; keeping in mind subsequent simulations to be performed. For simplicity, the configuration by Labibzadeh et al. will be referred to as the Lab configuration.

The first impression of the stress-strain plot is that the curves resemble more of what is expected from a concrete stress-strain curve (Fig. 6.15). Results from the DIC tests agree well with the stress-strain curves, with a parallel gradient. The curves experience a smooth rise and gradual descent before the they flatten out. This trend is apparent for all the curves, perhaps expect for $\lambda = 1.75$, where some fluctuations appear after maximum stress.

The reason for the fluctuations is difficult to identify; the kinetic energy ratio shows some oscillations, though the kinetic energy is never high compared to the internal energy. A possibility for the fluctuations could then be the time scaling of the problem. Another possible reason is the tabulated values for compression hardening and tensile stiffening are being excessively scaled while the other material parameters, like the E-modulus, are being kept constant. Thus creating a constraint on the curve, as was seen when scaling the J-L configuration. The stress-strain curves with the J-L configuration saw improvements when adjusting the E-modulus according to the compression strength, the same adjustment could better the Lab configuration as well.

To achieve the same compression force as for the experimental tests, a scale

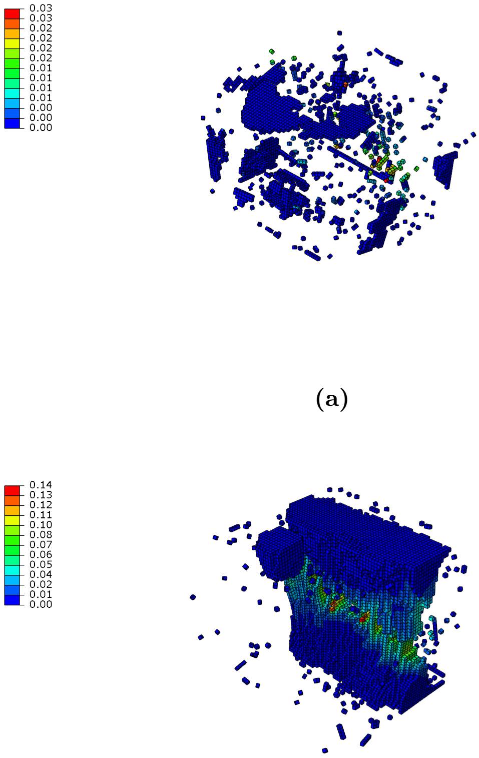
0.03
0.03
0.02
0.02
0.02
0.02
0.01
0.01
0.01
0.01
0.00
0.00
0.00
0.14
0.13
0.12
0.11
0.10
0.08
0.07
0.06
0.05
0.04
0.02
0.01
0.00

(a)

(b)

Figure 6.14 – *Equivalent plastic strain at maximum displacement. Cubes with (a)* $\varepsilon_{crit} = 0.02$ *and (b)* $\varepsilon_{crit} = 0.10$.

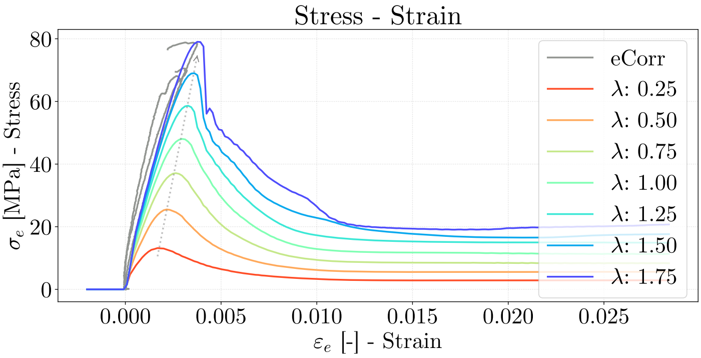

Figure 6.15 – *Stress-strain curves for the different scale factors. Dotted grey line emphasizes the trend of peak stress for increasing scale factor*

factor of $\lambda = 1.60$ is necessary. This corresponds to a theoretical compression strength 60.01 MPa. The experimental compression strength is obtained by a scale factor of $\lambda = 1.72$. The corresponding theoretical compression strength is 64.66 MPa. For this configuration of the CDP model, it is seen that the measured engineering stress is in general higher than the theoretical compression strength (Table 6.3), even without the adjustment of E-modulus.

It is seen that strains concentrate more with the configuration proposed by Labibzadeh et al. [56], compared to the J-L configuration (Fig. 6.16). Also, when the E-modulus is adjusted in the J-L configuration, the strains seem to localize more. Strains are highest in the corners of the cubes and tend to be concentrated in the middle, stretching diagonally from the center and out to the corners. A large decrease in compression strength was also observed to give more concentrated strains.

Table 6.3 – *Theoretical and measured compression strength for different scale factors with the Lab configuration of the CDP model.*

λ	0.25	0.5	0.75	1.0	1.25	1.5	1.75
f_c', theoretical	9.37	18.75	28.12	37.50	46.87	56.25	65.62
f_c', measured	13.18	25.51	37.10	48.03	58.64	69.02	79.04

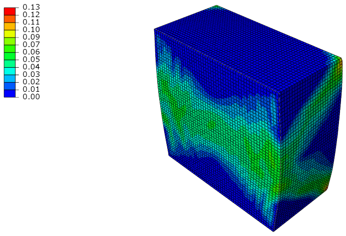
0.13
0.12
0.11
0.10
0.09
0.07
0.06
0.05
0.04
0.03
0.02
0.01
0.00

(a) $\lambda = 1.50$, $f_c' = 77.24\,\text{MPa}$, $E_c = 19\,700.0\,\text{MPa}$

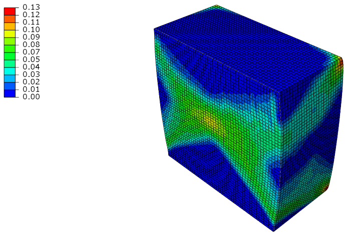
0.13
0.12
0.11
0.10
0.09
0.08
0.07
0.05
0.04
0.03
0.02
0.01
0.00

(b) $\lambda = 1.25$, $f_c' = 72.74\,\text{MPa}$, $E_c = 40\,764.3\,\text{MPa}$

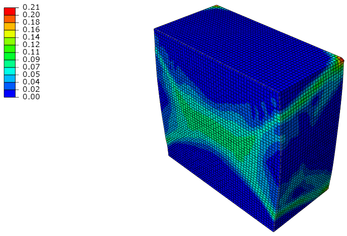
0.21
0.20
0.18
0.16
0.14
0.12
0.11
0.09
0.07
0.05
0.04
0.02
0.00

(c) $\lambda = 1.75$, $f_c' = 79.04\,\text{MPa}$, $E_c = 33\,000.0\,\text{MPa}$

Figure 6.16 – *Equivalent plastic strain at maximum displacement. Cubes with configuration by (a) Jankowiak and Lodygowski, (b) Jankowiak and Lodygowski wit adjusted E-modulus and (c) Labibzadeh et al.*

Chapter 7

Numerical Study - Concrete Pipes

The pipe specifications were found from BASAL's product catalog [51] (App. A), and the *BASAL Mufferør ig* and *BASAL Flasrør ig*, the small and large pipes respectively, were modeled accordingly. The concrete pipes were made of a B60 concrete [35]. This corresponds to a cylinder compression strength of 60 MPa and cube compression strength of approximately 75 MPa [57] [58]. Initial simulations were performed by modeling the concrete material using the CDP model. The tabulated tensile stiffening and compression hardening values were scaled correspondingly, to give a theoretical compression strength of $f_c' = 75\,\text{MPa}$. To simulate the loading, the CONWEP model implemented in ABAQUS was employed. The CONWEP model is built for TNT charges, so the mass of C4 was scaled by the relative effectiveness factor of 1.34 to get the equivalent mass of TNT [59].

Since the experimental study was mainly qualitative, it is of interest to achieve simulations that are qualitatively similar. To model the cracking and fracturing of the concrete, element erosion was employed through a subroutine (App. E). Initially all the experimental tests were simulated, and then a few of them have been chosen out for further study which will be discussed in this chapter.

7.1 Small Pipes

The *BASAL Mufferør ig* pipes were modeled using the general purpose brick element C3D8R brick elements, with reduced integration (1 integration point). The general size of the elements was set to 10 mm, which gave 4 elements over the thickness and a total number of 58650 elements. Pressure data was extracted from selected elements on the inner surface of the pipe, at locations corresponding to the center of the pipe and 250 mm, 500 mm, 550 mm and 650 mm from the center. The two outermost element positions matches the locations of the pressure sensors from the experiments.

The small pipe were subjected to pressure loadings from centrically placed C4 charges with sizes ranging between 10 g and 20 g. In the experiments there was observed a change in failure mode between a pipe subjected to 12 g and 14 g C4. In the simulations, the pipe got eroded when subjected to 12 g C4, and even when subjected to 10 g C4 as well (Table 7.1). Furthermore, there is progressively more elements being eroded as the charge increases, but in general the difference is not very large. Some erosion at the muzzle ring is also visible when a loading corresponding to 20 g is utilized, but this was not seen in the experiments.

The simulations give overall decent results, but was not able to capture the various failure modes that was seen for the different loading scenarios. It is mainly the elements in close proximity to the charge that get eroded. As the distance from the charge to the loaded surface increases, consequently the load itself decreases. Therefore, further out from the middle fewer elements are eroded, but longitudinal cracks, in the form of eroded elements along a line, are present (Fig. 7.1). The fragmentation seen in the experiments and the scatter of concrete pieces are not seen, but is not expected either. It is not happening in the simulations because of the way the CONWEP model defines the loading. It bases the loading solely on charge size plus distance and angle to the loaded surface. Therefore, effects such as reflections and leakage of high-pressurized air through cracks are not taken into consideration. For this to be taken into account, it would be necessary with a full FSI-simulation.

Table 7.1 – *Small pipes subjected to* 10 g, 12 g, 15 g *and* 16 g *C4 at* $t = 2\,\mathrm{ms}$. *Field values are tensile damage from 0 (blue) to 1 (red).*

	C4 12 g – 20 g, $t = 2\,\mathrm{ms}$
10 g	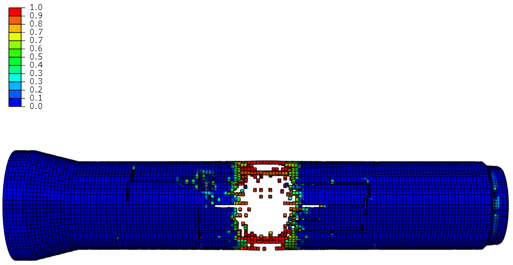 1.0 0.9 0.8 0.7 0.7 0.6 0.5 0.4 0.3 0.3 0.2 0.1 0.0
12 g	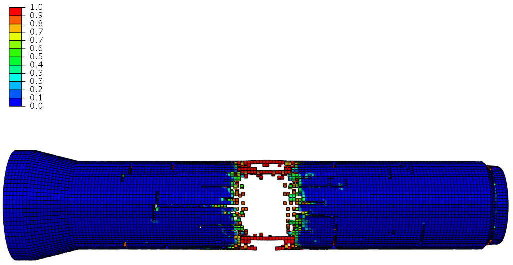 1.0 0.9 0.8 0.7 0.7 0.6 0.5 0.4 0.3 0.3 0.2 0.1 0.0
14 g	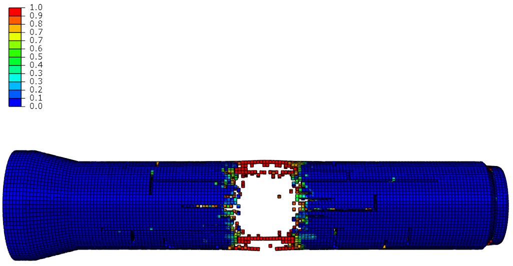 1.0 0.9 0.8 0.7 0.7 0.6 0.5 0.4 0.3 0.3 0.2 0.1 0.0
20 g	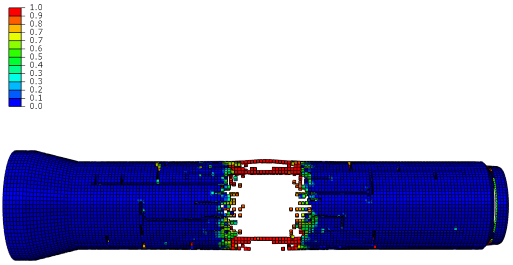 1.0 0.9 0.8 0.7 0.6 0.7 0.6 0.5 0.4 0.3 0.2 0.1 0.0

7.2 Large Pipes - PCC

In similarity to the *BASAL Mufferør ig*, the *BASAL Falsrør ig* was modeled with C3D8R brick elements. The general size was set to 20 mm, which gave 42106 elements in total and 5 elements over the thickness. Also here, pressure data was extracted from selected elements on the inner surface of the pipe, though at locations corresponding to the center of the pipe and 275 mm, 575 mm, 875 mm and 975 mm from the center. The two outermost element positions matches the locations of the pressure sensors from the experiments.

In general the simulations gave quite satisfactory results, though mainly for the larger charge sizes. The erosion of elements was able to reproduce some of the cracks, and the major part of elements in proximity of the charge got eroded. In addition, the amount of damage increases as the loading intensifies (Table 7.2). The damage the muzzle ring is also seen in the simulations, while in the experiments it happened only at 150 g C4, it is seen to happen down to 50 g in the simulations. In the experiments a charge of 50 g yielded no visible damage to the pipe, whereas in the simulation the center part of the pipe got eroded under analogous loading. So the simulations were not able to accurately represent the various failure modes and tend to render more damage than what was seen from experiments. This was also seen in the simulations of the smaller pipes. However, the simulations did qualitatively well in representing the pipes subjected to higher loading, which fragmented. As previously addressed, when using the CONWEP model to simulate the loading, elements are not projected outwards by the blast. Phenomenons such as concrete fragments being blown outwards are then not reproduced.

A sensitivity study has been performed on the large PCC pipes, investigating the effects of altering different parameters. The parameters that will be discussed is the erosion criterion ε_{crit}, the compressive and tensile strength of the concrete, the effect of mesh size and another material model. For this sensitivity study, it was chosen to primarily focus on simulations regarding 50, 100 and 150 g C4. It is useful to focus on the simulation with 50 g, because it was visibly undamaged in the experiments, and this is something to attempt in simulations as well. Furthermore, a loading of 150 g C4 is also convenient to include because it is directly comparable to the simulations performed with reinforced concrete. Lastly, a loading of 100 g C4 provides a reference to ensure a gradual development of damage, as the loading intensifies. Since numerous simulations were conducted, only the most relevant results will be presented and talked about, but some may be mentioned without further discussion.

Table 7.2 – *Large PCC pipes subjected to* 50 g*,* 100 g *and* 150 g *C4 at* $t = 2\,\mathrm{ms}$*. Field values are tensile damage from 0 (blue) to 1 (red).*

	C4 50 g – 150 g, $t = 2\,\mathrm{ms}$
50 g	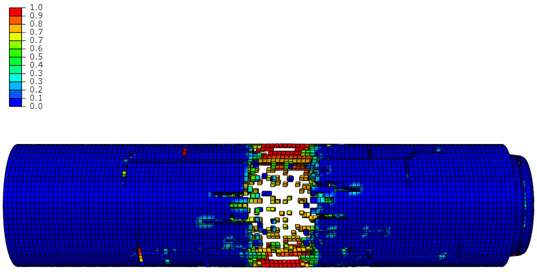 1.0 0.9 0.8 0.7 0.7 0.6 0.5 0.4 0.3 0.3 0.2 0.1 0.0
100 g	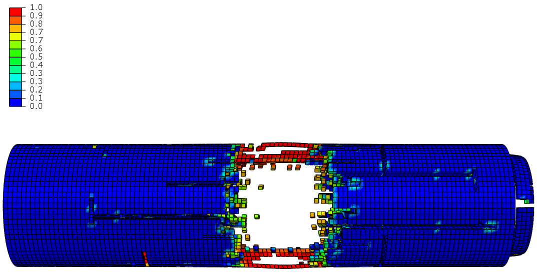 1.0 0.9 0.8 0.7 0.7 0.6 0.5 0.4 0.3 0.3 0.2 0.1 0.0
150 g	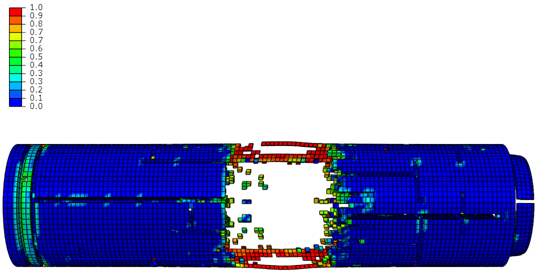 1.0 0.9 0.8 0.7 0.7 0.6 0.5 0.4 0.3 0.3 0.2 0.1 0.0

7.2.1 Effect of erosion criterion

Initially the erosion criterion was set to $\varepsilon_{crit} = 0.02$. Though, from simulations it was observed that the level of destruction was in general to high, especially for the pipe subjected to 50 g C4 (Table 7.2). When increasing ε_{crit}, it means that higher strains are necessary before an element is eroded. This gives a more ductile behavior of the concrete. Fewer elements would be eroded when the criterion is increased, which is also seen in this particular case (Table 7.3). This is desirable considering the experiments showed no visible damage. Yet, there is still quite significant erosion, even when ε_{crit} is as high as 0.10.

The simulations regarding 100 g and 150 g C4 displayed similar characteristics, with less elements being eroded as the erosion criterion was elevated. As the charge was increased, overall more elements were eroded.

7.2.2 Effect of concrete strength

From the product catalog of Basal and concrete standards, it was found that the concrete used for the pipes had a compression strength of 75 MPa [35][57][58]. The strength given in standards are a minimum however, and the actual strength of the concrete is often higher. Information given by the concrete manufacturer, from a concrete cube compression test, specified a compression strength of 83.3 MPa (App. A). It is therefore of interest to study the effect of the compression strength, and whether it is an important parameter to consider when doing these types of simulations.

The J-L configuration of the CDP model was thus scaled accordingly to give three different pipes with theoretical compression strength of 75 MPa, 85 MPa and 100 MPa. A problem occurred however when trying to employ the model with compression strength of 100 MPa. As seen from the numerical study of the concrete cubes, as the compression hardening and tensile stiffening tables are scaled, the stress-strain curve gets increasingly tilted towards the right (Fig. 6.2). It was therefore necessary to also adjust the E-modulus after the empirical model to get the material model to work. This gave material parameters as stated in Table 7.4.

In general, the difference is quite small as the compressive and tensile strength is increased. There are fewer elements that are eroded for higher compression strength, but the overall effect is quite small. The tensile strength is likely to be an influential factor, though it is not altered much under scaling, thus the effect is hard to distinguish.

Cracks seem to be approximately the same length, and damage to the muzzle

Table 7.3 – *Large PCC pipes with $\varepsilon_{crit} \in [0.02, 0.05, 0.10]$ subjected to $50\,\mathrm{g}$ C4 at $t = 2\,\mathrm{ms}$. Field values are tensile damage from 0 (blue) to 1 (red).*

	C4 $50\,\mathrm{g}$, $t = 2\,\mathrm{ms}$
$\varepsilon_{crit} = 0.02$	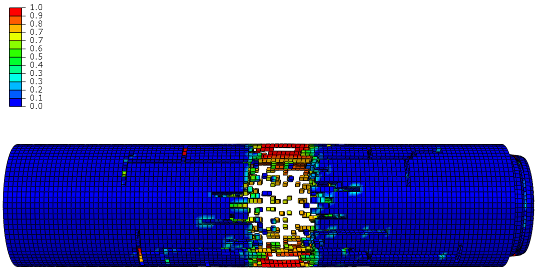 1.0 0.9 0.8 0.7 0.7 0.6 0.5 0.4 0.3 0.3 0.2 0.1 0.0
$\varepsilon_{crit} = 0.05$	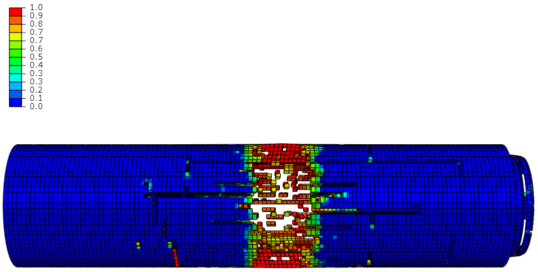 1.0 0.9 0.8 0.7 0.7 0.6 0.5 0.4 0.3 0.3 0.2 0.1 0.0
$\varepsilon_{crit} = 0.10$	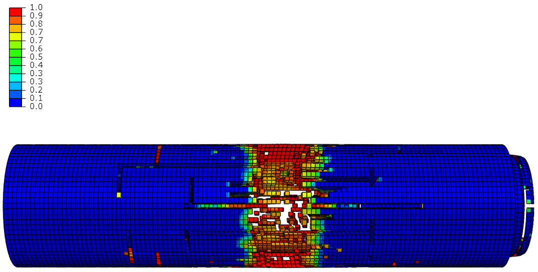 1.0 0.9 0.8 0.7 0.7 0.6 0.5 0.4 0.3 0.3 0.2 0.1 0.0

Table 7.4 – *The different compression strengths and the complementary tensile strength and E-modulus.*

f'_c [MPa]	f'_t [MPa]	E_c [MPa]
75.0	3.0	44651.6
85.0	3.4	47535.3
100.0	4.0	51559.3

ring remains also the same (Table 7.5). Even at at compression strength of 100 MPa, the pipe is still destructed exposed to 50 g C4. These same trends was also present for the pipes subjected to 100 g and 150 g C4, although it was seen that damage to the open end of the pipe got reduced when compression strength increased.

Most notable is the effect of adjusting the E-modulus. The only difference between the top picture in Table 7.2 and Table 7.5 is the adjustment of E-modulus. It is clear that this has a considerable effect, with fewer elements being eroded and less damage around the middle of the pipe. Additionally, cracks appear to be longer and have more damage.

Table 7.5 – *Large PCC pipes with* $f'_c = 75\,\mathrm{MPa}$*,* $f'_c = 85\,\mathrm{MPa}$ *and* $f'_c = 100\,\mathrm{MPa}$ *subjected to* 50 g *C4 at* $t = 2\,\mathrm{ms}$*. Field values are tensile damage from 0 (blue) to 1 (red).*

	C4 50 g, $t = 2\,\mathrm{ms}$
$f'_c = 75\,\mathrm{MPa}$	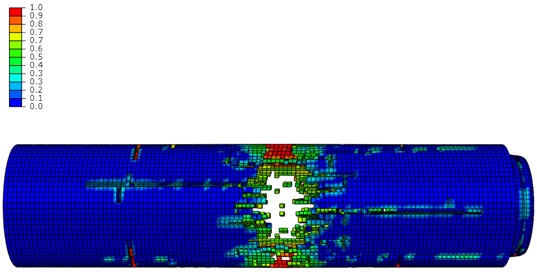 1.0 0.9 0.8 0.7 0.7 0.6 0.5 0.4 0.3 0.3 0.2 0.1 0.0
$f'_c = 85\,\mathrm{MPa}$	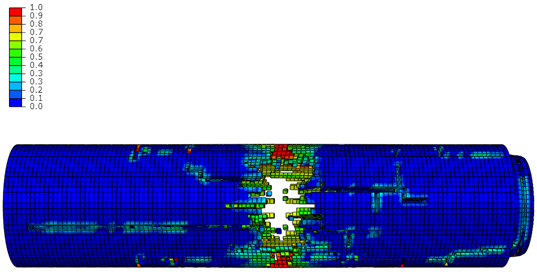 1.0 0.9 0.8 0.7 0.7 0.6 0.5 0.4 0.3 0.3 0.2 0.1 0.0
$f'_c = 100\,\mathrm{MPa}$	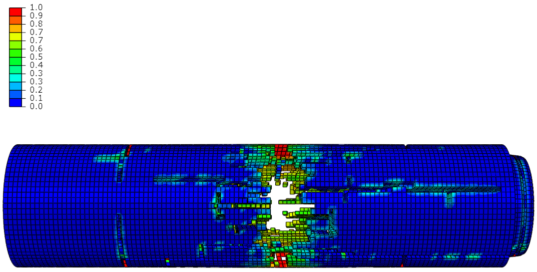 1.0 0.9 0.8 0.7 0.7 0.6 0.5 0.4 0.3 0.3 0.2 0.1 0.0

7.2.3 Effect of mesh size

The initial model was modeled with an average mesh size of 20 mm. This was a suitable mesh size giving decent results and fast computational times. Though, when doing qualitative simulations, the mesh size is important to study to see if more accurate and detailed results can be obtained. In addition to the mesh size of 20 mm, the pipes were simulated with a mesh size of 10 and 5 mm.

Naturally, the change in mesh size has a significant effect on the representation of crack patterns. The refinement of mesh allows for a more detailed depiction of the cracks. From 20 mm to 10 mm elements, cracks become thinner and more refined, but stay approximately the same length. The eroded part in the middle of the pipe also stay about the same (Table 7.6).

The level of detail becomes even higher when regarding the mesh size of 5 mm. There are more cracks in the circumferential direction, which was not present with the more coarse meshes. Additionally, cracks are thinner and longer in extension. The eroded part in the middle of the pipe has approximately the same size as for the other mesh size configurations, but there are much more cracks present in this area (Table 7.6).

The tensile damage in the pipe remained about the same regardless of the element size and the same trends were seen for pipes subjected to 50 g and 100 g C4. The amount of destruction to the pipe still appears to be somewhat more in the simulation compared to the experiments, and altering the mesh size did not seem to affect this. There was still a lot of erosion in the simulation with 50 g C4, even as the mesh was refined. Notably, the smaller element size makes the critical time step for a simulation shorter, thus the simulation with 50 g C4 and element size 5 mm saw some irregularities in the energy balance, but the qualitative results still seemed reasonable. The energy balances for the other simulations were satisfactory.

7.2.4 Effect of material calibration

The previous simulations have been modeled using the J-L configuration of the CDP model [52]. From the simulations of the concrete cubes, it was seen that the configuration proposed by Labibzadeh et al. [56] also gave good results and it is therefore subject to further study.

In general it has been seen that the simulated pipes have been considerably more shattered and fractured than their physical counterpart. Some of the problem could be in the configuration of the material parameters. The parameters proposed in the Lab configuration showed a more gradual post

Table 7.6 – *Large PCC pipes with mesh sizes* 20 mm, 10 mm *and* 5 mm *subjected to* 150 g *C4. Field values are tensile damage from 0 (blue) to 1 (red).*

	C4 150 g
20 mm	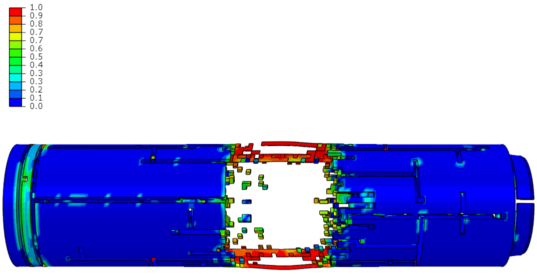 1.0 0.9 0.8 0.7 0.7 0.6 0.5 0.4 0.3 0.3 0.2 0.1 0.0
10 mm	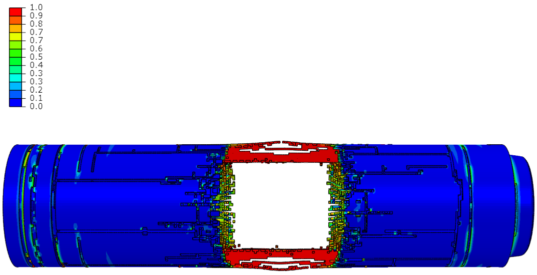 1.0 0.9 0.8 0.7 0.7 0.6 0.5 0.4 0.3 0.3 0.2 0.1 0.0
5 mm	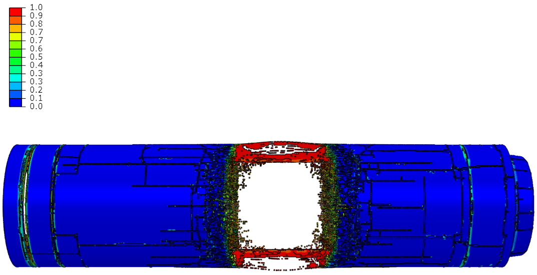 1.0 0.9 0.8 0.7 0.7 0.6 0.5 0.4 0.3 0.3 0.2 0.1 0.0

yield softening compared to the J-L configuration. In the J-L configuration, the post yield softening was very abrupt, especially without the adjustment of the E-modulus. The simulations discussed here have both adjusted the E-modulus after the empirical relation (Eq. (6.1)). A theoretical compression strength of $f'_c = 75\,\text{MPa}$ was used, giving material parameters as stated in Table 7.7. Additionally, from the cube tests, the Lab configuration was seen to give a higher measured compressive strength than the theoretical compression strength; it also has a higher tensile strength than the J-L configuration.

It is seen that there is significantly less erosion to the pipe with the Lab configuration, but there is still some (Table 7.8). The less abrupt strain-softening behavior which was seen in the J-L configuration with adjusted E-modulus and in the Lab configuration, appears to give a better representation of the concrete behavior. The higher tensile strength of the Lab configuration might also contribute to reduce erosion. Cracks are approximately the same length, but there is less tensile damage to the pipe with material parameters from Labibzadeh et al.

Table 7.7 – *The material configurations by Jankowiak and Lodygowski [60] and Labibzadeh et al. [56] and the corresponding compression strengths, tensile strengths and E-modulus.*

Configuration	f'_c [MPa]	f'_t [MPa]	E_c [MPa]
J-L	75.0	3.0	44651.6
Lab	75.0	7.0	44651.6

Table 7.8 – *Large PCC pipes with CDP model configuration by Jankowiak and Lodygowski [60] and Labibzadeh et al. [56] subjected to* 50 g *C4. Field values are tensile damage from 0 (blue) to 1 (red).*

	C4 50 g
Jan-Lod	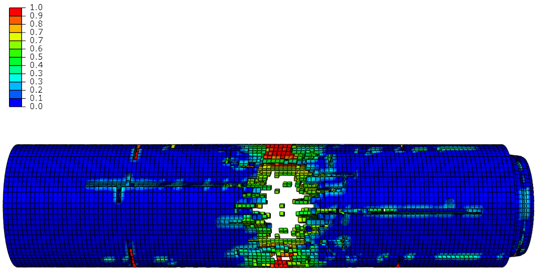 1.0 0.9 0.8 0.7 0.7 0.6 0.5 0.4 0.3 0.3 0.2 0.1 0.0
Labibzadeh et al.	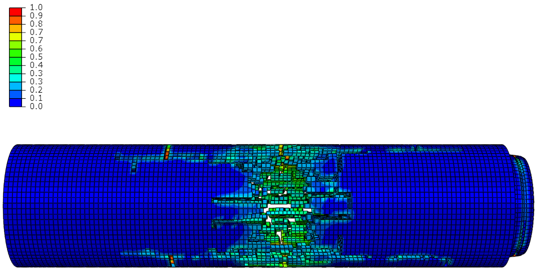 1.0 0.9 0.8 0.7 0.7 0.6 0.5 0.4 0.3 0.3 0.2 0.1 0.0

7.3 Large Pipe - Reinforced

The reinforced *Basal Falsrør ig* was modeled in the same way as the unreinforced, using C3D8R brick elements. Only difference is that reinforcements were embedded in the model. The reinforcements were modeled with B31 2-node linear beam elements. In total there was 12 longitudinal rods, 8 mm in diameter, mid-placed across the thickness of the cross section and evenly distanced in the circumferential direction. In the reinforced *Basal Falsrør ig*, the circumferential reinforcement was originally a wound rebar helix with 100 mm of elevation per round. For the simplicity of the model, the circumferential reinforcement was modeled as multiple steel rings placed along the length of the pipe, with an internal spacing of 100 mm. This totaled a number of 22 steel rings in the pipe. This gave a total of 45038 elements. The steel behavior was modeled using a Johnson-Cook hardening model. It has been chosen to focus on loading scenarios of 150 g, 300 g and 500 g C4, to observe the gradual increase of damage as the loading is intensified.

The simulations gave predominately good results. The behavior of concrete is notoriously difficult to simulate, with strain softening and excessive erosion, thus the introduction of steel in the model seemed to act as a regularization. In the experiments the reinforced pipe subjected to 150 g C4 experienced some small cracks. This is also shown in the simulations, although the crack patterns are more rough due to the relatively coarse mesh and the extension of the cracks are somewhat shorter. The muzzle ring is still intact, even though it seems to experience a lot of damage (Table 7.9).

As the loading is increased to 300 g C4, the pipe gets more eroded; reinforcements are visible through the cracks. From experiments it was seen that there were large longitudinal cracks, and some spalling. Thus the simulation appear to give some more destruction in vicinity of the charge, but the extension of the cracks is significantly less. The muzzle ring also stays unbroken.

At 500 g C4 the pipe gets significantly eroded. The reinforcements are visible through the cracks, in similarity to the experiments. There is tensile damage extending from the middle of the pipe and in the pipe end. Though, the elements farther out are not eroded, thus the extension of the cracks and destruction to the narrow pipe end does not resemble the physical tests.

Table 7.9 – *Large reinforced pipes subjected to* 150 g, 300 g *and* 500 g *C4. Field values are tensile damage from 0 (blue) to 1 (red).*

	C4 150 g – 500 g, $t = 2$ ms
150 g	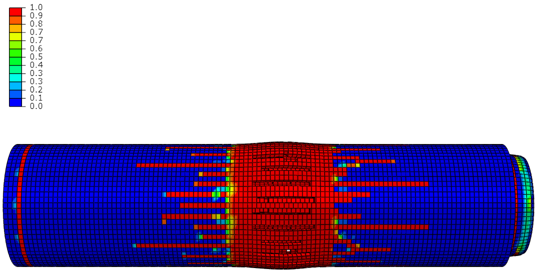
300 g	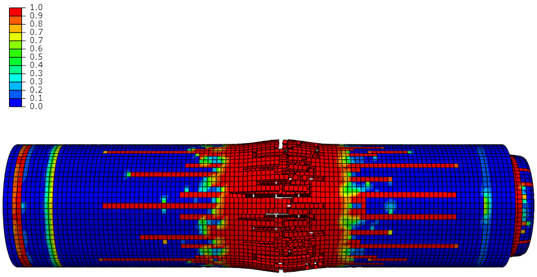
500 g	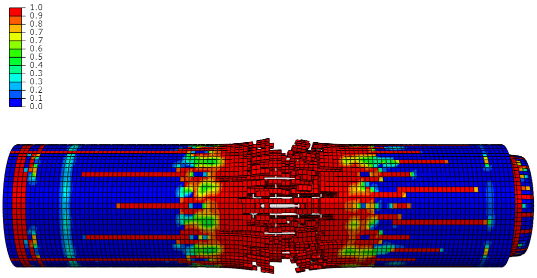

7.3.1 Effect of erosion criterion

As discussed previously, altering the erosion criterion ε_{crit} involves altering at which equivalent strain an element gets eroded. The damage remains fairly unchanged as ε_{crit} is increased. The most notable change is in the number of elements eroded and the failure mode of the pipe. This becomes especially evident when the pipe is exposed to 500 g C4. At $\varepsilon_{crit} = 0.02$ the pipe resembles the experiments quite well, but as ε_{crit} is increased to $\varepsilon_{crit} = 0.05$ the pipe only suffers some cracks and remains partially intact at the middle (Table 7.10). With $\varepsilon_{crit} = 0.10$ there are almost no elements being eroded, it is nearly pure deformation.

In general, as ε_{crit} is increased the pipe goes from full breach of the pipe wall, to cracking and then to almost solely deformation. The same tendencies were seen for simulations with 150 and 300 g C4, though for 150 g C4 there was initially only cracking (Table 7.9). The pipe loses its brittle behavior and becomes more ductile. Although the change of ε_{crit} did not yield more physical results, it is still interesting to study the effect it has.

7.3.2 Effect of concrete strength

To study the effect of concrete strength, the material parameters by Jangoviak and Lodygowski [52] in the CDP model were scaled equally as for the unreinforced pipes, to give three different pipes with theoretical compression strength of 75 MPa, 85 MPa and 100 MPa (Table 7.4). The E-modulus was also modified after the empirical model (Eq. 6.1) to get the scaled material model to work.

As the concrete strength increases, there is nearly no change whatsoever (Table 7.11). The reinforcements absorb most of the tensile stress caused by the pressure from the blast, thus changing the strength of the concrete gives little effect. The amount of damage is approximately unchanged, but crack lengths seem to increase as the strength increases.

The adjustment to the E-modulus does provide some effect. Comparing the last picture of Table 7.9 to the first picture of Table 7.11, it is seen that there are significantly less elements eroded at the middle of the pipe, while the crack lengths remain about the same. This is not unreasonable, considering that increasing the E-modulus gave a stiffer behavior and also a higher strength compared to the theoretical compression strength.

Table 7.10 – *Large reinforced pipes with* $\varepsilon_{crit} \in [0.02, 0.05, 0.10]$ *subjected to* $500\,\mathrm{g}$ *C4. Field values are tensile damage from 0 (blue) to 1 (red).*

	$C4$ $500\,\mathrm{g}$, $t = 2\,\mathrm{ms}$
$\varepsilon_{crit} = 0.02$	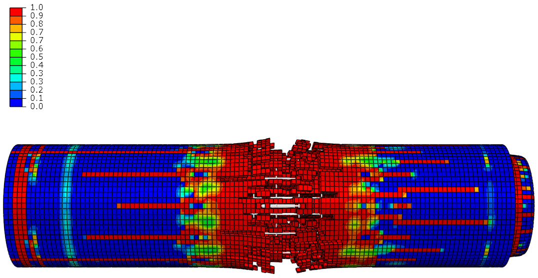 1.0 0.9 0.8 0.7 0.7 0.6 0.5 0.4 0.3 0.3 0.2 0.1 0.0
$\varepsilon_{crit} = 0.05$	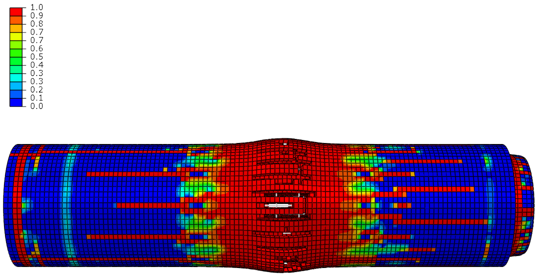 1.0 0.9 0.8 0.7 0.7 0.6 0.5 0.4 0.3 0.3 0.2 0.1 0.0
$\varepsilon_{crit} = 0.10$	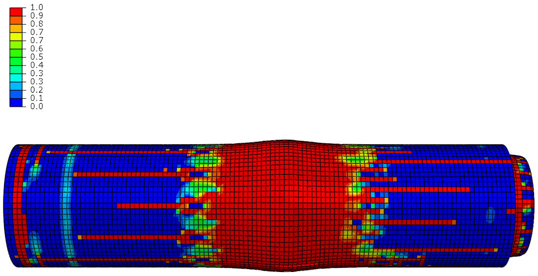 1.0 0.9 0.8 0.7 0.7 0.6 0.5 0.4 0.3 0.3 0.2 0.1 0.0

Table 7.11 – *Large reinforced pipes with* $f'_c = 75\,\mathrm{MPa}$*,* $f'_c = 85\,\mathrm{MPa}$ *and* $f'_c = 100\,\mathrm{MPa}$ *subjected to* 500 g *C4. Field values are tensile damage from 0 (blue) to 1 (red).*

	C4 500 g, $t = 2\,\mathrm{ms}$
$f'_c = 75\,\mathrm{MPa}$	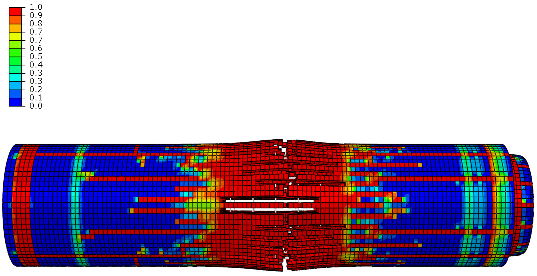 1.0 0.9 0.8 0.7 0.7 0.6 0.5 0.4 0.3 0.3 0.2 0.1 0.0
$f'_c = 85\,\mathrm{MPa}$	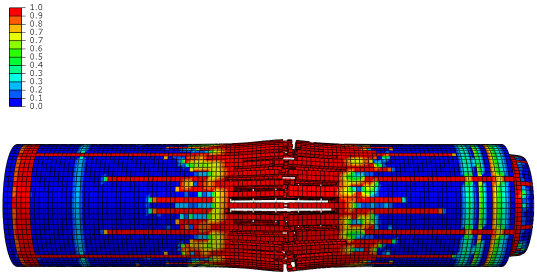 1.0 0.9 0.8 0.7 0.7 0.6 0.5 0.4 0.3 0.3 0.2 0.1 0.0
$f'_c = 100\,\mathrm{MPa}$	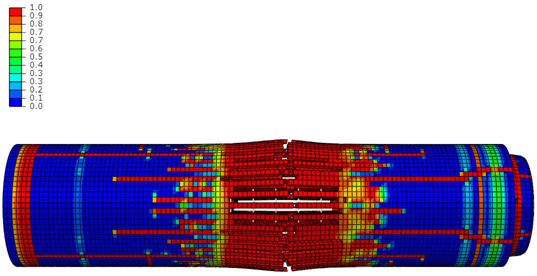 1.0 0.9 0.8 0.7 0.7 0.6 0.5 0.4 0.3 0.3 0.2 0.1 0.0

7.3.3 Effect of mesh size

In similarity to the plain concrete pipes, the initial model was modeled with an average mesh size of 20 mm. To study the effect of mesh size two other pipes were modeled with a mesh size of 5 mm and 10 mm. Again it is observed that altering the element size has a notable influence on the reproduction and details of cracks and crack patterns. When the element size is decreased from 20 mm to 10 mm, the cracks become thinner and extends more out from the middle (Table 7.12). More cracks in the circumferential direction also appear around the middle of the pipe. There is also less of the reinforcement being exposed as mesh is more detailed. Larger elements imply that when an element first is eroded, a larger part of the pipe is removed in contrary to the smaller elements. This leaves more singular unconnected elements when the element size is smaller, concealing more of the rebar.

When the element size becomes as small as 5 mm, the level of detail becomes quite good. Characteristics that were not previously present appear, such as cracks in the muzzle ring. In general, cracks also get thinner, longer in extension and more cracks in the circumferential direction also become present. The mesh size did not seem to influence the tensile damage in the pipe, although the distribution of damage became more detailed as the element size became smaller. The same tendencies were observed for the two other pipes subjected to 150 and 300 g C4.

As the mesh is refined, the simulations resemble the experimental tests more. Using a mesh size of 5 mm, the likeness is very good. In the physical test there was continuous cracks from the middle out to the narrow end, but these cracks were very thin (less than 5 mm in width). Therefore, it is not expected that the simulation is able to capture this. The widest and most prominent cracks however are well represented. From experiments it was seen that the cracks were regularly distanced in correlation to the reinforcement, this is also reproduced in the simulations, though not to the same degree; the crack patterns are somewhat more irregular.

7.3.4 Effect of material calibration

The previous simulations have been modeled using the Jankowiak and Lodygowski [52] configuration of the CDP model. It is of interest to also look into the configuration proposed by Labedzidah et al. [56]. The scaled material parameters are given in Table 7.7.

Evidently, there is less tensile damage when using the Lab configuration compared to J-L (Table 7.13). The former gives a higher tensile strength,

Table 7.12 – *Large reinforced pipes with mesh sizes* 20 mm, 10 mm *and* 5 mm *subjected to* 500 g *C4. Field values are tensile damage from 0 (blue) to 1 (red).*

	C4 500 g, $t = 2\,\text{ms}$
20 mm	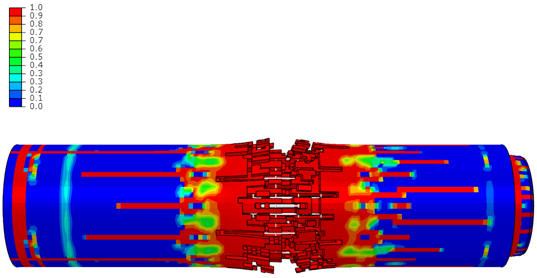 1.0 0.9 0.8 0.7 0.7 0.6 0.5 0.4 0.3 0.3 0.2 0.1 0.0
10 mm	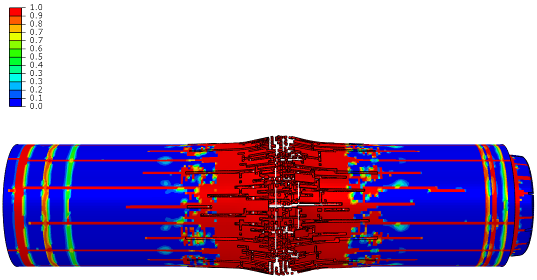 1.0 0.9 0.8 0.7 0.7 0.6 0.5 0.4 0.3 0.3 0.2 0.1 0.0
5 mm	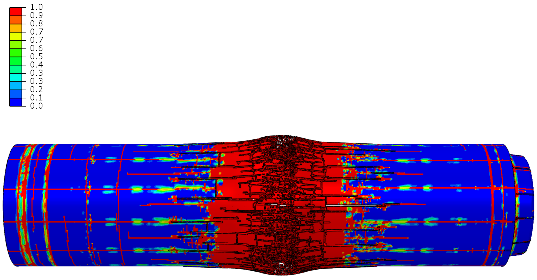 1.0 0.9 0.8 0.7 0.7 0.6 0.5 0.4 0.3 0.3 0.2 0.1 0.0

Table 7.13 – *Large reinforced pipes with CDP model configuration by Jankowiak Lodygowski [60] and Labibzadeh et al. [56] subjected to* 500 g *C4. Field values are tensile damage from 0 (blue) to 1 (red).*

	C4 500 g, $t = 2\,\mathrm{ms}$
Jan-Lod	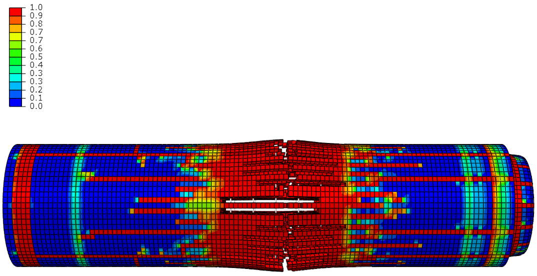 1.0 0.9 0.8 0.7 0.7 0.6 0.5 0.4 0.3 0.3 0.2 0.1 0.0
Lab et al.	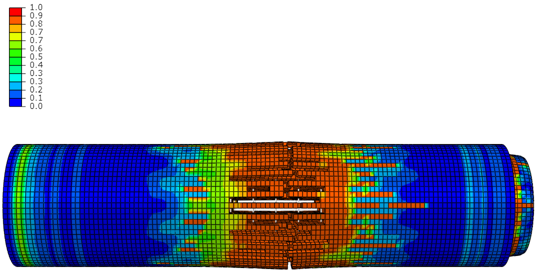 1.0 0.9 0.8 0.7 0.7 0.6 0.5 0.4 0.3 0.3 0.2 0.1 0.0

when both are scaled to the same compression strength. It appears to be a bit more erosion happening in the pipe with the J-L configuration, with crack lengths being longer. In neither of the simulations the muzzle ring is destroyed, but as seen from the previous subsection, this could be a more mesh related issue rather than connected to the material model.

In general the Lab material configuration gives promising results and is an alternative to consider as a substitute for the configuration proposed by Jankowiak and Lodygowski.

7.4 Pressure considerations

During the experiments the pressure was measured at various locations. In the simulations, pressure data was extracted from various elements on the inner surface of the pipe (Table 7.14). This provides a comparison for the loading subjected to the pipe in the experiments and the simulation. It should be noted that at times, the experimental pressure readings suffered

Table 7.14 – *Sensor locations from simulations for the large pipes. Distance is taken from the middle of the pipe, outwards toward the narrow end.*

Sensor	X	Y	Z	7	8
L	0 mm	275 mm	575 mm	875 mm	975 mm

some problems; exposed to very high pressure, the pressure sensor would be saturated and not able to record the highest magnitudes. Occasionally, some of the pressure sensors malfunctioned and was unable to record pressure data. Also, in some of the experiments, the part of the pipe the pressure sensors were drilled into, was knocked off by the force of the blast.

7.4.1 CONWEP model

It was expected that the CONWEP model would give a lower pressure than observed in the experiments. The CONWEP model does not take into account effects such as shock reflections, but rather gives a pressure-time loading on a surface based on the distance and angle from the blast origin and the size of the blast. The shock wave is thus propagating uniformly in shape outwards from the center of the pipe, applying pressure on the surface it moves over. The magnitude of the pressure is seen to decrease as distance increases, and is additionally decreased as the angle between the surface normal and the vector from the surface to the blast origin increases (Table. 7.15) (Fig. 7.1) [27].

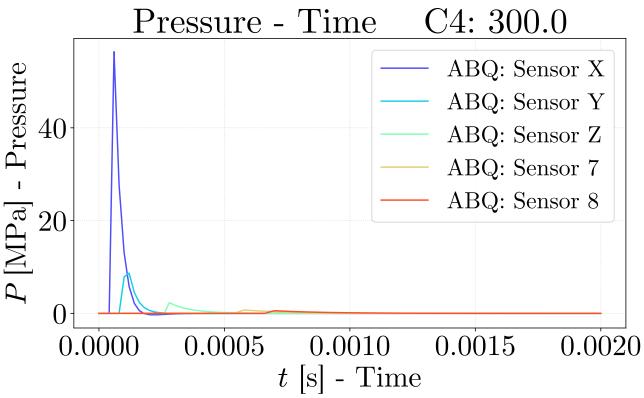

Figure 7.1 – *Pressure-time history for the various sensor locations in ABAQUS.*

In physical experiments effects such as reflections and mach fronts are expected to subject a higher pressure on the pipe. For the sake of validating whether the simulated pressure is at any point near what is measured, the pressure was extracted from a surface at the middle of the pipe, where the pressure would be the highest. This fictional sensor is denoted sensor X. Pressure was also extracted from two additional surfaces to better observe how the magnitude of the pressure decreases in the pipe. These surfaces were located 275 mm and 575 mm from the center, which are dubbed sensor Y and sensor Z respectively. As a reminder, pressure sensors 7 and 8 are located 875 mm and 975 mm from the center respectively, in both simulations and experiments.

It is seen that the simulated pressure near the opening of the pipe is many times lower than what is seen in the experiments (Fig. 7.2a). For a simulated reinforced pipe loaded by the CONWEP model by a charge equivalent to 300 g C4, the highest of the pressure readings near the opening, sensor 7, reached merely 0.7 MPa (Table 7.18). The pressure recorded in the experimental test however, gave a maximum peak of approximately 51 MPa. The recorded pressure is thus over 60 times larger than the simulated at the end of the pipe, which is quite significant. The simulated pressure at the middle of the pipe, in sensor X, reaches a peak of 56.4 MPa which is slightly higher than the peak experimental pressure. Though, the impulse of the simulated loading is small compared to the experimental, seeing that the positive time duration of the pressure-time curve is significantly smaller (Fig. 7.1). The larger impulse seen in the experiments might be due to some afterburn effects, which are not captured by the CONWEP model.

An interesting observation is that the pressure recorded from sensor 7 and 8 in the simulations correlating well with sensor 1 and 4 from the experiments (Fig. 7.2b). Sensor 1 and 4 are the first sensors placed outside the pipe, approximately 210 mm from the opening. With a charge size of 300 g, the maximum recorded pressure in experimental sensor 1 and 4 was approximately 2.6 MPa in both of them. This is a significant reduction in peak pressure only a few centimeters outside the pipe. The shock wave is no longer confined and is thus able to expand into free air, and loses its pressure and energy more rapidly. In the CONWEP model the shock wave is modeled as if it were expanding in free air, and it is interesting to note how much more accurate it is once the shock wave in the problem starts to expand as well. The pressure is still higher in the experiments, but it is important to keep in mind that the shock has been freely expanding for a shorter distance.

Another aspect to consider is the time of arrival of the shock wave. It does not have a large influence of the loading scenario, but is still interesting to note. In general, the arrival time at sensor 7 and 8 of the shock wave in simulations and experiments correlate quite well. The error is generally in the magnitude of 0.1 ms while the duration of the simulation lasts for 2 ms. The difference in arrival time compared to the simulation time is usually around 10 %, and within a range of 5 % to 20 %. It is clear that the CONWEP model is able to satisfyingly predict the arrival time of the shock wave. Though, once again the correlation is stronger with experimental sensors 1 and 4. The difference between sensor 8 in the simulations and experimental sensors 1 and 4 are usually below 5% of the total simulation time, and in many cases below 1%. The shock wave in the experiments thus propagate a little faster, but this is reasonable since it conserves more energy by being confined.

The CONWEP model is not really intended for these types of problems. When working in confined spaces it looses a lot of its capability, because it does not consider effects such as reflections. Yet, it is still interesting to see observe how well it performs. It gave reasonable results when simulating the plain concrete pipes, and simulating the reinforced pipes it gave a surprisingly good qualitative result. One weakness was that it was not able to model the destruction of the pipe farther out from the middle. Analyzing the pressure-time history in the pipe it becomes evident why. Though, it provides a simple yet good estimation of the problem.

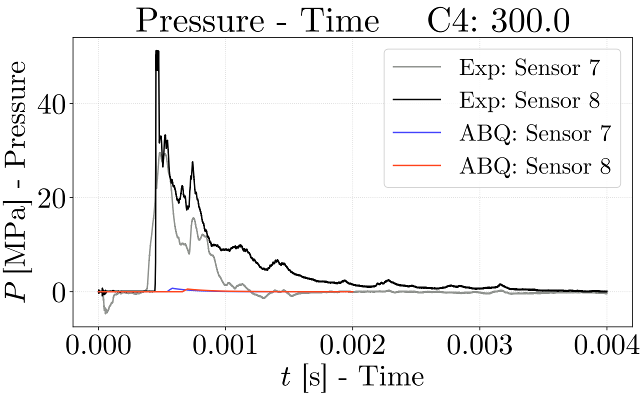

(a) *Pressure-time history for sensor 7 and 8 in ABAQUS, compared to sensor 7 and 8 from the experiments.*

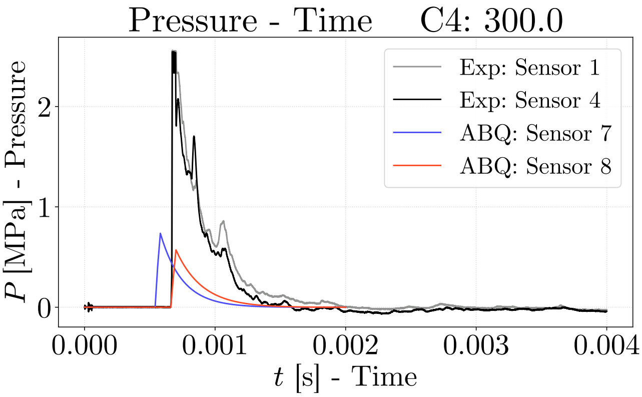

(b) *Pressure-time history for sensor 7 and 8 in ABAQUS, compared to sensor 1 and 4 from the experiments.*

Figure 7.2 – *Comparison of different pressure sensors from simulations and experiments.*

Table 7.15 – *Propagation of pressure* [MPa] *with the CONWEP model, for a charge size of* 300 g.

	CONWEP - 300 g C4
$t = 0.1\,\mathrm{ms}$	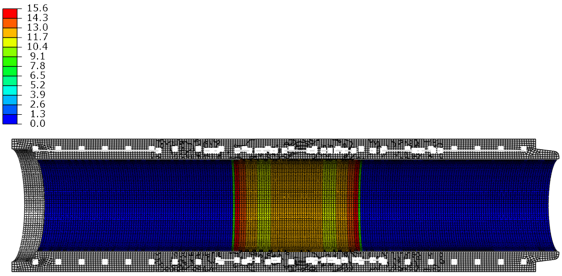 15.6 14.3 13.0 11.7 10.4 9.1 7.8 6.5 5.2 3.9 2.6 1.3 0.0
$t = 0.2\,\mathrm{ms}$	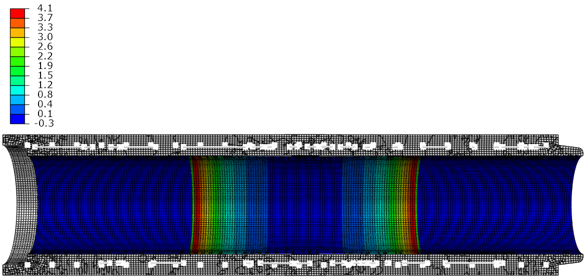 4.1 3.7 3.3 3.0 2.6 2.2 1.9 1.5 1.2 0.8 0.4 0.1 -0.3
$t = 0.4\,\mathrm{ms}$	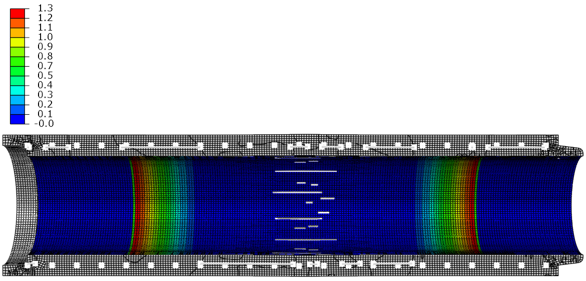 1.3 1.2 1.1 1.0 0.9 0.8 0.7 0.5 0.4 0.3 0.2 0.1 -0.0
$t = 1.2\,\mathrm{ms}$	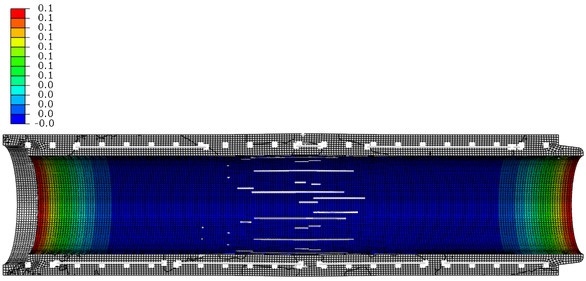 0.1 0.1 0.1 0.1 0.1 0.1 0.1 0.1 0.0 0.0 0.0 0.0 -0.0

7.4.2 CFD simulations

To gain insight in the possibilities of other loading application methods, and to try to get a more realistic pressure distribution on the pipe, it was initially intended to perform Coupled Eulerian Lagrangian (CEL) analyses in ABAQUS. Unfortunately, it proved to be quite a tedious task to get a functioning model. Despite large efforts and extensive tweaking, the solver was not able to provide useful results before it exited with errors. For the interested reader, the next paragraph will go through some of the problems encountered and efforts made in an attempt to find a solution. It was eventually chosen to perform Eulerian analyses in Europlexus.

CEL troubleshooting

The JWL formulation was used to model the explosive which propagated in an Eulerian domain. In the numerical analysis, as the blast front approached the pipe wall, the simulation was exited prematurely with errors reporting about excessive deformation in some of the Eulerian elements. To cope with this problem it was first tested with simple remedies such as scaling the time increment and altering mesh size. This did little to improve the model however. It was then further attempted with more sophisticated methods. Excessive deformation of elements could be due to the fast movement of the shock front excessively distorting the elements in the Lagrangian phase of the time increment. By inspiration from a previous master thesis [61], also conducting CEL analyses in ABAQUS, a flux limit ratio was therefore introduced. The flux limit ratio restricts material to flow across only a fraction of an element in each time step, and is a way of reducing the time increment size when dealing with high velocities like those occurring in blasts. The flux limit ratio was set to 0.1 which is the minimum recommended by documentation [27]. Additionally, adaptive mesh refinement was activated in the Eulerian domain with a refinement criterion related to the density gradient across an element, aimed at refining the mesh near the shock front and keeping a relatively coarse mesh otherwise to reduce computational time. It was also postulated that this would reduce the gradient across elements and thereby the shock.

On this improved model, a small parametric study was performed, altering the values of the linear bulk viscosity and the quadratic bulk viscosity. In general, the two bulk viscosities introduce damping associated with the volumetric straining, and are intended to improve the modeling of high speed dynamic events. Bulk viscosity is included in ABAQUS/Explicit, with default values for the linear and quadratic parameters of $b_1 = 0.06$ and $b_2 = 1.2$ respectively. In the parameter study these values were adjusted independently while the other was held constant at its default value. Improvements were seen both when the linear and quadratic bulk viscosity was increased. For a value of $b_2 = 2.4$ the simulation lasted for 0.4 ms of the total simulation time of 2 ms, before exiting with errors. In comparison, without the efforts listed above, the simulation would last for 0.28 ms. The improvements were thus not very large, and due to time limitations it was chosen to abandon ABAQUS and use Europlexus instead, which is more suited for Eulerian simulations.

Europlexus simulations

Eulerian simulations were conducted in Europlexus to provide a comparison to the CONWEP model. Europlexus is preferable to ABAQUS/Explicit when it comes to performing Eulerian analyses, as it allows the use of Cell-Centred Finite Volumes (CCFV) elements where all variables are discretized at the volume centres and fluxes are calculated across element faces to ensure conservation of mass, momentum and energy [10].

In Europlexus the JWL EOS was used to model the C4 explosive, where material constants for the explosive was found from literature [29]. Since the JWL is simply assigned as a material, the mass of the charge was determined by the size of the spherical part and material density. Only a quarter of the inner volume of the larger pipes were modeled due to the symmetry of the problem. In addition, parts of the volume extending outside the opening of the pipe was also modeled in an effort to capture the effects as the shock wave expands into free air. Pressure data was extracted from selected elements corresponding to the pressure sensors 7 and 8 from the experimental tests, and three additional locations in similarity to the ABAQUS simulations (Table 7.14).

The first visual impressions makes it evident that Europlexus is able to describe the propagation of the shock wave in a far more advanced way. As an example it has been chosen to focus on a charge size of 300 g. In the first tenths of a millisecond, the pressure is propagating spherically outwards until it reaches the boundary, i.e. pipe wall, and thereby gets reflected (Table 7.16). As the blast continues the shock front becomes more one-dimensional along the longitudinal axis of the pipe. Thus, it appears that it is only the part of the wall in proximity to the charge that receives head-on loading. Farther out towards the pipe ends, the loading becomes side-on.

The maximum pressure is seen to decrease as the blast expands. Yet, the most notable difference from the CONWEP model, is that the pressure behind the shock front, in the center region of the pipe, remains quite high even after the shock front has left the pipe. In the CONWEP model the

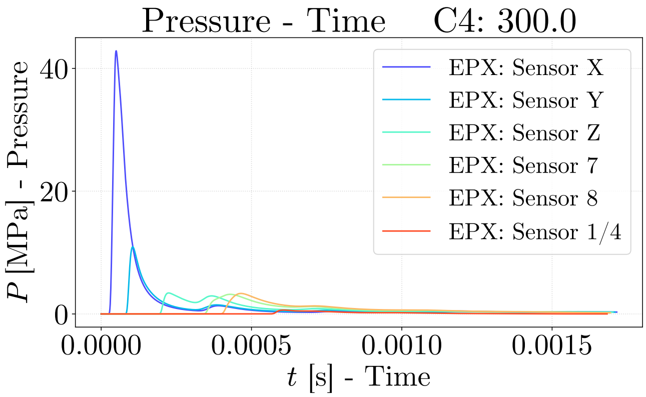

Figure 7.3 – *Pressure-time history for the various sensor locations in Europlexus.*

pressure in the center part of the pipe returned to ambient pressure shortly after the shock wave had propagated further out. It is clear that the pressure distribution simulated in Europlexus is more physical, and it also correlates better with observations from the high speed footage recorded during the experiments. In the experimental footage, it was seen that after the initial shock wave, high pressure air was still present in the pipe; pushing through cracks and scattering fragments. However, at $t = 1.2\,\text{ms}$ there seems to be some inconsistencies across the boundary, which might indicate that the solution is not completely converged.

Though the pressure distribution seemed reasonable, it did underestimate the magnitude of the pressure by quite a lot. For a charge size of 300 g the peak pressure recorded in the tests at sensors 7 and 8 are 31.29 MPa and 51.25 MPa respectively (Table 7.19). Europlexus estimates a peak pressure of 3.20 MPa and 3.34 MPa at these locations. It is then off by a factor of 10 at sensor 7, which is a general trend for the other measurements and simulations as well. Anyhow, the arrival time of the shock wave was remarkably well predicted by Europlexus. It was seen to be predicted within 4 %, of the total simulation time of 2 ms, in all instances except one. The arrival time was often seen to be estimated within 1% in several of the instances.

The shape of the pressure-time curve is slightly more rounded and the maximum pressure is seen to decrease less over the length of the pipe in the CFD simulations, compared to the CONWEP model (Fig. 7.3)(Table 7.19). Additionally, there are small fluctuations present in the pressure-time histories, implying reflections of the blast wave.

In the experiments it is seen that the peak pressure increases and arrival

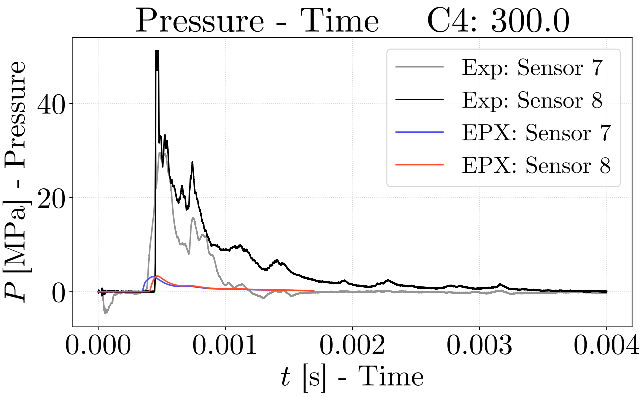

Figure 7.4 – *Pressure-time history for sensor 7 and 8 in Europlexus, compared to sensor 7 and 8 from experiments.*

time decreases as the charge size is increased (Table 7.17). This effect is also captured by the Eulerian simulations in Europlexus (Table 7.19) and in ABAQUS (Table 7.18). Although the peak pressure was underestimated by the JWL EOS in Europlexus, it could for future analyses be an option to upscale the charge size to achieve the desired pressure loading. Kristoffersen et al. [9] also had to scale up the charge size to obtain significant damage to the concrete tubes. When scaling up the charge size, note that the arrival time of the shock wave at a given point will decrease. One should then be aware that the strain rate to the material might increase, if strain rate dependency is a matter.

Table 7.16 – *Propagation of blast wave of* 300 g *C4 simulated in Europlexus. Note that units are in Pascals at the legend.*

	Europlexus - 300 g C4
$t = 0.1\,\mathrm{ms}$	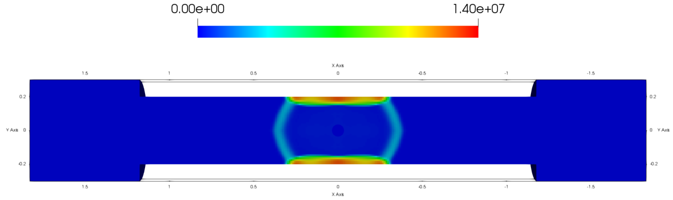
$t = 0.2\,\mathrm{ms}$	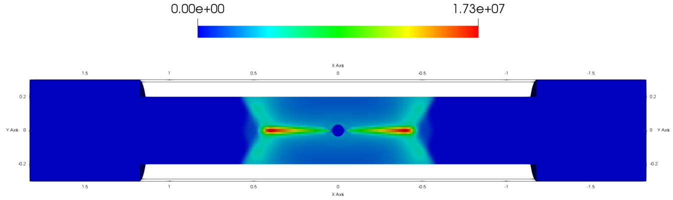
$t = 0.4\,\mathrm{ms}$	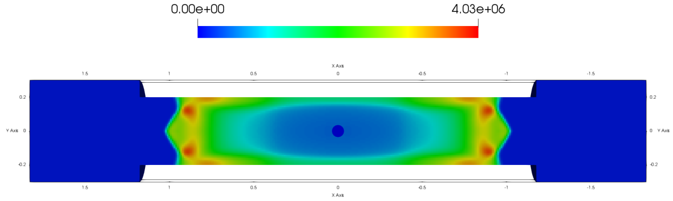
$t = 1.2\,\mathrm{ms}$	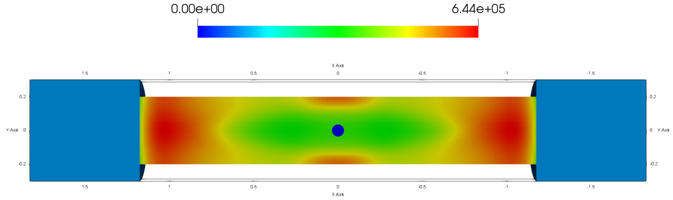

Table 7.17 – *Maximum pressure and arrival times at the different sensors from experimental tests.*

W	S1		S4		S7		S8	
	P_{max}	t_a	P_{max}	t_a	P_{max}	t_a	P_{max}	t_a
[g]	[MPa]	[ms]	[MPa]	[ms]	[MPa]	[ms]	[MPa]	[ms]
50.00	0.95	1.19	0.63	1.26	7.82	0.66	11.17	0.74
100.00	0.99	0.94	0.93	0.97	9.76	0.55	16.56	0.61
150.00	1.29	1.06	1.31	0.97	1.17 [1]	- [1]	17.82	0.76
150.00 (R)	1.29	0.81	1.12	0.82	4.18 [1]	- [1]	25.67	0.54
300.00	2.56 [2]	0.67	2.54 [2]	0.67	31.29	0.43	51.25 [2]	0.45
500.00	2.56 [2]	0.55	2.54 [2]	0.68	19.47 [3]	0.37	47.00 [3]	0.37

[1] Pressure sensor malfunction.
[2] Pressure sensor saturation.
[3] Pressure sensors blown off from pipe.

Table 7.18 – *Maximum pressure and arrival times at the different sensors from ABAQUS.*

W	S7		S8		SX		SY		SZ	
	P_{max}	t_a	P_{max}	t_a	P_{max}	t_a	P_{max}	t_a	P_{max}	t_a
[g]	[MPa]	[ms]	[MPa]	[ms]	[MPa]	[ms]	[MPa]	[ms]	[MPa]	[ms]
50.00	0.18	0.94	0.15	1.12	11.29	0.08	2.31	0.16	0.48	0.46
100.00	0.30	0.78	0.24	0.94	35.54	0.06	5.46	0.14	0.96	0.38
150.00	0.44	0.70	0.32	0.84	40.45	0.06	4.88	0.12	1.32	0.34
150.00	0.45	0.70	0.32	0.84	41.48	0.06	5.03	0.12	1.33	0.34
300.00	0.74	0.56	0.57	0.68	56.40	0.06	8.68	0.10	2.30	0.28
500.00	1.11	0.48	0.87	0.60	128.18	0.04	16.93	0.10	3.61	0.24

Table 7.19 – *Maximum pressure and arrival times at the different sensors from Europlexus.*

W	S7		S8		SX		SY		SZ	
	P_{max}	t_a	P_{max}	t_a	P_{max}	t_a	P_{max}	t_a	P_{max}	t_a
[g]	[MPa]	[ms]	[MPa]	[ms]	[MPa]	[ms]	[MPa]	[ms]	[MPa]	[ms]
50.00	0.80	0.70	0.68	0.80	8.55	0.05	2.25	0.15	0.73	0.38
100.00	1.51	0.54	1.38	0.62	15.91	0.05	4.28	0.12	1.33	0.29
150.00	2.08	0.47	2.09	0.54	24.03	0.04	6.17	0.11	1.91	0.26
300.00	3.20	0.36	3.34	0.42	42.86	0.04	10.93	0.09	3.42	0.21

Chapter 8

Concluding Remarks

8.1 Summary and Discussion

The aim of this thesis has been to investigate the behavior of concrete pipes subjected to blast loading. Several experimental tests were conducted during the course of this thesis. Compression tests were performed on concrete cubes. The compression process of three of the cubes was tracked by a camera and later post-processed in a DIC analysis in an effort to establish the stress-strain relationship for concrete under compression. Moreover, blast tests were performed on three different types of concrete pipes. The pipes used in the tests were the 200 mm inner diameter plain concrete *BASAL Mufferør ig* plus the 400 mm inner diameter *BASAL Falsrør ig*, both plain concrete and reinforced; provided by the concrete pipe manufacturer BASAL [51]. The tests were filmed with two high speed cameras, Phantom Miro LC310 (1280x800 @ 3268 fps), one camera filming from the front and one from the side. The pipe explosion tests were performed in collaboration with Norwegian Defence Estates Agency at their facilities at Østøya, Norway.

A comprehensive numerical study has been performed, looking at the modeling of concrete and the application of blast loading. The compression test of the concrete cubes was modeled using the finite element software ABAQUS and the implemented CDP model for the material behavior. A sensitivity study was performed, investigating the effect of altering different parameters in the model, such as scaling the compression strength, modulus of elasticity, friction, mesh size, erosion criteria and configuration of the material model. To investigate the potential of numerical models in analyzing concrete structures exposed to blast loading, the pipes exposed to blast loading were modeled, with the experimental work acting as a reference. Further, different material parameters and mesh size was modified to examine the change in qualitative results. Lastly, CFD analyses in Europlexus were carried out to examine potential improvements in the description of the blast loading.

The most important discoveries of this study will be further discussed below.

Experimental work

In total 24 cubes were tested under compression. The concrete cubes showed some variation in compressive strength; the average compression strength was found to be 79.01 MPa. Three of the cubes were used for a DIC-analysis in an attempt to establish a stress-strain relationship for the concrete. DIC is not intended for brittle materials like concrete, and this became evident when doing the analyses. The DIC gave a good read-out of the strain up until the initiation of cracks, close to the maximum recorded force. The cracks in the test specimen distorted the mesh in the DIC-analyses severely, as a result giving spurious strain measurements. The stress-strain relationship was thus only constructed up until peak stress.

Blast test experiments were conducted on a total number of 18 pipes, 6 of each kind. The *BASAL Mufferør ig* were subjected to centrically placed C4 charges ranging in size from 10 g to 20 g. It was found that as the charge increased from 12 g to 14 g, the pipe went from experiencing a few cracks to complete fracture. This was in compliance with tests performed from another experimental series, which found that 13 g of C4 was required to produce through-thickness cracks [9]. As the charge size was further increased it was seen that the concrete pipes were shattered in increasingly smaller pieces.

Plain concrete *BASAL Falsrør ig* was subjected to charges between 50 and 150 g C4. A charge of 50 g C4 gave no visible damage to the pipe, but increasing the charge size to 65 g gave two distinct through-thickness cracks along the pipe's length, splitting the pipe in two halves. When the charge size was further increased, it was seen that the pipe got fractured in increasingly smaller pieces.

The reinforced *BASAL Falsrør ig* was exposed to charges varying from 150 g to 500 g C4. For the smallest charge of 150 g, the pipe suffered small exterior cracks extending from the center in the longitudinal direction, and in the circumferential direction at the center. As the charge size increased the pipe got increasingly more damaged. With 300 g and 400 g C4, pieces of concrete started to fall of from the outside of the pipe, cracks were also visible on the inside implying through-thickness cracks. Lastly, at 500 g the pipe got severely destructed with large fragments being scattered and the pipe wall was breached, exposing the rebar.

Lastly, in compliance with theory, there was seen to be a linear relationship between the charge size and the maximum pressure from the blast.

Numerical study - Cubes

The compression tests of the cubes were modeled and a parameter study was performed. A scaling approach of the CDP model was used to adjust the compression strength of the simulated concrete cube. In addition, the behavior of the material model under scaling was inquired into. It was found that with the J-L configuration, the stress-strain curve had some unexpected characteristics as it was scaled up, and did not resemble a typical stress-strain curve for concrete. However, if the E-modulus was altered, the stress-strain curve showed much more resemblance to the typical stress-strain curve that is known for concrete, especially in terms of the post-peak softening behavior. The E-modulus was seen to affect the compression strength as well. It was found that the theoretical compression strength was often smaller than the maximum engineering stress found from the simulations.

Furthermore, other parameters that had a notable influence on the model was the mesh size. Increasing the mesh size resulted in less post-peak softening and a generally stiffer behavior. Strains were also seen to be more concentrated as the mesh size decreased. The erosion criterion was also modified and compared against the basis model. With erosion activated, an excessive amount of elements were removed such that the cube was not able to withstand stresses after the peak stress, this was in contradiction to the experiments and the softening phase of the concrete was not captured.

A different calibration of the CDP model, by Labibzadeh et al. [56], was also tested and scaled; it showed great potential with smooth stress-strain curves similar to the characteristic stress-strain curve of concrete. Under extensive scaling it did however suffer from some fluctuations in the stress-strain curve and in the kinetic energy, but it is expected that adjusting the E-modulus would ameliorate this. It was observed that strains tended to localize more in the Lab configuration, compared to the J-L configuration. Increasing the E-modulus also made strains concentrate more.

Other parameters that were studied were the friction and the time scaling. Friction had little effect on the model unless the tangential friction coefficient was set close to zero. Since the compression test was quasi-static, the time period of the simulation was scaled. Naturally, if the time got overly scaled, large fluctuations appeared and additional energy was created.

Numerical study - Pipes

The plain concrete and reinforced *BASAL Falsrør ig* was chosen for a more extensive numerical study. For the plain concrete pipes the loading scenarios of 50 g, 100 g and 150 g C4 were investigated. With the reinforced pipes, it was chosen to focus on the loading scenarios of 150 g, 300 g and 500 g C4. In general, it was seen that the plain concrete pipes suffered from substantial erosion in the area in proximity of the charge. The erosion subroutine removed an exaggerated number of elements, thereby underestimating the capacity of the pipes. Strains were predominantly located in the central part of the pipe, and it was observed that the material configurations which had more strain localization also saw less erosion.

The reinforced pipes provided better qualitative results. Concrete is known to be quite unpredictable, whereas models for steel are well established and tested. When the pipes are subjected to an internal pressure, the concrete undergoes biaxial tension in the longitudinal and circumferential direction. Under tension, it is the steel that absorbs the majority of the stresses and thus becomes determining in the behavior when the pipe is reinforced. The reinforcement also seemed to act as a regularization, encouraging strain dissipation. Therefore, the numerical model was able to give a better qualitative representation of the experiments once reinforcements were added.

A sensitivity study on the pipes was also conducted to study the effect on qualitative behavior. Variations were made to the scaling of the material model, the erosion criteria, the mesh size and another calibration of the CDP model was also tried. Evidently, scaling the theoretical compression hardening and tension stiffness tables for the CDP model gave little effect, even more so for the reinforced pipes. Though when adjusting the E-modulus according to an empirical model notably less elements were eroded. Alterations to the erosion criteria were also made, and it was seen that as the erosion criteria was increased, the pipe behaved in a more ductile manner. Decreasing the mesh size gave a much better qualitative reproduction of cracks. From the physical tests, the cracks were generally quite small, often only a few millimeters in width. The erosion of smaller elements is therefore better able to reproduce these cracks and gives a higher level of detail. Especially good results were seen for the reinforced pipes with a mesh size of 5 mm. The cube compression tests showed that strains concentrate more as the mesh size decreases, giving a weaker concrete, but apparently less erosion overall. Lastly, another configuration of the CDP model was tested, which gave a theoretically higher tensile strength and more strain localization. Overall fewer elements were eroded, and the pipe suffered from less tensile damage by this configuration.

The blast loading was modeled using the CONWEP model which is implemented in ABAQUS. It is simple to use and calibrate, and it worked predominantly well. Though it was clear that it has its limitations. When comparing the pressure read-out from the CONWEP model to the pressure data from the experiments, it was clear that the CONWEP model was not able to give a sufficiently high pressure loading farther out from the center. The positive impulse of the loading was also considerably smaller.

Using Europlexus, Eulerian simulations were performed, in an effort to include effects such as reflections due to confinement. The pressure magnitude was still underestimated, but the shock wave propagation and pressure loading was better represented. Only in vicinity of the charge is the wall subjected to head-on loading. Furthermore, the maximum pressure was seen to decrease less over the length of the pipe, compared to the CONWEP model. Arrival times of the shock wave was also well predicted by this method.

8.2 Conclusion

This thesis has revolved around the consequences of an internal blast loading in an SFT. It was found that a reinforced concrete pipe, exposed to a centrically placed explosive charge, could withstand an explosion equivalent to a scaled distance of approximately $Z = 0.3$. The cross section proposed for the SFT has an inner diameter of 5.3 m. To achieve the same scaled distance it would require almost 5570 kg of C4, or equivalently 7800 kg of TNT. For comparison, the bomb detonated within the Executive Government District in Oslo is estimated to have been equivalent to somewhere in between 400 kg and 700 kg of TNT [16]. Thus, the SFT should be able to resist quite a significant blast. Moreover, the most severe damage to the pipes were mainly located in closeness to the blast origin, indicating that this is a local problem. This is something to bear in mind for future simulations of an SFT, only the region in proximity to the charge need to be assessed in detail.

Modeling concrete proved to be difficult. The CDP model shows potential, but when the material parameters in the model does not correspond to the concrete being modeled, it requires extensive adjustment to get a good agreement with physical behavior. With reinforcements, the qualitative behavior of the concrete was better replicated than without. The erosion subroutine utilized gave an exaggerated amount of erosion for the plain concrete pipes.

To accurately model a blast load in confined spaces it is recommended to use computational methods like CFD, rather than methods based on empirical models like the CONWEP model. Numerical methods could more accurately model the shock wave propagation and pressure distribution, though the magnitude of the pressure was underestimated. It could therefore be necessary to calibrate these models to get more accurate results.

Chapter 9

Further Work

The work undergone in this thesis has investigated a few ways to model concrete pipes subjected to internal blast loading. It is a subject that can be further explored in many ways, and there are room for improvements and more thorough study in certain areas. In the following a few proposals to further work and improvements will be made.

Investigate the possibilities of a statistical model to more accurately describe concrete behavior. Hillestad and Pettersen [6] employed a mesoscale model to more accurately describe the statistical behavior of concrete. They got very promising results and the model could capture intricate crack patterns. Using a mesoscale approach to the pipes was considered for this thesis, but due to time limitations it was not prioritized. The effect it would have to the pipes could be debatable however; the geometry of the pipes is quite large compared to the aggregate size, thus the local strength variations exist on a small scale compared to the size scale of the pipe. The qualitative assessment of the pipe is performed at large scale, thus small local variations in the concrete will tend to be smeared out. For instance, in the experiments, where some charge sizes were repeated and the response and failure mode of the pipe was approximately the same. Additionally, as the aggregates in the pipe had a maximum size of 8 mm, it would require a very fine mesh size to be able to capture the aggregates. Nevertheless, it could still be interesting to implement a mesoscale model or similar to be able to definitely say if there is an effect or not.

Include strain rate effects in the concrete. Concrete subjected to dynamic loading tends to see an increase in ultimate stress and elastic modulus. The plain concrete pipes saw predominantly excessive erosion; it could be investigated if the inclusion of strain-rate effects would aid in increasing the capacity of the concrete. Hillestad and Pettersen looked into strain-rate effects in LS-DYNA; it gave a considerably stronger concrete and actually under-predicted the displacement in the concrete slabs. At high pressure blast the correlation between experimental and simulated crack patterns improved. Therefore, it would be interesting to see if the same effect would be present for the pipes.

Perform a full FSI simulation on the pipes. It would be of relevance to include effects such as reflections due to confinement in the application of the loading to the pipe. One possibility is to do an uncoupled simulation where the loading is calculated in an Eulerian analysis first, and then apply the loading in a Lagrangian analysis. Another option, and probably the best, is to do a fully coupled FSI simulation, this would also include effects such as pressure leakage through the cracks as the pipe shatters. Kristoffersen [9] had success with this using Europlexus. In an FSI simulation using the JWL EOS, it could also be of interest to scale the charge size to get analogous loading to the experiments.

Create a more advanced erosion criterion. The erosion criterion used in ABAQUS is a strain based criteria developed by Hillestad and Pettersen [6]. For the plain concrete pipes, it was seen that increasing the critical strain did reduce the amount eroded elements, yet the capacity of the pipes was still underestimated. For the simulations in general, too much erosion occurred. It is therefore suggested, also by Hillestad and Pettersen, to create a more sophisticated criterion where multiple parameters are taken into account.

Do material tests of the rebar steel. The material model used for the rebar steel was a simple standard Johnson-Cook plasticity model which was not calibrated. For a more accurate description of the steel behavior it could be considered to calibrate the material model after experimental tests.

Explore other concrete models. Other concrete models, such as the K&C model in LS-DYNA or DPDC model in Europlexus, could be further explored to investigate potential improvements in the description of concrete behavior.

References

[1] Norwegian Ministry of Transport and Communications. *National Transport Plan 2018-2029*. Report to the Storting. Meld.St.33. 2016-2017.

[2] Statens Vegvesen. *The E39 Coastal Highway Route*. URL: `http://www.vegvesen.no/Vegprosjekter/ferjefriE39/English` (visited on 06/06/2018).

[3] Reinertsen, Dr. techn. Olav Olsen. *Feasibility study for crossing Sognefjorden - Submerged Floating Tunnel*. Document no. 11744-ROO-R-001.

[4] Teknisk Ukeblad. *Voldsom brann etter eksplosjon i tunnel i Bremanger*. URL: `https://www.tu.no/artikler/voldsom-brann-etter-eksplosjon-i-tunnel-i-bremanger/197007` (visited on 06/06/2018).

[5] S. R. Haug and K. Osnes. *Submerged floating tunnels subjected to internal blast loading*. MA thesis. NTNU, 2015.

[6] E. Hillestad and J. E. Pettersen. *Experimental and Numerical Studies of Plain and Reinforced Concrete Plates Subjected to Blast Loading*. MA thesis. NTNU, 2016.

[7] IMPETUS Afea AS. *IMPETUS Afea Solver Command manual*. Version 4.0. 2018. URL: `https://www.impetus-afea.com/support/manual/` (visited on 06/07/2018).

[8] Livermore Software Technology Corporation. *LS-DYNA Manuals*. 2018. URL: `https://www.dynasupport.com/manuals` (visited on 06/07/2018).

[9] M. Kristoffersen, K. O. Hauge, G. Valsamos, and T. Børvik. *Blast loading of concrete pipes using spherical centrically placed C-4charges*. In: *Proceedings of 12th International DYMAT Conference* (9–14).

[10] European Commision Joint Research Centre. *Europlexus User's Manual*. URL: `http://europlexus.jrc.ec.europa.eu/public/manual\_pdf/manual.pdf` (visited on 06/06/2018).

[11] M. Kristoffersen, A. Minoretti, and T. Børvik. *Submerged floating tunnels subjected to internal blast loading*. In: *Proceedings of 7th Transport Research Arena TRA 2018, Vienna, Austria* (2018).

[12] M. Kristoffersen, J. Eide, V. Aune, and T. Børvik. *Experimental and numerical study on blast loading of normal strength concrete slabs.* In: 7491 (2017), pp. 1–26.

[13] R. Tiwari, T. Chakraborty, and V. Matsagar. *Dynamic Analysis of Tunnel in Soil Subjected to Internal Blast Loading.* In: *Geotech. Geol. Eng.* 35.4 (2017), pp. 1491–1512. ISSN: 15731529. DOI: `10.1007/s10706-017-0189-9`.

[14] B. Burgan, A. Chen, J.-W. Choi, and Y. Ryu. *The use of coupled and uncoupled analysis techniques in the assessment of blast wall response to explosions.* In: *Proc. Int. Conf. Offshore Mech. Arct. Eng. - OMAE* 3.V003T02A022 (2016). DOI: `10.1115/OMAE2016-55100`.

[15] D. O. Dusenberry, ed. *Handbook of Blast-Resistant Design of Buildings.* John Wiley & Sons, Inc., 2010. ISBN: 9780470170540.

[16] V. Aune, T. Børvik, and M. Langseth. *Lecture Notes in TKT4128 Impact Mechanics : An Introduction to Blast Mechancis.* SIMLab, Department of Structural Engineering, NTNU. Trondheim, Norway, 2016.

[17] Atomic Heritage Foundation. *Science Behind the Atom Bomb.* URL: `https://www.atomicheritage.org/history/science-behind-atom-bomb` (visited on 06/06/2018).

[18] V. Aune. *Behaviour and modelling of flexible structures subjected to blast loading.* PhD thesis. NTNU, 2017.

[19] J. L. Meriam and L. G. Kragie. *Engineering Mechanics Dynamics.* 7th ed. Vol. 2. John Wiley & Sons, Inc., 2012.

[20] G. Randers-Pehrson and K. A. Bannister. *Airblast Loading Model for DYNA2D and DYNA3D.* Tech. rep. Army Research Laboratory, 1997.

[21] V. Feldgun, Y. Karinski, I. Edri, D. Tsemakh, and D. Yankelevsky. *On Blast Pressure Analysis Due to a Partially Confined Explosion: II. Numerical Studies.* In: *International Journal of Protective Structures* 3.1 (2012), pp. 61–79. DOI: `10.1260/2041-4196.3.1.61`. URL: `https://doi.org/10.1260/2041-4196.3.1.61`.

[22] I. Edri, Z. Savir, V. Feldgun, Y. Karinski, and D. Yankelevsky. *On Blast Pressure Analysis Due to a Partially Confined Explosion: I. Experimental Studies.* In: *International Journal of Protective Structures* 2.1 (2011), pp. 1–20. DOI: `10.1260/2041-4196.2.1.1`. URL: `https://doi.org/10.1260/2041-4196.2.1.1`.

[23] I. Edri, V Feldgun, Y Karinski, and D. Yankelevsky. *On Blast Pressure Analysis Due to a Partially Confined Explosion: III. Afterburning Effect.* In: 3 (Sept. 2012), pp. 311–331.

[24] C. N. Kingery and G. Bulmash. *Airblast parameters from TNT Spherical Air Burst and Hemispherical Surface Burst.* Tech. rep. Aberdeen Proving Ground, Maryland: Defence Technical Information Center, Ballistic Research Laboratory, 1984.

[25] US Army Corp of Engineers (USACE). *Structures to resist the effects of accidental explosions.* Tech. rep. UFC 3-340-02. US Department of Defense, Washington DC, 2008. Supersedes TM5-1300, 1990.

[26] D. Hyde. *ConWep – Application of TM 5-855-1.* Vicksburg, MS, USA: Structural Mechanics Division, Structures Laboratory, USACE Waterways Experiment Station, 1992.

[27] Dassault Systémes. *Abaqus Analysis User's Guide.* URL: `http://130.149.89.49:2080/v2016/books/usb/default.htm` (visited on 06/06/2018).

[28] T. Krauthammer. *Modern Protective Structures.* CRC Press, Taylor & Francis Group, 2001.

[29] B. M. Dobratz and P. C. Crawford. *LLNL Explosives Handbook, Properties of Chemical Explosives and Explosive Simulants.* 1985.

[30] J. H. Spurk and N. Aksel. *Fluid Mechanics.* 2nd ed. Springer, 2008. ISBN: ISBN 978-3-540-73536-6.

[31] Wikiversity. *Nonlinear finite elements/Lagrangian and Eulerian descriptions.* 2017. URL: `https://en.wikiversity.org/wiki/Nonlinear_finite_elements/Lagrangian_and_Eulerian_descriptions` (visited on 06/06/2018).

[32] O. S. Hopperstad and T. Børvik. *Lecture Notes in TKT4128 Impact Mechanics: Modelling of plasticity and failure with explicit finite element methods.* SIMLab, Department of Structural Engineering, NTNU. Trondheim, Norway, 2017.

[33] J. Blazek. *Computational Fluid Dynamics. Principles and Applications.* Elsevier, 2005. ISBN: ISBN: 978-0-08-099995-1.

[34] O. S. Hopperstad and T. Børvik. *Materials Mechanics.* SIMLab, Department of Structural Engineering, NTNU. Trondheim, Norway, 2017.

[35] Basal. *Rør- og Kumsystemer av betong.* URL: `http://www.basal.no/ror/` (visited on 06/06/2018).

[36] W.-F. Chen. *Plasticity in Reinforced Concrete.* J. Ross Publishing Classics. J. Ross Publishing, 2007. ISBN: 9781932159745. URL: `http://search.ebscohost.com/login.aspx?direct=true&db=e230xww&AN=225355&site=ehost-live`.

[37] P. K. Mehta and P. J. M. Monteiro. *Concrete. Microstructure, Properties and Materials.* McGraw-Hill, 2006. DOI: `DOI:10.1036/0071462899`.

[38] A. Neville. *Concrete: Neville's Insights and Issues.* Thomas Telford Publishing, 2006. DOI: `10.1680/cniai.34686`. URL: `https://www.icevirtuallibrary.com/doi/abs/10.1680/cniai.34686`.

[39] J. van Mier. *Concrete Fracture.* Boca Raton: CRC Press, 2012.

[40] X. Q. Zhou and H. Hao. *Modelling of compressive behaviour of concrete-like materials at high strain rate.* In: *Int. J. Solids Struct.* 45.17 (2008), pp. 4648–4661. ISSN: 00207683. DOI: `10.1016/j.ijsolstr.2008.04.002`.

[41] D. M. Cotsovos and M. N. Pavlović. *Numerical investigation of concrete subjected to high rates of uniaxial tensile loading.* In: *Int. J. Impact Eng.* 35.5 (2008), pp. 319–335. ISSN: 0734743X. DOI: `10.1016/j.ijimpeng.2007.03.006`.

[42] D. Grote, S. Park, and M. Zhou. *Dynamic behavior of concrete at high strain rates and pressures: I. experimental characterization.* In: *Int. J. Impact Eng.* 25.9 (2001), pp. 869–886. ISSN: 0734743X. DOI: `10.1016/S0734-743X(01)00020-3`.

[43] M. Pajak. *The influence of the strain rate on the strength of concrete taking into account the experimental techniques.* In: *Archit. Civ. Eng. Environ.* (2011), pp. 77–86. ISSN: 1947-5748. DOI: `10.1615/NanomechanicsSciTechnolIntJ.v2.i3.40`. URL: `https://www.researchgate.net/publication/257610043`.

[44] K. S. Kandil, M. T. Nemir, E. A. Ellobody, and R. I. Shahin. *Implicit and Explicit Analysis of the Response of Blast Loaded Reinforced Concrete Slabs.* In: *World J. Eng. Technol.* 02.03 (2014), pp. 211–221. ISSN: 2331-4222. DOI: `10.4236/wjet.2014.23023`. URL: `http://www.scirp.org/journal/PaperDownload.aspx?DOI=10.4236/wjet.2014.23023`.

[45] Dassault Systémes. *Abaqus Theory Guide.* URL: `http://130.149.89.49:2080/v2016/books/stm/default.htm` (visited on 06/06/2018).

[46] J. Lubliner, J. Oliver, S. Oller, and E. Oñate. *A Plastic-Damage Model for Concrete.* In: *International Journal of Solids and Structures* 25.3 (1989), 229–326.

[47] J. Lee and G. L. Fenves. *Plastic-Damage Model for Cyclic Loading of Concrete Structures.* In: *Journal of Engineering Mechanics* 124.8 (1998), 892–900.

[48] The Editors of Encyclopaedia Britannica. *Reinforced concrete.* Encyclopædia Britannica Inc. 2014. URL: `https://www.britannica.com/technology/reinforced-concrete` (visited on 06/06/2018).

[49] E. Fagerholt. *eCorr v4.0 Documentation.* URL: `http://www.ntnu.edu/kt/ecorr` (visited on 06/06/2018).

[50] Instron. *5980 Series Universal Testing Systems up to 600 kN Force Capacity.* URL: `http://www.instron.us/en-us/products/testing-systems/universal-testing-systems/electromechanical/5900/5980-floor-model` (visited on 06/06/2018).

[51] Basal. *Basal Produktkatalog.* URL: `http://www.basal.no/Produkter/177/produktkatalog` (visited on 06/06/2018).

[52] Jankowiak, Tomasz and Lodygowski, Tomasz. *Identification of parameters of Concrete Damage Plasticity constitutive model.* In: *Foundations of civil and environmental engineering* 6 (2005).

[53] Dassault Systémes. *Abaqus Scripting User's Guide.* URL: `http://130.149.89.49:2080/v2016/books/cmd/default.htm` (visited on 06/06/2018).

[54] Python Software Foundation. *Documentation.* 2018. URL: `https://www.python.org/doc/` (visited on 06/08/2018).

[55] Civiltoday.com. *Modulus of Elasticity of Concrete - Civil Engineering.* URL: `https://civiltoday.com/civil-engineering-materials/concrete/84-modulus-of-elasticity-of-concrete` (visited on 06/06/2018).

[56] M. Labibzadeh, M. Zakeri, and A. Shoaib. *A new method for CDP input parameter identification of the ABAQUS software guaranteeing uniqueness and precision.* In: *Int. J. Struct. Integr.* 8.2 (2017). ISSN: 17579872. DOI: `10.1108/IJSI-03-2016-0010`.

[57] Standard Norge. *NS-EN 206: Betong. Spesifikasjon, egenskaper, framstilling og ansvar.*

[58] ISO. *ISO 22965-1: Concrete. Part 1 - Methods of specifying and guidance for the specifier.* 2007.

[59] Wikipedia. *TNT equivalent.* 2018. URL: `https://en.wikipedia.org/wiki/TNT_equivalent` (visited on 06/06/2018).

[60] T Jankowiak and T Lodygowski. *Identification of parameters of concrete damage plasticity constitutive model.* In: *Found. Civ. Environ. . . .* 6 (2005), pp. 53–69. ISSN: 1642-9303. DOI: `10.3390/app6090245`. URL: `http://www.ikb.poznan.pl/fcee/2005.06/full/fcee{\_}2005-06{\_}053-069{\_}identification{\_}of{\_}parameters{\_}of{\_}concrete.pdf`.

[61] H. M. Granum and L. M. Løken. *Experimental and Numerical Study on Perforated Steel Plates Subjected to Blast Loading.* MA thesis. NTNU, 2016.

Appendices

Appendix A

Concrete Data

LOE Rorprodukter
NO-Trondheim

02.11.2017
10:22:36

Auftragsprotokoll 51 (07.09.2017)
Charge 1

Dato:	07.09.2017	**Tid:**	11:48:54	**Oppdragsnummer::**	51
Bruker:	LASSE UTAKER	**Betontemperatur:**	12,6 °C	**Mengde (Total:):**	1,42 m³
Reseptsort:	Basal IG MAX 20-25 Cryso	**Dato:**	07.09.2017	**Tid:**	11:54:10

Reseptdata

Dato:	07.09.2017	**Tid:**	11:48:54
Oppdragsnummer::	51	**Ordrenr:**	1
Starttid::	11:48:54	**Tømmeposisjon (Navn):**	Masterflex
Mischmenge (Prozent):	95,0 %	**Mischmenge:**	1,42 m³
Navn:	Masterflex	**Blander:**	2

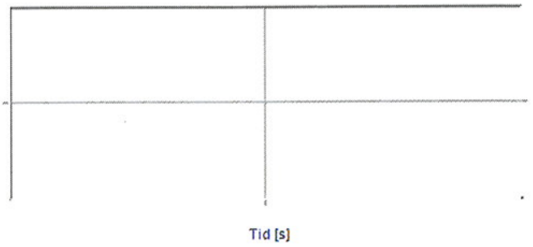

WDG Daten

Mischmenge (Prozent):	95,0 %	**v/c faktor:**	0,3700
Luftinnhold:	0,00	**Blandetid (Total:):**	80,2 s
Ekstra vann::	103,5l	**Vann (Dosert:):**	103,0l
Vann (Manuell):	0,0l	**Vannkorrektur (Er):**	0,0l
FuktStein (Summe):	118,9l	**Sementvekt (Ohne Füller):**	592,0 kg
v/c faktor (Kalkulert):	0,3692	**v/c faktor (Ende Trockenmischzeit):**	0,1918
v/c faktor (Ende Nassmischzeit):	0,4089	**v/c faktor (Ende Nassmischzeit):**	

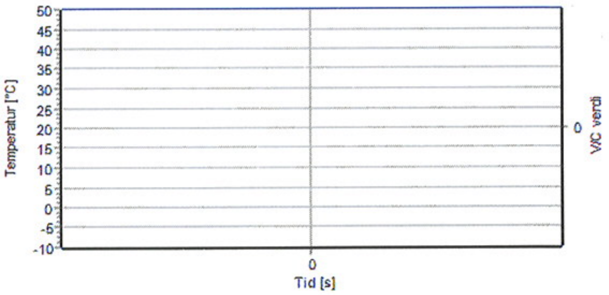

	Dato:	**Mpa:**
1 døgns:	8-9	38,2
7 døgns:	14-9	64,1
28 døgns:	5-10	83,3

Diverse målte verdier

Temperatur:	**Luftinnhold:**	**Densitet:**
°C	%	gr/dm3

LOE Rorprodukter
NO-Trondheim

30.10.2017
13:05:52

Resepter

Basal IG MAX 20-25 Cryso

Reseptsort	Basal IG MAX 20-25 Cryso	Artikkelnummer:	20
		Navn	Masterflex
Fasthetsklasse		Trykkfasthet:	
Eksponeringskl.		Luftinnhold	0,00
v/c faktor	0,3700	Informasjon	
Zeitvorgabe (Navn)	Tørrbetong		

Aggregat

Artikkelnummer:	Unternummer	Dosierposition	Mengde
1003 (Hanset 0-8)	1	2	550kg
1005 (Hanset 0-8)	1	3	550kg
1006 (Eidsmo 0-8)	1	8	250kg
1002 (Vassfjell 4-8)	1	9	610kg

Sement

Artikkelnummer:	Unternummer	Dosierposition	Mengde
2001 (FA)	1	1	400kg
2003 (Silica)	1	2	18kg

Tilsetningsstoff

Artikkelnummer:	Unternummer	Dosierposition	Mengde
3003 (Premia 204)	1	1	2,30kg
3005 (Air R2)	1	2	0,50kg

Vann

Artikkelnummer:	Unternummer	Dosierposition	Mengde
4001 (Kaldt vann)	1	1	60kg
4003 (Direkte vann)	1	2	94kg

Tider Blander 1

Tider Blander 2

Taktende Dosiereinrichtung Blander 1

Taktende Dosiereinrichtung Blander 2

Loe Rørprodukter Nord AS *På lag med brukerne*	**VANNABSORPSJON**	Blankett nr.:

Produkt: Basal 200x1500 ig

PRØVE 1	PRØVE 2
Vekt etter neddykking i vatn m_1: 1612	Vekt etter neddykking i vatn m_1: 1603
Vekt etter 5 døgn i tørkeskap m_2: 1551	Vekt etter 5 døgn i tørkeskap m_2: 1545
Masseøkning m_1-m_2: 61	Masseøkning m_1-m_2: 58
Absorpsjon $A_w = 100(m_1-m_2)/m_2$ 3.93%	Absorpsjon $A_w = 100(m_1-m_2)/m_2$ 3.75%

Gjennomsnitt av prøve 1 og 2 er:

Kommentar:
Lagt i vann: 1/11-17. Taes ut 2/11-17
Ut fra ovn 7/11-17

dc

Dato: 9/11-17

Utført av: Johan Faranoim

KVALITETSSYSTEM

Appendix B

Pipe Information

BASAL mufferør ig

Mål (mm)				Overdekn. min/maks. (m)	Maks. tillatt avvinkling (mm/m)	Vekt ca. kg
DN	*l*	t	Dm			
150	500 1000	33	284	0,5-10,0	63	35 55
200	500 1500	37 41	353	0,5-8,0	49	50 140
250	500 1500 2000	42 45 48	425	0,5-7,0	54	70 190 250
300	500 2000	45 53	481	0,5-6,0	45	80 340
400	1000 2000	50 63	590	0,5-5,0	36	240 500

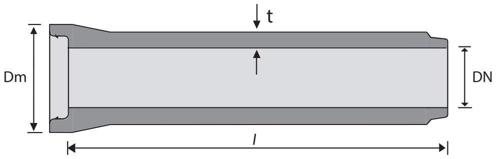

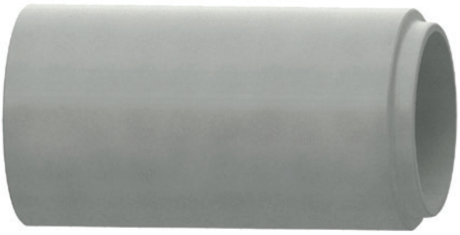

BASAL falsrør ig

Mål (mm)				Overdekn. standardrør min-maks. (m)	Maks. tillatt avvinkling (mm/m)***	Vekt ca. kg
DN	*l*	t	OD			
300	1000 2000 2250	90	480	0,5-12,0* $^{1)}$	45	275 550 620
400	1000 2000 2250	85	570	0,5-7,0* $^{1)}$	36	330 650 730
500	1000 2000 2250	90	680	0,5-6,0*	29	420 840 940
600	1000 2000 2250	94	788	0,5-4,0*/**	24	520 1030 1160
800	1000 2000 2250	110	1020	0,5- 4,0 **	23	790 1580 1770
1000	1000 2000 2250	125	1250	0,5- 4,0 **	18	1110 2210 2490
1200	1000 2000 2250	136	1472	0,5- 4,0 **	16	1430 2860 3210
1400	1000 2000 2250	156	1712	0,5- 4,0 **	14	1910 3820 4290
1600	2000 2250	176	1952	0,5- 3,0 **	15	5000 5500
1800	2000	200	2200	0,5- 3,0 **	13	6290
2000	1500 2000	215	2430	0,5- 3,0 **	12	5610 7450
2400	1500	250	2900	0,5- 3,0 **	17	7680
3000	1750	320	3640	På forespørsel	14	14400

*Uarmert. Rør med større overdekning må bestilles spesielt
** Ønskes større overdekning må dette oppgis ved bestilling. Basal har dimensjonert alle rør for opptil 10 m. overdekning, ta kontakt for større overdeknnger.
*** Oppgitt avvinkling er 2/3 av maks. avvinkling.
Rør med overdekning som angitt i tabell er normalt lagervare.
$^{1)}$ Ved avkjørsler kan minimum overdekning reduseres til 0,2 m.
Omfylling må utføres med pukk 8-12 og komprimeres.

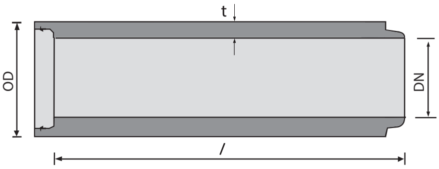

Appendix C

Material Parameters

C.1 CDP model: Jankowiak and Lodygowski

Table C.1 – *Concrete elasticity and CDP parameters.*

E [MPa]	ν [−]	ρ [t/mm^3]	ψ [−]	ϵ [−]	f [−]	K_c [−]
19700.0	0.19	2.4316×10^{-9}	38°	1.0	1.12	0.666

Table C.2 – *Compression hardening and damage data.*

Inelastic strain [−]	Damage [−]	Stress [MPa]
0.0000000000	0.0000000000	15.0000000000
0.0000747307	0.0000000000	20.1978040000
0.0000988479	0.0000000000	30.0006090000
0.0001541230	0.0000000000	40.3037810000
0.0007615380	0.0000000000	50.0076920000
0.0025575590	0.1954020000	40.2360900000
0.0056754310	0.5963820000	20.2360900000
0.0117331190	0.8948650000	5.2575570000

Table C.3 – *Tensile stiffening and damage data.*

Cracking strain [−]	Damage [−]	Stress [MPa]
0.0000000000	0.0000000000	1.9989300000
0.0000333300	0.0000000000	2.8420000000
0.0001604270	0.4064110000	1.8698100000
0.0002797630	0.6963800000	0.8627230000
0.0006845930	0.9203890000	0.2262540000
0.0010867300	0.9800930000	0.0565760000

C.2 CDP model: Labibzadeh et al.

Table C.4 – *Concrete elasticity and CDP parameters.*

E [MPa]	ν [–]	ρ [t/mm^3]	ψ [–]	ϵ [–]	f [–]	K_c [–]
33000.0	0.18	2.4316×10^{-9}	35°	0.1	1.12	0.67

Table C.5 – *Compression hardening data*

Inel. strain [–]	Stress [MPa]	Inel. strain [–]	Stress [MPa]	Inel. strain [–]	Stress [MPa]
0.0000	9.2110	0.0030	34.4310	0.0060	22.2160
0.0001	12.2770	0.0031	33.9850	0.0062	21.6140
0.0002	15.2240	0.0032	33.5300	0.0064	21.0380
0.0003	18.0270	0.0033	33.0690	0.0066	20.4850
0.0004	20.6630	0.0034	32.6050	0.0068	19.9580
0.0005	23.1120	0.0035	32.1380	0.0070	19.4520
0.0006	25.3620	0.0036	31.6720	0.0072	18.9680
0.0007	27.4060	0.0037	31.2070	0.0074	18.5040
0.0008	29.2380	0.0038	30.7450	0.0076	18.0590
0.0009	30.8600	0.0039	30.2860	0.0078	17.6320
0.0010	32.2760	0.0040	29.8330	0.0080	17.2230
0.0011	33.4930	0.0041	29.3840	0.0082	16.8290
0.0012	34.5220	0.0042	28.9410	0.0084	16.4520
0.0013	35.3740	0.0043	28.5050	0.0086	16.0890
0.0014	36.0610	0.0044	28.0750	0.0088	15.7400
0.0015	36.5970	0.0045	27.6520	0.0090	15.4050
0.0016	36.9950	0.0046	27.2370	0.0092	15.0820
0.0017	37.2700	0.0047	26.8290	0.0094	14.7700
0.0018	37.4330	0.0048	26.4290	0.0096	14.4710

0.0019	37.4980	0.0049	26.0360	0.0098	14.1820
0.0020	37.4760	0.0050	25.6510	0.0100	13.9040
0.0021	37.3770	0.0051	25.2740	0.0120	11.5860
0.0022	37.2130	0.0052	24.9050	0.0140	9.8930
0.0023	36.9910	0.0053	24.5430	0.0160	8.6100
0.0024	36.7200	0.0054	24.1880	0.0180	7.6070
0.0025	36.4080	0.0055	23.8420	0.0200	6.8030
0.0026	36.0610	0.0056	23.5020		
0.0027	35.6850	0.0057	23.1700		
0.0028	35.2850	0.0058	22.8450		
0.0029	34.8650	0.0059	22.5270		

Table C.6 – *Compression damage table.*

Inel. strain [−]	Damage [−]
0.000	0.000
0.003	0.080
0.004	0.200
0.005	0.310
0.006	0.400
0.007	0.480
0.008	0.540
0.009	0.580
0.010	0.600
0.011	0.600
0.012	0.600

Table C.7 – *Tensile damage and tensile stress table.*

Cracking strain [−]	Damage [−]	Stress [MPa]
0.0000000	0.0000000	3.5000000
0.0000224	0.1000000	3.1500000
0.0002690	0.3000000	2.4500000
0.0004480	0.5000000	1.7500000
0.0006280	0.7000000	1.0500000
0.0008070	0.9000000	0.3500000

C.3 Johnson-Cook

Table C.8 – *Material parameters for the Johnson-Cook constitutive model used for steel.*

E [MPa]	ν [−]	ρ [t/mm^3]	A [MPa]	B [MPa]	n [−]	m [−]	T_m [K]	T_0 [K]
200000.0	0.30	7.8×10^{-9}	348.0	566.0	0.044	0.0	15000.0	10000.0

Appendix D

Experimental

D.1 Overview of experimental tests

Table D.1 – *Full results from the experimental concrete cube tests. The average force and stress for the whole table is given at the bottom.*

	Cube 1		*Cube 27*		*Cube 40*	
Part	F [kN]	f_c' [MPa]	F [kN]	f_c' [MPa]	F [kN]	f_c' [MPa]
1	205.11	83.35	203.70	82.47	197.56	84.75
2	181.42	82.09	183.09	78.84	171.60	77.68
3	213.22	83.44	208.73	82.35	165.45	73.07
4	193.98	81.85	202.32	87.47	137.62	58.21
5	180.60	76.35	191.52	81.45	201.21	85.22
6	171.29	77.38	191.92	85.60	188.82	84.22
7	173.08	77.86	175.89	79.29	159.66	73.21
8	164.90	70.61	183.73	78.81	161.67	68.11
	Average F [kN]			*Average* f_c' [MPa]		
	183.67			79.81		

Table D.2 – *Overview of experimental tests conducted in March 2018.*

Test nr	*ID*	*Pipe*	*Mass C4*	*Failure mode*
1	XVII	Small - PCC	20.0 g	Fragmentation
2	XVIII	Small - PCC	10.0 g	No failure
3	XIX	Small - PCC	12.0 g	Cracking
4	XX	Small - PCC	14.0 g	Fragmentation
5	XXI	Small - PCC	16.0 g	Fragmentation
6	XXII	Small - PCC	18.0 g	Fragmentation
7	I	Large - PCC	150.0 g	Fragmentation
8	II	Large - Re	150.0 g	Cracking
9	III	Large - Re	200.0 g	Cracking
10	IV	Large - Re	300.0 g	Cracking and spalling/scabbing
11	V	Large - PCC	100.0 g	Fragmentation
12	VI	Large - PCC	50.0 g	No failure
13	VII	Large - PCC	75.0 g	Fragmentation
14	VIII	Large - PCC	75.0 g	Fragmentation
15	IX	Large - Re	400.0 g	Cracking and spalling/scabbing
16	X	Large - PCC	65.0 g	Cracking
17	XI	Large - Re	500.0 g	Cracking and fragmentation
18	XII	Large - Re	400.0 g	Cracking and spalling/scabbing

D.2 Pressure measurements

D.2.1 Small pipes

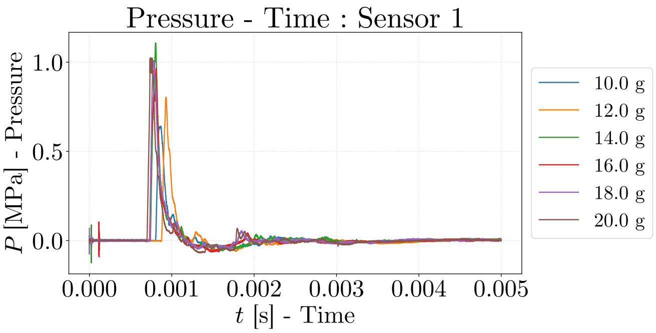

(a) *Sensor 1.*

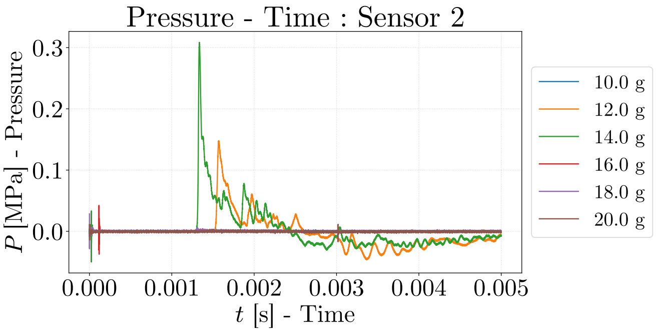

(b) *Sensor 2.*

D.2.2 Large pipes - PCC

D.2.3 Large pipes - Reinforced

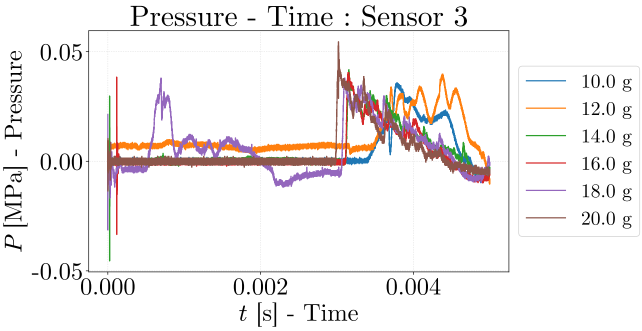

(c) *Sensor 3.*

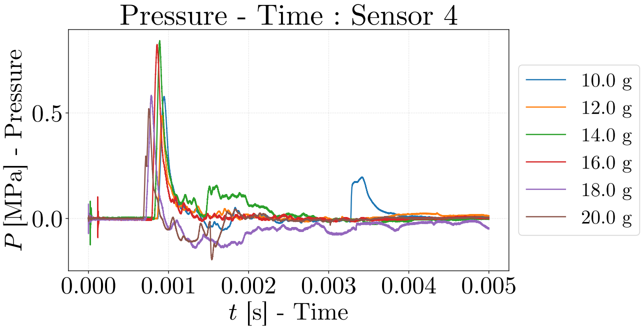

(d) *Sensor 4.*

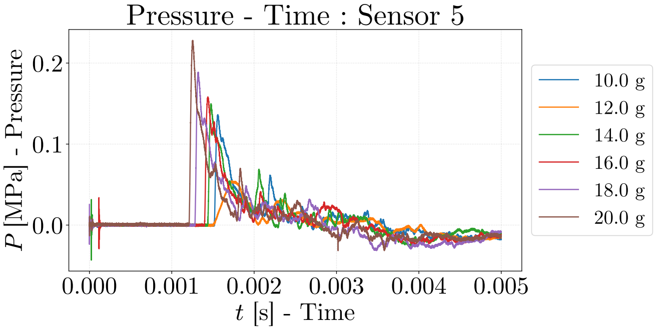

(e) *Sensor 5.*

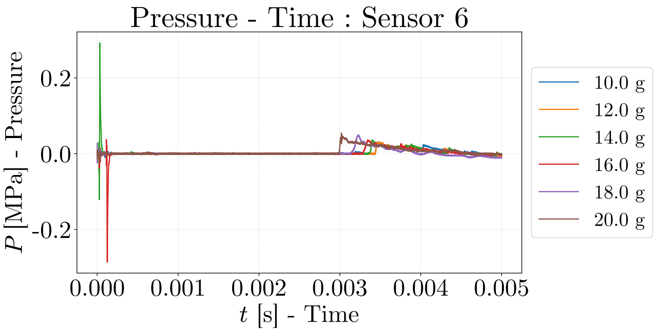

(f) *Sensor 6.*

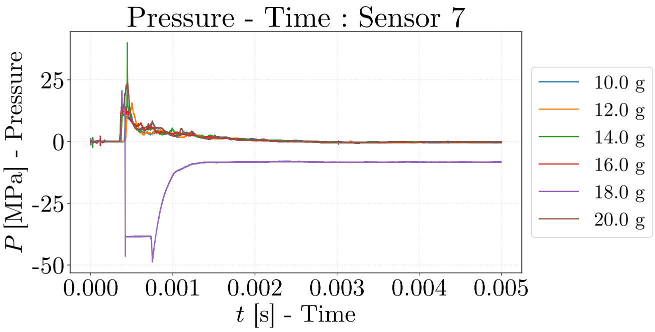

(g) *Sensor 7.*

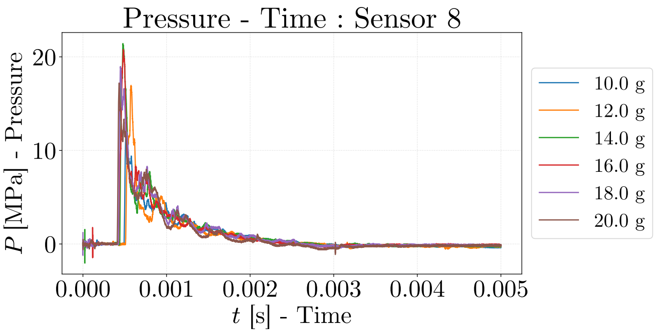

(h) *Sensor 8.*

Figure D.1 – *Pressure measurements from tests on BASAL Mufferør ig.*

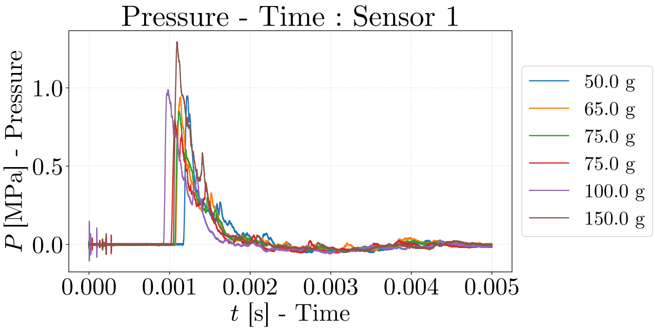

(a) *Sensor 1.*

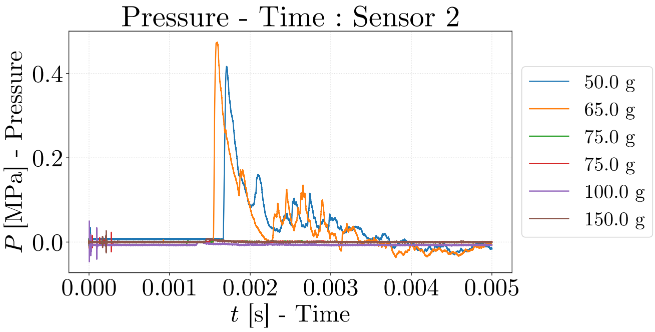

(b) *Sensor 2.*

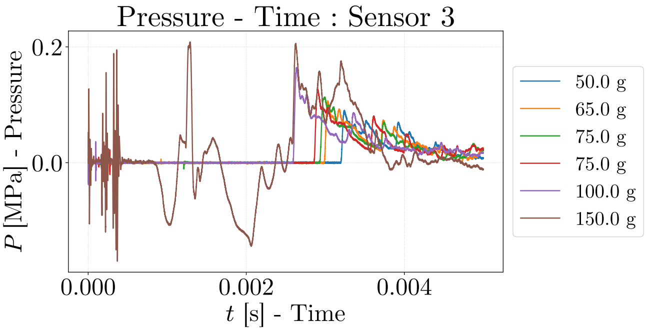

(c) *Sensor 3.*

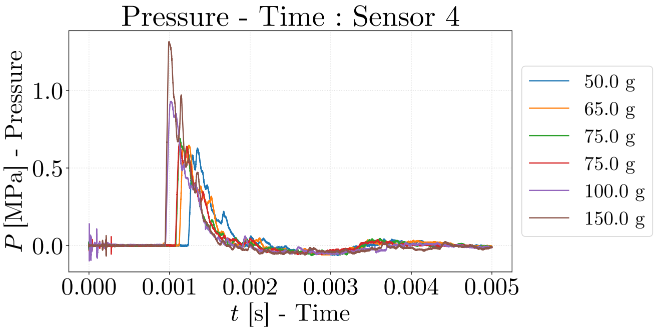

(d) *Sensor 4.*

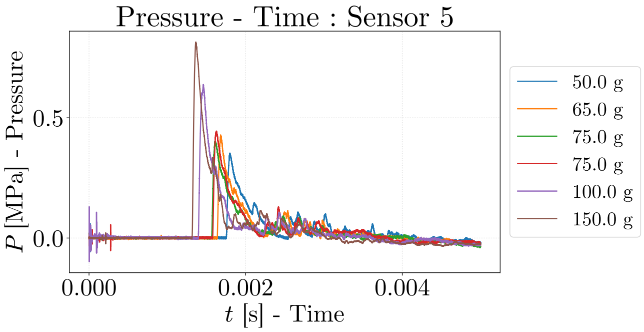

(e) *Sensor 5.*

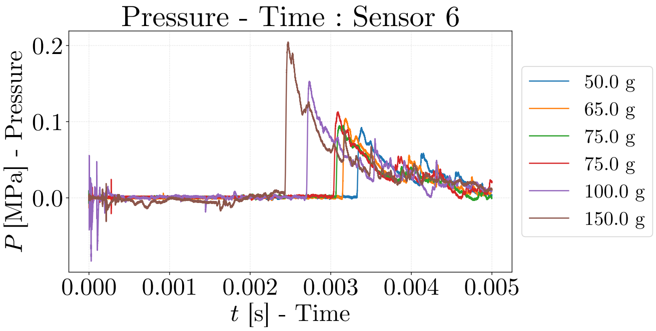

(f) *Sensor 6.*

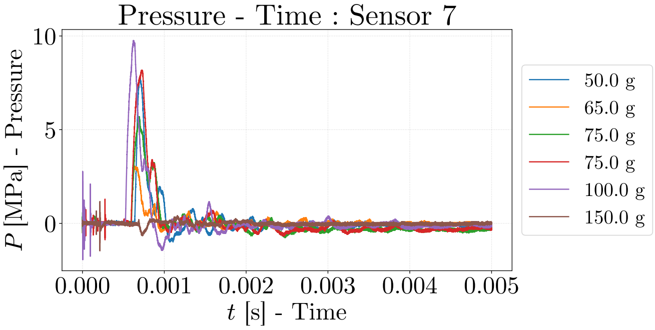

(g) *Sensor 7.*

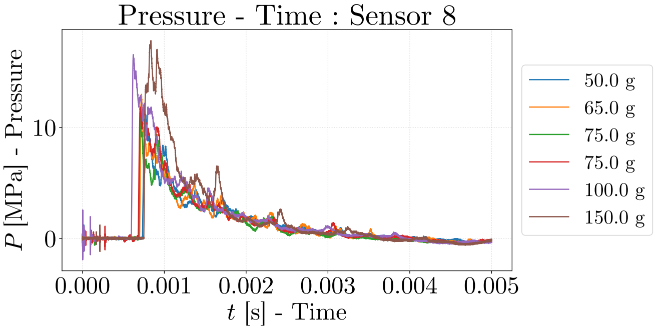

(h) *Sensor 8.*

Figure D.2 – *Pressure measurements from tests on plain concrete BASAL Falsrør ig.*

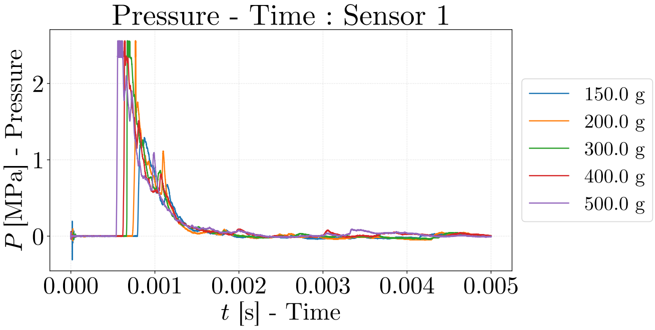

(a) *Sensor 1.*

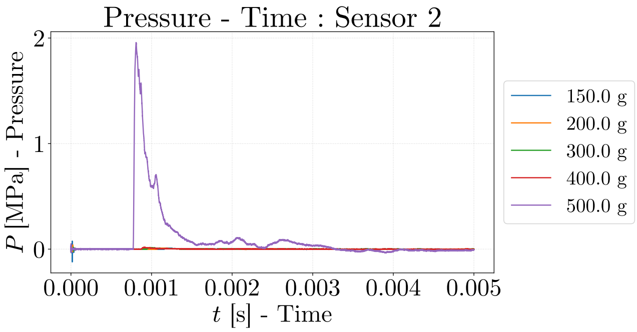

(b) *Sensor 2.*

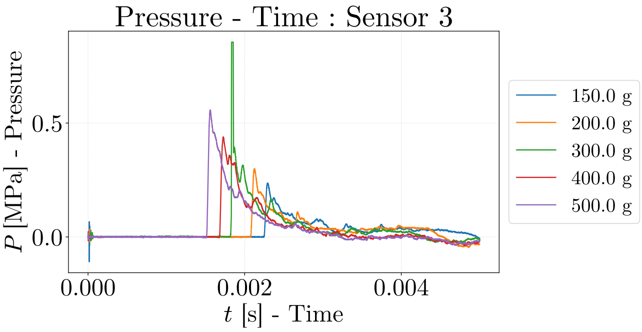

(c) *Sensor 3.*

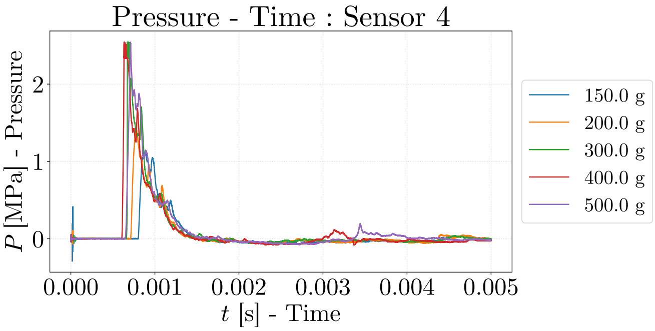

(d) *Sensor 4.*

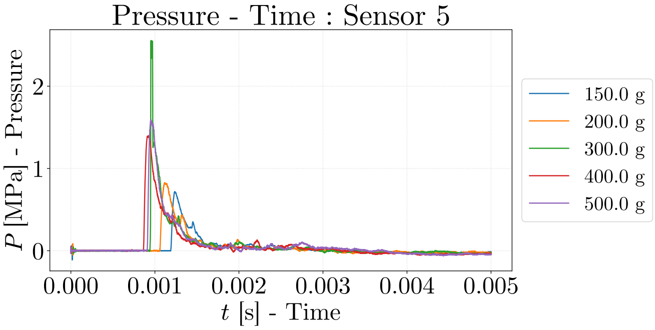

(e) *Sensor 5.*

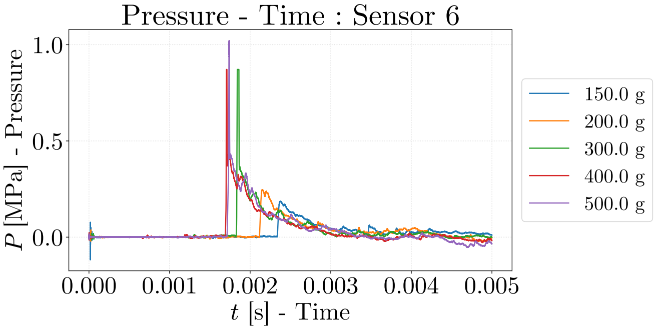

(f) *Sensor 6.*

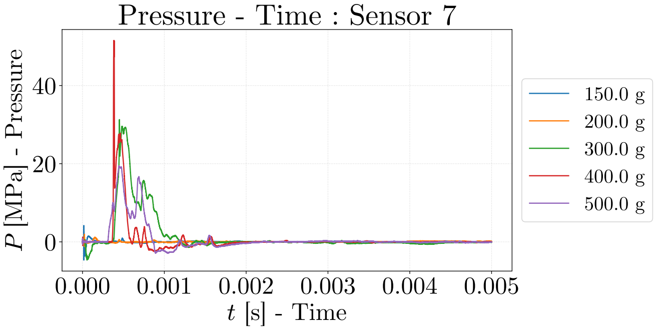

(g) *Sensor 7.*

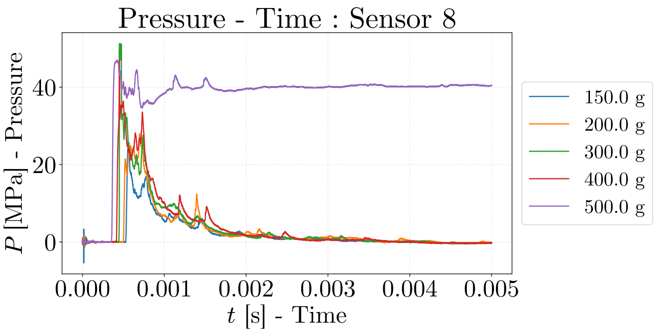

(h) *Sensor 8.*

Figure D.3 – *Pressure measurements from tests on reinforced BASAL Falsrør ig.*

Appendix E

Subroutine

```
      subroutine vusdfld(
! Read only variables
     . nblock, nstatev, nfieldv, nprops, ndir, nshr,
     . jElem, kIntPt, kLayer, kSecPt,
     . stepTime, totalTime, dt, cmname,
     . coordMp, direct, T, charLength, props,
     . stateOld,
! Write only variables
     . stateNew,field)
      include 'vaba_param.inc'
!      implicit double precision (a-h,o-z)
!      parameter (j_sys_Dimension = 2)
!      parameter( n_vec_Length = 544  )
!      parameter( maxblk = n_vec_Length  )
      dimension jElem(nblock),coordMp(nblock,*),direct(nblock,3,3),
     .          T(nblock,3,3),charLength(nblock),props(nprops),
     .          stateOld(nblock,nstatev),stateNew(nblock,nstatev),
     .          field(nblock,nfieldv)
      character*80 cmname
c
      real*8 straindata(maxblk*(ndir+nshr))
      integer jSData(maxblk*(ndir+nshr))
      character*3 cPData(maxblk),cSData(maxblk*(ndir+nshr))
      integer jStatus
      real*8 PE(nblock,6)
      real*8 tr,e1,e2,e3,e4,e5,e6,f1,f2,f3,f4
      real*8 epsp1(nblock),epsp1crit
      integer failactive
!-----------------------------------------------------------------------
!     Read material properties
!
```

```
------------------------------------------------------------------------
      epsp1crit  = props(1)
      failactive = props(2)
!
------------------------------------------------------------------------
!     Call history variables
!
------------------------------------------------------------------------
      call vgetvrm(  'PE', straindata,jSData,cSData,jStatus)
!
------------------------------------------------------------------------
!     Extract data
!
------------------------------------------------------------------------
      do k=1,nblock
         PE(k,1) = straindata(k)
         PE(k,2) = straindata(k+nblock)
         PE(k,3) = straindata(k+nblock*2)
         PE(k,4) = straindata(k+nblock*3)
         PE(k,5) = straindata(k+nblock*4)
         PE(k,6) = straindata(k+nblock*5)
      enddo
!
------------------------------------------------------------------------
!     Compute principal stresses and strains
!
------------------------------------------------------------------------
      do k=1,nblock
         tr = (PE(k,1)+PE(k,2)+PE(k,3))*one3
         e1 = PE(k,1)-tr
         e2 = PE(k,2)-tr
         e3 = PE(k,3)-tr
         e4 = PE(k,4)
         e5 = PE(k,5)
         e6 = PE(k,6)
         f1 = 0.5d0*(e1*e1+e2*e2+e3*e3)+e4*e4+e5*e5+e6*e6
         f2 = e1*e5*e5+e2*e6*e6+e3*e4*e4-e1*e2*e3-2.0d0*e4*e5*e6
         f3 =-sqrt(27.d0/f1)*f2*0.5/f1
         f3 = sign(min(abs(f3),1.0d0),f3)
         f4 = acos(f3)/3.0
         epsp1(k) = tr+2.0*sqrt(f1/3.0)*cos(f4)
      enddo
!
------------------------------------------------------------------------
!     Compute Damage according to CL
!
------------------------------------------------------------------------
```

```
      do k=1,nblock
         if((epsp1(k).gt.epsp1crit).and.(failactive.eq.1))then
            stateNew(k,nstatev) = 0
         else
            stateNew(k,nstatev) = 1
         endif
      enddo
!  ------------------------------------------------------------------------
!     End of subroutine
!  ------------------------------------------------------------------------
      return
      end
```